Title
A High-Density Carbon Fiber Neural Recording Array Technology: Design, Fabrication, Assembly, and Validation

Author
Massey, Travis Lee

Publication Date
2018

Peer reviewed|Thesis/dissertation

A High-Density Carbon Fiber Neural Recording Array Technology: Design, Fabrication, Assembly, and Validation

by

Travis Lee Massey

A dissertation submitted in partial satisfaction of the

requirements for the degree of

Doctor of Philosophy

in

Engineering — Electrical Engineering and Computer Sciences

in the

Graduate Division

of the

University of California, Berkeley

Committee in charge:

Professor Michel M. Maharbiz, Chair
Professor Kristofer S.J. Pister
Professor Michael R. DeWeese

Spring 2018

A High-Density Carbon Fiber Neural Recording Array Technology: Design, Fabrication, Assembly, and Validation

Abstract

A High-Density Carbon Fiber Neural Recording Array Technology: Design, Fabrication, Assembly, and Validation

by

Travis Lee Massey

Doctor of Philosophy in Engineering — Electrical Engineering and Computer Sciences

University of California, Berkeley

Professor Michel M. Maharbiz, Chair

Increasingly advanced tools are desired for understanding electrical activity in the brain, whether for basic neuroscience or clinically relevant brain-machine interfaces. Among the many classes of tools available, intracortical neural recording electrodes have the potential advantage of both high spatial and temporal resolution, and depending on the device can be suitable for either acute or chronic applications. To achieve the breadth of desirable characteristics for an acute neural recording array, including minimal adverse biological response, full-volume sampling, and scalability to a large number of recording electrodes, a new type of device must be developed. This dissertation presents significant steps toward such a device, demonstrating a high-density 32-channel carbon fiber microwire neural recording array capable of acute *in vivo* recording. Departing from the in-plane architectural paradigm of conventional microwire-style neural recording arrays, an array substrate is microfabricated in silicon and 5 µm diameter carbon fiber monofilaments are threaded through holes in that silicon substrate to create a two-dimensional array of carbon fiber recording electrodes that can, in principle, be scaled to an arbitrary number of recording electrodes. In addition to scalability, this device architecture affords electrode pitch four times finer than the state of the art among microwire recording arrays. The fine diameter of the carbon fibers affords both minimal cross-section and nearly three orders of magnitude greater lateral compliance compared to traditional tungsten microwires, with these features serving to minimize the adverse biological response of the implanted electrodes.

The substrate microfabrication and array assembly processes are robust and repeatable, and with the introduction of a robotic system to automate the insertion of carbon fibers into the through-silicon vias with submicron precision, the processes are fundamentally scalable to an array with a large number of electrodes. A specially formulated isotropically conductive adhesive mechanically and electrically bonds the carbon fiber recording electrodes to the silicon substrate, and post-processing of both the adhesive and the recording sites serves to further lower the impedance for superior electrophysiological characteristics. Recording is demonstrated in the primary motor cortex of a rat, with single-unit action potentials being recorded on many channels. This carbon fiber microwire neural recording array is a promising technology for increasing information density

while minimizing the adverse biological response in acute preparations, particularly in applications where microwire arrays are already commonplace.

To my parents, Warren and Anita, without whom I wouldn't have begun this journey,
and to my wife, Siao Charn, without whom I wouldn't have finished.

Contents

List of Figures

List of Tables

Acknowledgments

A PhD is never undertaken alone, and I have been fortunate to have a wonderful group of colleagues, mentors, friends, and family surrounding me and supporting me throughout the entire journey.

Michel Maharbiz and Kris Pister — Thank you for mentoring me not only on the technical details, but in how to be a better researcher; how to conceptualize, evaluate, and develop ideas; how to sell the story; and how to take a step back when I'm lost in the weeds. You struck the perfect balance, giving me plenty of room to experiment and explore on my own, even when that meant venturing into new and unrelated fields, but you were always there when I needed to come back for advice. I'm deeply grateful for all of your patience and persistence with me over the years. I have deeply enjoyed working with and learning from each of you.

Steven Lanzisera — Your guidance as my first research mentor during my undergrad years played a major role in my decision to continue research as a PhD student. Your words of wisdom/warning regarding the mid-PhD crisis have been comforting not only to me, but to many other grad students in turn. Thank you for taking the time to care.

Anita Flynn — For your mentorship and words of wisdom during my transition from undergrad to PhD, and for teaching me that "everything is a connector problem." Those words have been consistently true and have shaped the way I view nearly every problem.

Colleagues in the Maharbiz and Pister groups — I can't possibly list you all, but thank you for the countless conversations that helped to shape both my research direction and my outlook on the world. Thank you for being a sounding board for each crazy idea of the week, entertaining all of my esoteric questions, and bringing laughter and camaraderie to what might otherwise have been lonely years in the lab. Special thanks to those of you with whom I got to spend days, nights, and weekends the Nanolab, and particularly those who preceded me and taught me everything I know.

Samantha Santacruz — Thank you for helping out with the *in-vivo* testing, as well as for putting up with my ever-shifting timeline.

My "undergrad army" — To all those I mentored, thank you for your hard work and dedication. I learned something from each and every one of you and came to enjoy my time with most of you. Sorry for using you as guinea pigs as I experimented with different management strategies. It speaks to your resilience that you survived my inexperience.

The Marvell Nanolab Staff — Thank you especially to Bill Flounders, Ryan Rivers, Allison Dove, Jeff Clarkson, and Richelieu Hemphill for the many process discussions and for entrusting me with the latitude to run so many oddball processes.

Friends and former brothers of the many iterations of Grad Haven — Your encouragement, prayers, and hilarious antics kept me sane and grounded throughout the years. I can't imagine having gone through this without you guys alongside. I'll always have a special place in my heart for nerding out on the most inane topics. *tl;dr: You shouldn't put the knife in the microwave*.

Mom and Dad — Thank you for raising me to be inquisitive and to persevere, and for providing a home where I felt safe to learn, grow, and explore. You made sure to support me in everything, especially when I failed so I could learn to get back up again. Thank you for all of your love and care.

Siao Charn — Words don't exist to thank you enough for your infinite patience, love, and support over the past six years, and for nourishing me with your words of encouragement, food, and hugs. You put up with so many late nights without complaint, but were always there to help me decompress when I got home and midnight and remind me that there *is* life outside of the lab. Coming home to you is the highlight of my every day; you truly are the perfect wife for me, and I can't possibly imagine going through life without you.

Chapter 1

Introduction to neural recording devices and needs in the field

Neural signals and the interconnections among neurons encode all of the information in our brains, and yet our understanding of how these signals and interconnections translate to thoughts, actions, or our practical experience of daily life are still largely unknown. Despite the extraordinary research and clinical progress in the 130 years since Ramón y Cajal's initial staining that yielded the first insight to the structure of the brain [1], we are still far from a comprehensive knowledge of the nervous system and how to treat most neurological disorders and damage. The complexity of the brain and scope of these afflictions are far too broad to be understood and addressed by any one method, but as with any complex research or clinical problem, appropriate tools are necessary for proper investigation and intervention.

The set of tools available for probing neural activity is broad, ranging from from dyes sensitive to electrical or chemical changes to room-sized scanners providing high-level structural and functional insights [2–5]. Each has its distinct advantages and applications, with key metrics including spatial resolution, temporal resolution, sampling volume, degree of invasiveness or adverse biological response, and type of signal measured (electrical, chemical, optical, thermal, etc.). The dominant and arguably most clinically-relevant method of investigating activity at the level of individual neurons involves directly measuring the extracellular voltage correlated with a neuronal action potential (AP) [6, 7]. By associating these low-level neural signals with particular input or output information, one can begin to tease apart accessible neural circuits. Those inputs and outputs may be external, such as sensory inputs and behavioral outputs, or they may be local inputs and outputs within a neural circuit. The rapidly growing field of brain-machine interfaces (BMI) externalizes either the input or the output to a computer for specific signal processing and feedback to aid in relating neural signals to inputs or outputs [8].

BMI and neuroprosthetics provide a compelling bridge from research to clinical applications of neural recording and stimulation potentially applicable to a broad range of sensory and motor prosthetics [9–11]; however, new tools are needed. Of particular note is the neural interface itself, the electrical device that directly interfaces with the brain to record from or stimulate neurons. Broadly, the ideal neural interface for BMI and most neuroprosthetic applications is able to record

from or stimulate every neuron in a large volume of tissue with high spatiotemporal resolution for the lifetime of the patient of time without adversely affecting the nervous system. This is a lofty goal, but these design ideals justify current practices and will guide the following discussion toward the development of a better neural recording array.

1.1 Basics of neural recording

It is necessary to first consider the characteristics of neural signals in the time and frequency domain, and how they are recorded, as this will in turn inform the design of the recording array. Neural signals are typically classified by frequency into either local field potentials ($<$ 300 Hz) or single/multi-units ($>$ 300 Hz) [7]. Local field potentials represent an average of neural activity over some volume, and include the well-known neural oscillations ($<$ 80 Hz), but often the term is also used to refer to the aggregate trends of many neurons firing within the local volume around the recording site [12, 13]. Single/multi-unit activity refers to activity from one or a few neurons, i.e. not a low-frequency spatial average. Single-unit activity is a signal from a single neuron, likely but not necessarily an AP, and multi-unit activity refers to the simultaneous activity of several neurons in a local volume, such that their independent activity can not be distinguished. Beyond APs, single- or multi-unit activity might include hyperpolarization of neurons or a subthreshold excitatory/inhibitory postsynaptic potential (E/IPSP) [7].

To better understand each of these terms, consider the five phases of an typical action potential (Figure 1.1). Initially, the interior of the neuron is at its *resting* potential of approximately -70 mV

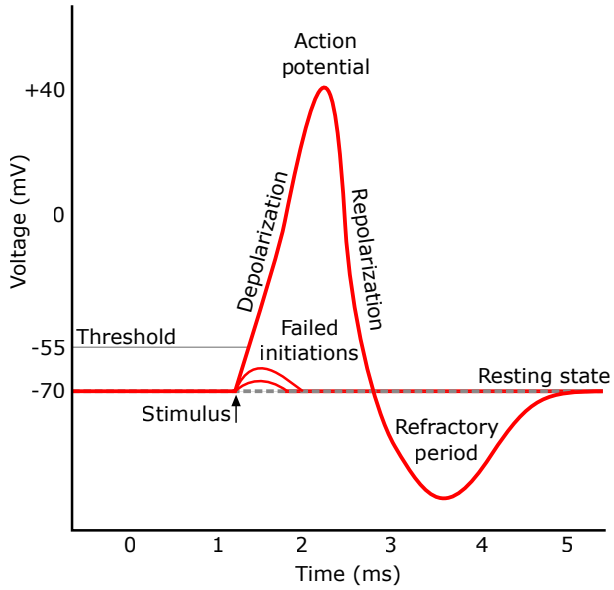

Figure 1.1: A schematic of a typical action potential. *Figure credit: Wikimedia Commons*

relative to the surrounding media. Next, the neuron receives a *stimulus* in the form of coincident EPSPs. Each EPSP raises the potential across the cell membrane by a few millivolts. If the EPSPs arrive infrequently, the potential decays back to -70 mV, but several simultaneous EPSPs will sum to raise the potential above the threshold value of -55 mV. Once this threshold is reached, ion channels in the cell membrane open and the potential rapidly increases. Because the potential is becoming less negative, this is called *depolarization*. This increase in potential proceeds up to +40 mV before just as rapidly *repolarizing*, overshooting the -70 mV resting potential. This overshoot below -70 mV and the subsequent recovery period back to the resting potential is known as the *refractory period*. This entire process from the stimulus to the refractory period takes place over a few milliseconds. While each of these phases is of interest in many situations, some applications including BMI are primarily interested in the rapid depolarization and repolarization, which is colloquially referred to as the "spike." This takes place over approximately one millisecond and sets a lower bound on the frequency band of interest for single-unit neural recording.

A neural recording electrode is used to sense this change in potential. Ideally one would record the potential difference across the membrane (intracellular recording), but this is often difficult to do without puncturing and destroying the cell. The dominant intracellular recording method, patch clamping, is time consuming and not easily scalable to more than a few electrodes, as each electrode must be manually placed under a microscope [14, 15]. In contrast extracellular potentials are much easier to record. Rather than measuring a neuron's membrane potential directly, extracelluar recording instead measures the voltage immediately outside of a neuron or group of neurons relative to some reference potential, usually a large spatial average or a region presumed to be largely inactive, potentially elsewhere in the body [16]. Because the voltage change during an action potential is a result of ion flow into or out of a neuron, there is a relative change in ion concentration immediately outside of a neuron as ions are taken up or expelled. This ion concentration, which is roughly the inverse of an action potential, is measured [7]. Because the change in concentration in the electrolyte outside the neuron is significantly less pronounced than the change inside, the observed change in voltage is typically 2-3 orders of magnitude smaller, on the order of tens or hundreds of microvolts.

Because this signal is so small, the voltage must be amplified before recording. While this may initially seem trivial, improper understanding of this effective circuit have led to incorrect conclusions within the electrophysiology community regarding ideal electrode design (personal conversations). The electrode, in its simplest conceptual form, is just a wire to "short" the extracelluar potential to the input of the voltage amplifier. Considering the circuit primarily in terms of voltages can be misleading, however; rather, it is helpful to consider the circuit in terms of currents, resistances, and capacitances, such that the goal of neural recording is to charge the capacitance at the input of the amplifier on a time scale similar to that of the action potential by flowing a current through the recording electrode. Unfortunately this model is also incomplete, in that the interface between the electrode and the electrolyte is not simply resistive [17]. An electric double layer (EDL) forms at the interface, resulting in an aggregation of ions at the interface behaving as a large capacitor [18]. Considering this capacitive interface independently of the aforemetioned resistive compontent, the capacitor would be floating. Moving charge on the electrolyte side of the capacitor will cause the electrode side to float correspondingly up or down, changing the voltage

presented at the input capacitance of the amplifier. Taking these resistive and capacitive components of the interface in conjunction would suggest that the ideal recording electrode would have low resistance and high capacitance at this interface, or simply low impedance (Equation 1.1). Increasing the area of the electrode will accomplish both, but will also reduce the spatial resolution of the recording electrode, meaning that there is an inherent trade-off between impedance and spatial resolution in neural recording. Electroplating is a commonly employed technique to overcome this trade-off, effectively increasing the area of the recording site by increasing surface roughness without increasing the area over which the electrode is averaging [19].

From the electrode model given in Figure 1.2, the impedance of the electric double layer is:

$$Z_{EDL} = \frac{(R_{sm} + \frac{1}{j\omega C_{lg}})R_{lg}}{R_{lg} + R_{sm} + \frac{1}{j\omega C_{lg}}} \tag{1.1}$$

It is worth brief discussion of the predominant misunderstanding regarding the ideal neural recording electrode, that the electrode impedance should be as high as possible. The first reason that this is improperly claimed relates to the aforementioned impedance-area trade-off. Because it is important to have a small recording area to avoid spatial averaging, electrophysiologists traditionally use fine wire, which has a higher impedance than coarse wire. This choice of fine wire has inadvertently been interpreted to support the notion that high impedance electrodes are superior. Second, patch clamp electrodes for intracellular recording typically have gigaohm impedances yet record high quality signals due to the large signal present, leading to the misplaced generalization that very high impedances must be ideal. Finally, a naive understanding of the equivalent circuit model has led some to reason that a large electrode impedance is desirable such that a large voltage drop occurs across the electrode and is present at the input to the amplifier. This follows the same reasoning that voltage amplifiers ideally have an infinite input impedance, incorrectly conflating the electrode and the amplifier.

A full equivalent circuit diagram of the recording environment is given in Figure 1.2. The action potential is represented by a current source in the presence of an electrolyte, a shunt and series resistance. The division between the shunt resistance of the electrolyte and the resistance looking into the electrode, electrolyte series resistance included, presents a smaller resistance at the electrode-electrolyte interface. The EDL can be represented at low voltages as a resistance in parallel with a series resistor and capacitor. This EDL typically dominates the electrode impedance, and is traditionally lumped into one complex impedance value. Following the electrode-electrolyte interface is the distributed resistance and capacitance of the electrode itself and the subsequent interconnect, and finally the input capacitance of the amplifier. The input capacitance of the amplifier is typically 2-3 orders of magnitude smaller than the EDL capacitance.

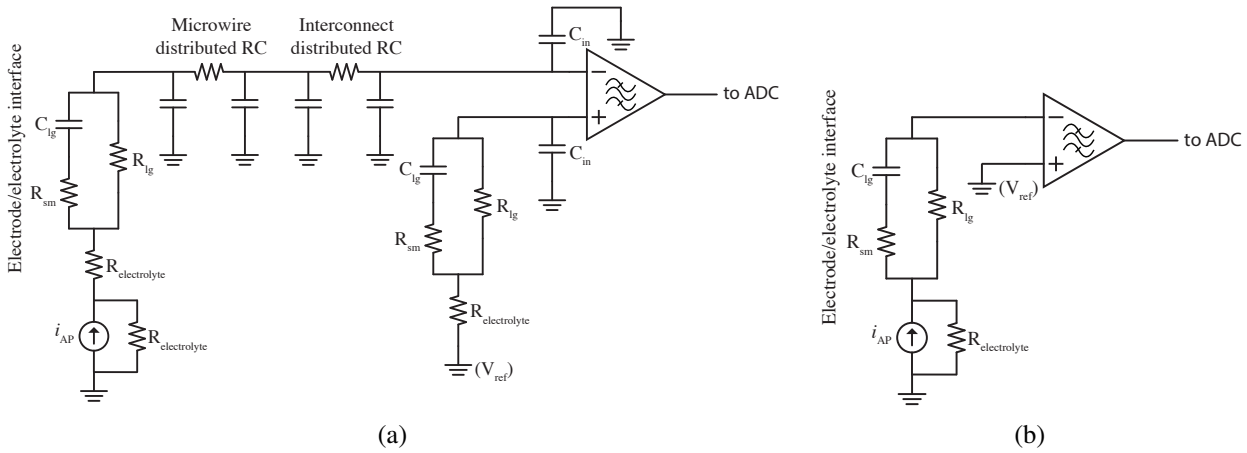

Figure 1.2: (a) Complete and (b) simplified equivalent circuit models of the recording environment. The action potential is represented as a current source, i_{AP}, and the electrolyte, interface, electrode, and interconnect are represented by resistors and capacitors. Distributed resistances and capacitances are represented by lumped models for simplicity. The amplifier has a preset application-specific closed-loop gain and bandpass corner frequencies.

1.2 Families of neural recording arrays

A neural recording array is a device comprised of multiple neural recording electrodes positioned to record simultaneously from multiple independent units. Each recording electrode is routed to an amplifier channel or multiplexer for processing and digitization. Several families of neural recording arrays exist, differing in their spatial resolution, level of invasiveness, and target application. This notion of invasiveness, discussed here only qualitatively, is treated in depth in Section 1.3. At the highest level, there is a tradeoff between spatial resolution and degree of invasiveness. Technologies may also differ by the volume sampled, though typically the volume sampled is inversely related with the spatial resolution and proportional to the electrode count. While not exhaustive, the predominant families of neural recording arrays include electroencephalograms (EEGs) and magnetoencephalograms (MEGs), electrocorticograms (ECoGs) and micro-ECoGs (μECoGs), and intracortical arrays [20–23]. The intracortical arrays may be further subdivided into shank-style probes (i.e. Michigan arrays), microwire arrays, Utah arrays, and polytrodes [24–27].

Extracortical recording arrays

EEGs are the dominant style of extracortical neural recording array, recording subtle changes in electric field. Affixed to the scalp, centimeter-scale EEG electrodes record a local average of neural activity. With appropriate signal processing and interpretation, EEG can provide insight into rhythms and transient activity within the local area surrounding each electrode. MEG is the dual of EEG, recording magnetic field changes due to ionic currents in the neurons rather than the electric field. The magnetic fields are much more difficult to detect than the electric fields,

typically requiring superconducting detector arrays in magnetically shielded rooms. While the depth of recording is shallower than EEG, MEG can provide greater lateral resolution because the magnetic fields are relatively unperturbed by the skull and tissue compared with the heavily distorted electric fields.

Similar in principal to EEG is ECoG, in which sheet of arrayed electrodes rests directly on the surface of the cortex rather than extracranially [22]; capacitive sensing electrodes detect the local electric fields generated by groups of neurons. In contrast to EEG, however, ECoG sits beneath the skull on the surface of the brain. Rather than independent electrodes, ECoG arrays have electrodes patterned into a flexible sheet that can conform to the surface of the brain. Because these electrodes are closer to the surface of the brain, their temporal and spatial resolution can be greater than EEG. μECoGs are, as their name implies, smaller scale microfabricated ECoGs. Whereas a typical ECoG electrode site might be several millimeters in diameter, each μECoG electrode site is typically tens to hundreds of microns [23, 28–37]. Typical ECoGs and μECoGs may contain 16-128 recording sites arranged in a two dimensional array. Because ECoGs and μECoGs record extracortically, leading to smaller detected signals compared with intracortical electrodes, the recording site can not be miniaturized sufficiently to detect single units without thermal and background noise exceeding the signal level; rather, they are best suited for detecting population activity with electrodes at least 40 μm in diameter [23].

Intracortical recording arrays

To record single-unit activity, an electrode must be placed relatively close to the neurons [38, 39]. Extracelluar intracortical recording electrodes place a recording site, typically well below 100 µm in diameter, some depth below the surface of the brain, with an insulated conductor routing the signal to the surface of the brain and out to an amplifier. The simplest intracortical recording electrode, as previously mentioned, is an insulated microwire with a cut tip forming the recording site. The simplest form of intracortical recording array, then, is multiple such wires inserted into the brain in parallel. Here it is worth making a distinction between multiple individual recording electrodes and a true array. Going forward, I will use “array” to refer to a collection of recording electrodes that are physically bound in some way and can be manipulated as one unit.

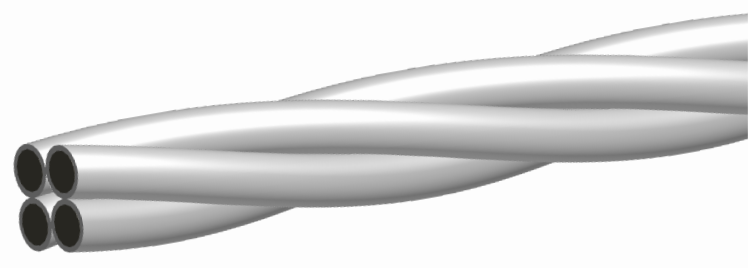

Figure 1.3: A tetrode recording array comprised of four insulated microwires twisted into a bundle.

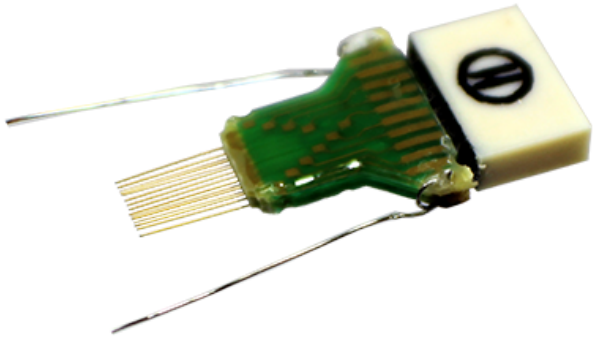

Figure 1.4: A microwire neural recording array comprised of sixteen tungsten microwire electrodes and two ground electrodes on a PCB. *Figure reproduced with permission from Tucker-Davis Technologies (TDT).*

The oldest form of intracortical recording device with multiple electrodes is the polytrode, a bundle of two or more microwire recording electrodes twisted or otherwise bound together and inserted together [27, 40]. Polytrodes are often described by the number of recording electrodes in the bundle, with the most common being stereotrodes (two wires) and tetrodes (four wires, Figure 1.3). These microwires may be cut at the same or different lengths and at varying angles in order to define the volume sampled by the polytrode. Commonly the recording sites are defined such that they spatially oversample a given volume, and the subtle differences in the signals received at each electrode are used to localize each unit [40, 41]. The costs of this arrangement, however, are that polytrodes typically only sample a small volume and provide little more unique information of unit activity than a single recording electrode. Furthermore, the large cross-section of polytrodes exacerbates the tissue's adverse response to the implanted device.

Microwire arrays are similarly comprised of multiple 25-50 μm tungsten microwire recording electrodes, but are distinct in that the microwires are spaced apart some distance (figure 1.4) [25, 42]. This spacing means that histologically, microwire arrays interact with tissues much like a series of individual recording electrodes would [43]; there is typically little interaction between the adverse biological responses of adjacent recording electrodes. The construction of microwire arrays is somewhat more complex, in that the individual microwires are laid out along and electrically connected to a common backplane as a linear array, most often a printed circuit board (PCB) [44, 45]. As multiple layers of PCBs are stacked, several linear arrays form a two-dimensional microwire array. The PCB trace pitch and board thickness set the pitch of the array, which is typically in the range of 150-400 microns in each axis [25]. The microwire arrays developed and used in the Nicolelis group at Duke have set the standard for microwire neural recording arrays. Microwire arrays have the advantages that they can record from a large volume and can be assembled without advanced microfabrication processes, but are labor-intensive to assemble.

The Utah array is a significant evolution of the initial concept of a microwire recording ar-

ray. Taking advantage of monolithic fabrication techniques and addressing the challenges of hand assembling many-electrode microwire arrays, the Utah array is a ten by ten array of 1.5 mm long sharp silicon recording electrodes that are 90 µm in diameter at a 400 µm micron pitch (figure 1.5) [26, 46]. The conductive p+ silicon electrodes are metallized and insulated with standard silicon microfabrication processes, and traces route the signal out to an array of pads on the back side of the device for easy integration with a standard connector. This monolithic approach to fabrication has been a strength of the Utah array and has contributed to its commercial viability and widespread use. The key limitations of the Utah array are its large electrode diameter and pitch, which lead to more a severe adverse biological response and lower sampling density, respectively [47].

The last major class of intracortical neural recording arrays is the shank-style probe. Originally developed by Ken Wise as a student at Stanford, subsequently by his research group at the University of Michigan [24], these shank-style probes are commonly referred to as "Michigan-style probes," though versions have been developed at nearly as many institutions as are developing other recording devices [49–52]. Shank-style probes are microfabricated devices with recording sites in the plane of the wafer exposed along a common backbone (figure 1.6. When implanted, these probes were traditionally microfabricated in silicon and have been called "silicon probes," but are increasingly being fabricated out of polyimide and other flexible materials [6, 53]. A deposited metal film defines the traces and recording sites, with all but the recording sites electrically insulated. Recording sites are typically a few microns or tens of microns across, and traces can be as small as lithographically viable provided the series resistance of the traces doesn't significant affect the impedance of the recording electrodes. The backbone of the probe, the shank, is commonly in the range of ten to fifty microns thick and tens to hundreds of microns wide [54]. While relatively easy to fabricate and amenable to a variety of designs, this large backbone cross-section

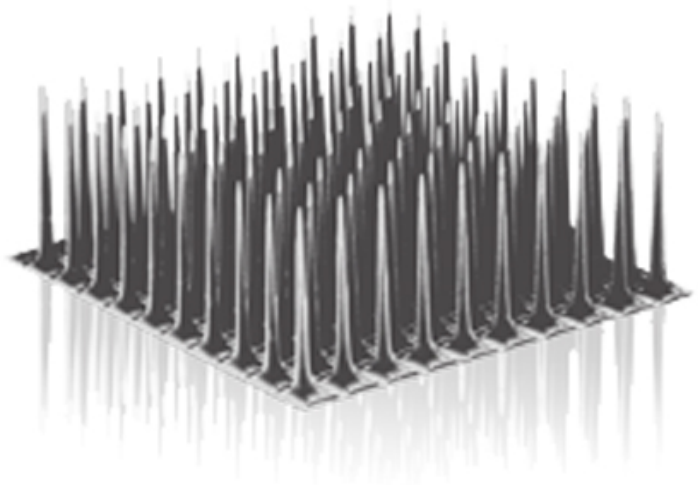

Figure 1.5: A Utah array monolithically fabricated in silicon with 100 electrodes. *Figure reproduced with permission from Blackrock Microsystems.*

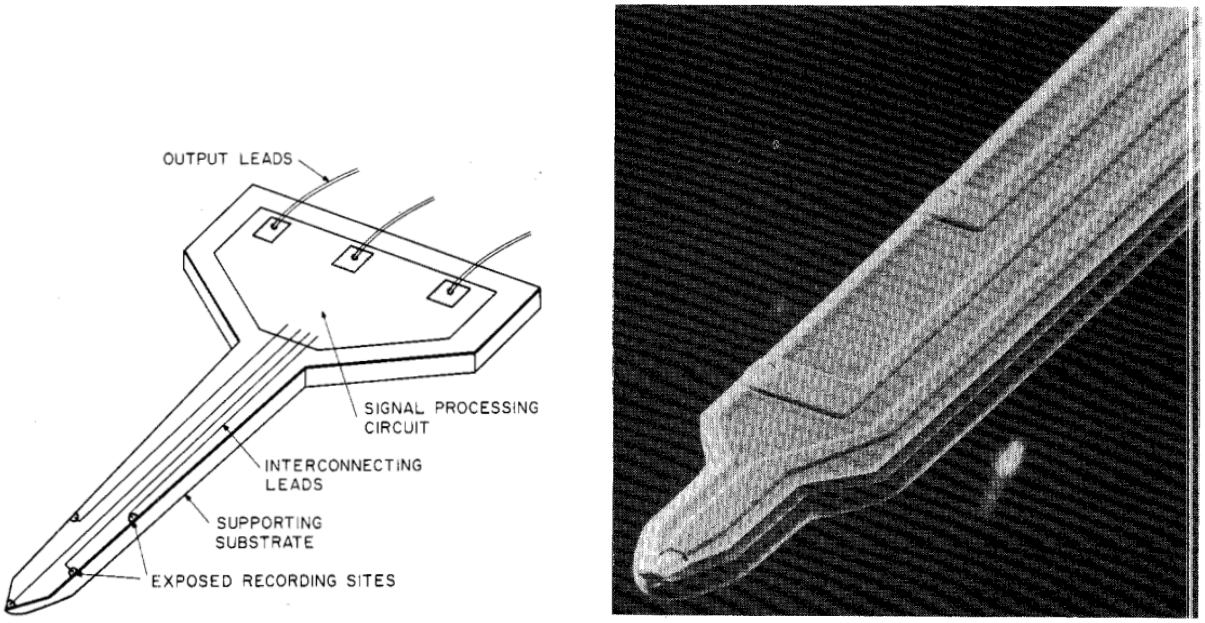

(a) (b)

Figure 1.6: (a) Diagram of a multichannel silicon neural recording probe comprised of a silicon shank with pattered metal electrodes. (b) SEM view of the tip of a recording array. Metal traces are 8 µm wide. *Both (a,b) reproduced from [48] with permission of lead author Khalil Najafi.*

causes a substantial adverse biological response and is one of the major limitations of such a device [55]. Compared to microwire and Utah arrays, shank-style probes are less commonly used in neuroscience and BMI because, anecdotally, the recordings at the lateral sites tend to degrade faster than those at the leading tip of a wire.

1.3 Biological response to implanted neural recording arrays

The biological response to an implanted device is one of the key drivers of continued innovation in the design of intracortical neural recording arrays. Just as the penetration or introduction of any foreign body into healthy tissue initiates a wound healing response, inserting an intracortical array into the brain initiates a specific sequence of adverse biological responses meant to isolate the device, protect the brain from further damage, and inhibit the formation of unsuitable neuronal interconnections [56–59]. Beyond the direct damage of implantation itself, over the course of weeks this response alters the organization of the neurons and causes degradation of the recorded signals from nearby units [60–64]. Thus, understanding and mitigating the adverse biological response to an intracortical neural recording array is central to the design of these devices, particularly if the recording sites are meant to remain viable beyond a single recording session. While neural recording electrodes are commonly used in the peripheral nervous system (PNS) as well, most studies on

the matter and the focus herein are on the CNS in vertebrates. The biological response is somewhat different, but the resulting concerns are similar.

When a device is first inserted, any tissue in the path of the neural recording array is destroyed, including neurons, vasculature, and glial cells. Damage to the vasculature results in a breach of the blood-brain barrier, and blood-borne cells and proteins flow to the site [65]. A clot is formed to prevent bleeding and exclude pathogens, subsequently signaling the initiation of the inflammatory response, the next stage of healing [56, 66, 67].

Microglia, phagocytotic cells native to the CNS, are activated during the inflammation stage to clear degenerating tissue at the wound site in conjunction with any macrophages that crossed the blood-brain barrier [60, 68]. Microglia are typically activated within hours and may remain active for up to two weeks, with a peak in activity three days after initial injury [69, 70]. Astrocytes, activated on a similar time course, help to mitigate neurodegeneration; however, nitric oxide released in this process also contributes to neurodegeneration [57]. Microglia cluster toward the center of the wound site, while astrocytes arrange around the periphery of the wound site in preparation for glial scar formation [70].

This glial scar formation characterizes the repair phase of wound healing. The astrocytes surrounding the wound site extend and intertwine processes to form a robust sheath, the glial scar, over [71]. The tight sheath and active immune response at the wound site both contribute to impeding survival or regeneration of axonal projections and dendritic processes [72]. This is in sharp contrast to healing in the PNS, in which Schwann cells support axonal regeneration [68, 73]. Over the next several weeks, the glial scar continues to densify until after 6-8 weeks the process is complete [60].

Not only does the glial scar physically protect the integrity of the healing blood-brain barrier, it chemically isolates healthy CNS tissue from the toxic inflammatory response [57, 71]. Unfortunately, this robust chemical and physical barrier also electrically insulates the now-sheathed neural recording array, attenuating signal reduction [64, 74, 75]. A likely even greater contribution to signal degradation is that the glial sheath displaces healthy neurons beyond the sampling volume of the electrodes [76].

Mitigating the adverse biological response

Mitigating this adverse biological response has become a central topic in the design of intracortical neural devices, with strategies focused on minimizing electrode size [77–80], matching the stiffness of the intracortical array and neural tissue [81–83], and modifying the surface chemistry to reduce inflammation and gliosis and even promote axonal regrowth [55, 84, 85]. While the relative significance of these three strategies is still subject to active debate, it is clear that all three play a significant role [86]. Further, there is evidence suggesting that if the blood-brain barrier is not penetrated, that is, if vasculature is not ruptured, that no adverse biological response would occur [56].

The size of the implant is significant not only because smaller devices will damage proportionally less tissue, but below a certain threshold certain aspects of the biological response cease. For example, Bernatchez *et al.* showed that macrophages do not adhere to and attempt to phagocytose

10-12 µm fibers, but will adhere to and react normally with larger fibers [77]. This is in agreement with prior work, which had showed that the critical threshold for macrophage adhesion in bone healing was 10-15 µm [87]. Similarly, polypropylene fibers inserted subcutaneously in a rat showed little or no encapsulation below a diameter threshold of 6 µm. These findings have since been corroborated in the CNS; 7 µm carbon fibers show little to no glial encapsulation 10-16 weeks post-implantation [88].

The goal of the recent emphasis on polymer-based neural recording arrays is to approximately match the stiffness of the electrode to the stiffness of the neural tissue, such that when the brain moves and flexes, the implanted device is able to move and flex with it without exerting damaging stress on the tissue [6, 89]. Lateral micromotion in a rat's brain is typically on the order of 2-25 µm due to respiration, and there may up to 80 µm of long-term drift [90]. If the neural implant unable to flex with these micromotions and is rigidly tethered to the skull, a significant force will be exerted on the neural tissue, exacerbating the damage already done during implantation and enlarging the glial scar [81]. Inserting flexible devices can prove challenging, so techniques have been developed to support these devices with polymers soluble in saline [53]. Alternatively, a rigid probe may be connected via a flexible tether to partially mitigate the effects of micromotion [52].

There are two key aspects with regards to the surface chemistry of implantable neural arrays. First, any materials exposed should be chemically inert to the the physiological environment. This traditionally includes the electrode material, any surface coating electroplated onto the electrode, the body of the neural recording device (if applicable), and the insulation used to electrically isolate the body of the device or microwires from the recording electrodes. This point is given little attention, because a relatively large set of accepted materials exist in the field for each of the above. The notable exception is that some common microwire materials, including tungsten, slowly corrode in the physiological environment [84]. The second key aspect discussed regarding the surface chemistry of implantable neural arrays is any additional coating added for the purpose of encouraging healthy tissue growth or healing in the vicinity of the device [91]. This so-called bioactive coating often contains biological signaling molecules or surface proteins meant to trick the neural tissue into treating the device as a native structure [55, 85]. These bioactive coatings are largely independent of the device design and may eventually be applied to all neural devices, but are not further considered in the scope of this dissertation.

1.4 Desirable characteristics of a intracortical neural recording array

Based upon the preceding considerations of the physical basis of neural recording, the biological response to implanted devices, and the historical use cases of neural recording devices, one can begin to develop a broad description of the characteristics of an "ideal" neural recording array. While the priority of each requirement will vary by application, the ideal general-purpose array would have several broad qualities, including a large number of recording sites (scalability), minimal adverse biological impact, high spatial and temporal resolution, low electrode impedance,

and longevity for chronic implantation. While not yet practically feasible to simultaneously meet every criterion, this combination of ideal qualities will lead to a proposed neural recording array that forms the basis for the device described in the following chapter.

Scalability

If the ideal recording array is to have a large number of recording electrodes, it must be scalable. Intracortical on the order of 100 electrodes are used in common practice, and the state of the art is approximately 1000 electrodes [51, 54, 92]. The ideal neural recording array, then, would be able to scale to thousands or tens of thousands of recording sites. Since manual assembly at scales of thousands of electrodes is no longer feasible, this suggests that the device must be either monolithically fabricated, or the assembly must be either automated or parallelized. This is consistent with how Utah arrays and shank-style probes are fabricated, but microwire arrays tend to be hand assembled and are difficult to scale. Nicolelis implanted 704 microwires among several arrays in a rat's brain, but none of the inidividual arrays had more than 128 microwires [25]. Polytrodes are fundamentally not scalable, and benefits beyond 9-16 microwires are minimal.

Beyond the number of electrodes that can be included in a given device, routing of those signals must be considered both within the device and between the device and the recording system. Routing thousands of wires out from the head of an animal is infeasible, both because of the weight and bulk of the wires and because connectors and interfaces tend to be large, dominating the area of any intracortical neural device. Integrated electronics to multiplex, amplify, digitize, and serialize the recorded information can address this issue, and have grown into a large field of their own. To reduce data rates and thus power requirements and heat dissipation, these integrated circuits often also include signal processing to compress the data to be transmitted. While such circuits can be designed independently of a particular neural recording array, the ideal neural recording array will either include on-device, or easily interface with, these headstage electronics. Integrated circuits are traditionally limited to integrating with other devices in one of four key ways: wire bonding, flip-chip bonding, through-silicon vias, and monolithic integration, i.e. fabricating the integrated circuit and the neural recording device in the same piece of silicon, as recently demonstrated in the Neuropixels probe [93]. Again, these constraints suggest either a silicon-based or PCB-based device.

Minimal adverse biological response

Per the preceding section, to minimize the adverse biological response the implanted cross-section should be small, the device flexible, and the surface biocompatible or bioactive. Preliminary evidence also suggests that implanted devices or electrodes with a cylindrical cross-section elicit a less severe response than those with a rectangular cross-section [94]. Patel et al. showed [80] that an array of sixteen 8.4 µm carbon fibers implanted in the cortex elicits a significantly lower response from microglia and astrocyles and does not perceptibly displace healthy neurons (Figure 1.7). This is presented in contrast with an implanted silicon shank-style probe, which elicits a significant adverse biological response.

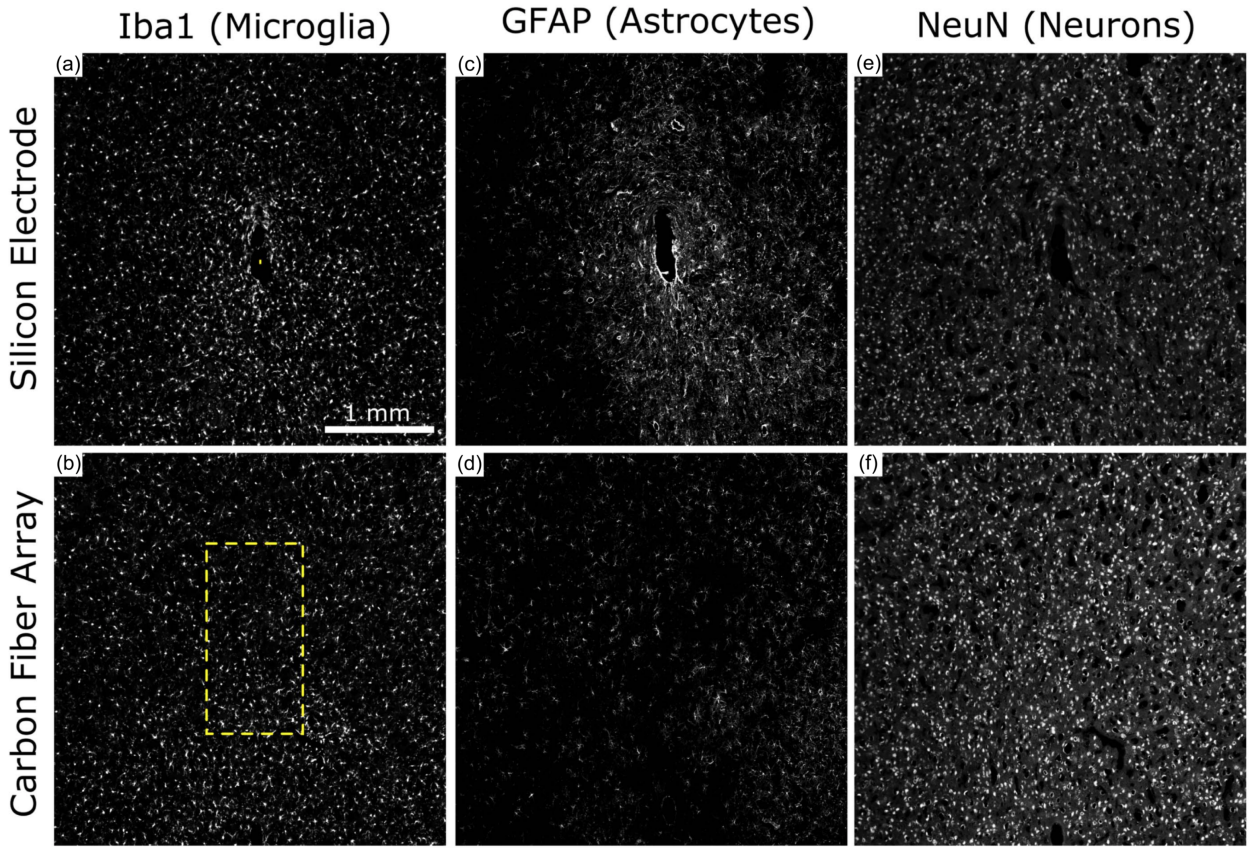

Figure 1.7: Chronic histology images and analysis. (a) and (b) Iba1 (microglia) staining around the implanted carbon fiber array and silicon electrode in ZCR19. Formation of a scar is well defined around the silicon electrode but not so around the carbon fiber array. Yellow rectangles show location and approximate size of implanted electrodes. (c) and (d) GFAP (astrocyte) staining around the implanted carbon fiber array and silicon electrode in ZCR19. Increased glial activity can be observed surrounding the silicon electrode with no obvious uptick in activity around the carbon fiber array. (e) and (f) NeuN (neuron) staining around the implanted carbon fiber array and silicon electrode in ZCR19. Neural density appears much more diminished around the silicon electrode as compared to the carbon fiber array. *Figure and caption from [80] are reproduced with permission of lead author Paras Patel.*

The cross-section of the implanted device may be separated into two components: the cross-sectional area of an individual unit, i.e. a single microwire in a microwire array or a single silicon probe in an array of silicon probes, and the volumetric displacement within the area of implantation. A microwire or Utah array with an electrode pitch equal to twice the diameter of the microwires would displace or destroy approximately 20% of the tissue in the region of implantation, whereas an array with larger pitch or finer electrodes would displace considerably less.

Flexibility, as described previously, may be considered both in the stiffness of the device itself as well as in the tether between the device and the skull. The stiffness is a function of the dimensions and the Young's modulus, and as the dimensions of the electrode are equal to the dimensions of the tissue displaced, the ideal device material would simply match the Young's modulus of the tissue, which was measured to be 8-15 kPa in rabbits, rats, and pigs [95]. The ideal device would also have a flexible tether between the implanted electrodes and a connector anchored to the skull to futher minimize damage due to micromotion. Alternatively, if the electrodes themselves are sufficiently laterally compliant, a tether may not be necessary.

Biocompatibility is achieved through careful selection of materials, such that the materials exposed to the neural environment will not corrode, dissolve, or otherwise react. To this end, noble metals such as platinum can be a good choice for any exposed metal, particularly at electrode sites. Many polymers are also quite inert in the physiological environment. Most will eventually degrade, but generally this degradation is sufficiently slow that no toxicity or adverse reaction with the tissue is visible. Many studies on the biocompatibility of a range of materials are available elsewhere [96–99].

High spatiotemporal resolution and full-volume sampling

Temporal resolution is linked with spatial resolution in that it is primarily a function of the volume sampled by a given electrode. Low spatial and temporal resolution go hand-in-hand. Extracortical electrodes sample a relatively large volume, resulting in spatial averaging that effectively low-pass filters the aggregate signal. Extracranial electrodes in particlar may experience such pronounced averaging that only low-frequency oscillations are discernable. Intracortical neural recording devices typically sample small enough volumes that temporal resolution is sufficient to resolve frequency content well above 5 kHz.

The volume sampled and the spatial resolution of a single electrode are entangled functions of the electrode area and impedance as well as the distance of the electrode from the target population of neurons. For the purposes of intracortical neural recording arrays, we can assume the distance to the target neurons is small, on the order of tens or low hundreds of microns, and can be neglected. The electrode impedance is inversely proportional to the area of the electrode and would seem to present a trade-off between low noise and low sampling volume, but electroplating recording sites with high surface area coatings allows the two to be disentangled. By electroplating the recording sites, their effective surface area is increased without increasing their geometric area. This increases the capacitance and conductance, reducing noise and improving signal fidelity, without increasing the spatial area over which the recording site is sensing and averaging. There is one caveat, however; reduced noise allows the detection of smaller signals from more distant units, thereby increasing the sampling volume. Ultimately these small, distant signals are averaged and contribute to the local field potential. Based on these considerations, the ideal individual recording site would have a small geometric area and thus a high spatial resolution but a large effective area due to electroplating and thus a low impedance.

While each recording site ideally records only from a limited local volume, the amount of information to be gathered increases proportionally with the volume of the brain that can be sampled.

Thus, as per the scalability argument, a large number of small recording sites is desirable. Ideally recording sites are spaced frequently such that all units within the sampling volume of the complete array are detected on one or more electrodes. This is called "full-volume sampling." Though the sampling volume of an individual electrode is a function of the area and impedance as described above as well as the impedance and other characteristics of the local biological environment, estimates of the maximum sampling radius have been experimentally found to be in the range of 50-70 µm [38, 39, 100]. Decreasing the pitch further and oversampling the volume may enable spatial localization of individual units and improve spike sorting, as with tetrode recordings [92, 100]. Common tetrodes have an electrode pitch of 12-25 µm, providing a practical lower bound below which little benefit is seen [27, 40]. Thus, the ideal neural recording array would have an electrode pitch between 12 and 50 µm.

Longevity for chronic implantation

A chronically implanted device must be able to withstand the harsh physiological environment if recordings are to remain viable for the lifetime of the device. Baresse *et. al* found that failure of the insulating material is the dominant factor in the gradual degradation of signal quality in a chronic implant [101]. Insulation failure modes primarily include degradation of insulator materials and the introduction of pinhole defects or cracks, as well as delamination from the electrode [102]. Recording sites on microwires and silicon substrates are also known to degrade in chronic implants, as are patterned traces on silicon [103, 104]. Recently silicon carbide has been proposed as a superior material for use in chronically implanted neural devices given that it is chemically inert and, as a wide-bandgap semiconductor, can be employed as both an electrical insulator and a conductive electrode site material [37]. Key observations with regards to the pursuit of an ideal neural recording array are that the insulating material and recording site should both be extremely chemically inert, and the interfaces among the insulation, electrode body, and metallization should be mechanically robust.

1.5 Carbon fiber microwire recording electrodes can begin to address the requirements of the ideal neural recording array

The preceding considerations for the ideal neural recording array present an ambitious goal, and it would be infeasible to satisfy every criterion. Rather, I have chosen to target a significant subset of the criteria and provide a future path to others.

The requirement of minimizing the biological response stipulates that the implanted elements be small, have low Young's modulus, be laterally compliant, and be comprised of biocompatible materials. Because lateral compliance increases as the dimensions of the device decrease, a sufficiently small implanted device will satisfy two of the above criteria. As mentioned previously, the size threshold below which inflammation and encapsulation are minimized is 6-12 µm, and 7 µm

carbon fibers show little to no encapsulation, so it follows that carbon fibers could be suitable electrodes for a neural recording array meant to minimize the adverse biological response. It remains difficult to fabricate a silicon-based neural probe of similar size that is mechanically robust, and the lithographic resolution to pattern a large number of recording sites and traces on such a device would be prohibitive. For these reasons I determined to pursue development of a carbon fiber microwire array.

Carbon fibers are ideal recording electrodes both because of their size and materials properties. Carbon fibers are commonly 4-7 µm in diameter, smaller than the finest microwire available. The Young's modulus of polyacrylonitrile (PAN)-based fibers is 200-280 GPa, and the modulus of pitch-based fibers may be as high as 455 GPa. For reference, the moduli of (100) silicon and tungsten are 180 and 410 GPa, respectively. This means that carbon fibers are relatively stiff for their size, which is beneficial for implantation. Despite their stiffness, however, the fibers are orders of magnitude more compliant due to their fine diameter than the 25 µm tungsten microwire commonly used in microwire arrays. See Appendix A for mechanical analysis of the lateral compliance of these structures. The carbon fiber used in this work is pitch-based due to ease of availability and *lesssim*5.4 µm in diameter (figure 1.8). Of further benefit compared to tungsten, carbon fiber is elastic until it fractures, alleviating the problem of damage due to bent microwires. Kozai *et. al* demonstrated carbon fiber's high fracture stress by bending a 6.8 µm carbon fiber to a radius of 500 µm [55]. Finally, carbon fiber is conductive, with a measured resistance of approximately 1 $k\Omega\,mm^{-1}$, and is biocompatible due to being largely chemically inert.

Fine carbon fiber microelectrodes also provide the benefits of high spatiotemporal resolution and, with an electroplated recording site, sufficiently low impedance for low-noise recording. Achieving full-volume sampling requires fine pitch, for which carbon fibers are better suited than their tungsten microwire counterparts due to displacing less tissue. For the same volume displacement, the pitch of the fibers can reduce compared to the tungsten microwire arrays as the ratio of their diameters. Thus, compared to 25 µm tungsten microwires at 150 µm pitch, carbon fibers can be spaced approximately four times closer. However, achieving such a pitch is not feasible with conventional microwire array design approaches.

Though the foregoing discussion clearly establishes a need for a high-density array of carbon fibers, a wholly new design approach is necessary to achieve the desired electrode pitch. Further, any new design of such a device should also address, or provide a clear path toward, the scalability criterion.

I present in this dissertation the design, fabrication, assembly, characterization, and testing of a high-density carbon fiber monofilament microwire-style neural recording array for acute recording in the CNS. Chapter 2 details the device concept and design, examines prior work into carbon fiber arrays, and describes the microfabrication process. Chapter 3 discusses a system to automate the rate-limiting assembly step, and chapter 4 the general array assembly procedure, electrical characterization, and *in vivo* testing. Chapter 5 concludes by considering what would be required for this device to be scaled to a large number of recording electrodes, recapitulating in the process many of the key contributions of this work.

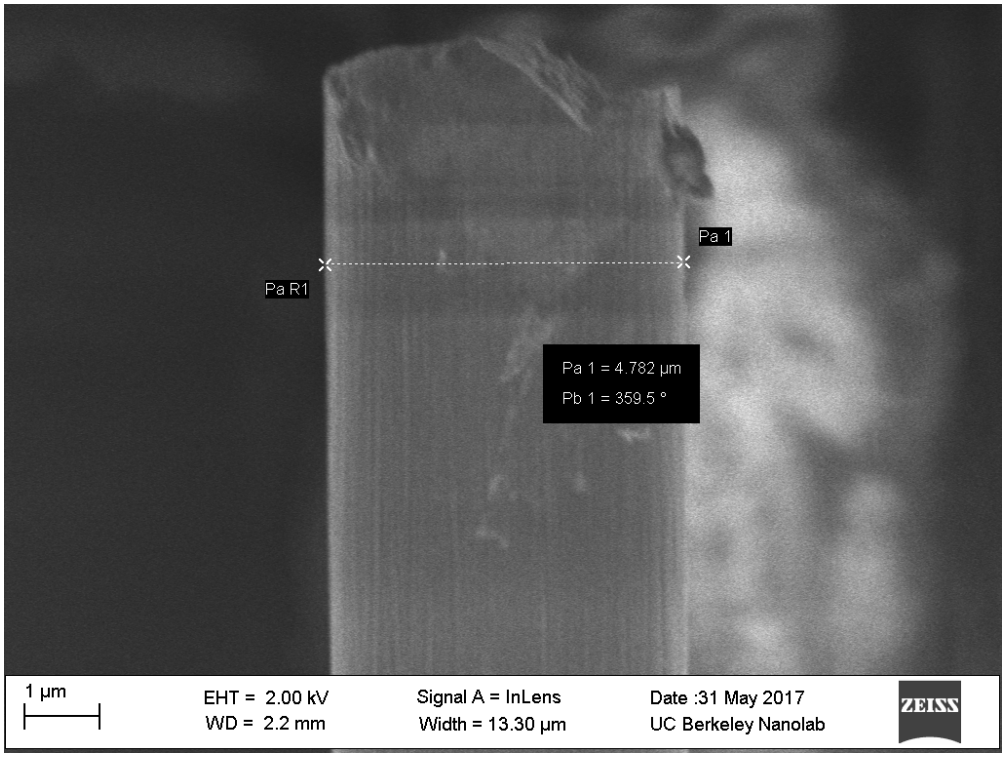

Figure 1.8: SEM of a 4.8 µm carbon fiber.

Chapter 2

Design and microfabrication of a carbon fiber microwire-style neural recording array

2.1 Existing carbon fiber neural recording devices lack density and inherent scalability

Armstrong's pioneering work in 1979 using carbon fibers as neural recording electrodes demonstrated their promise [105], but a high-density, fundamentally scalable carbon fiber neural recording array has yet to be demonstrated. Kozai demonstrated miniaturization of the carbon fiber electrode and a minimal adverse biological response [55], and interest immediately developed in arraying carbon fibers. Initial efforts in producing multi-fiber recording electrodes resembled polytrodes [106, 107], until more recently teams at the University of Michigan and Boston University arrayed fibers on FR-4 and polyimide printed circuit boards (PCBs), respectively, in a similar manner as traditional tungsten microwire arrays [25, 108, 109]. These latter works demonstrated viable recording in both the central and peripheral nervous system using arrays of carbon fiber microwire electrodes, and follow-up work by Patel *et al.* recorded from stable units for three months post-implantation, suggesting their potential viability for a variety of acute and multi-week applications.

Despite this progress, achieving the density desired ($\leq$ 50 µm electrode pitch) is infeasible with current PCB-based approaches. These devices are assembled by manually positioning and aligning carbon fibers on a row of exposed pads at the edge of the PCB (150 µm pitch), and silver epoxy is applied to establish an electrical and mechanical connection between the fiber and pad. While advanced PCB manufacturing process can achieve 25 µm line and space (50 µm pitch), applying silver epoxy at this scale without shorting adjacent pads is prohibitively difficult. Gillis and Lissandrello's 3D-printed alignment clips can circumvent this limitation to some degree, reportedly allowing electrodes to be arrayed at a 20 µm pitch, however this array was one dimensional and would not readily be scalable to a second dimension with pitch on the same order of magnitude [109]. Likewise, Patel's FR-4 PCB-based arrays can be stacked in the second dimension, but pitch between rows of fibers is limited to the thickness of the PCBs (not reported, but estimated 0.5-1 mm from figures) [108].

Beyond these pitch limitations, none of the aforementioned carbon fiber microwire arrays are practically scalable beyond one hundred electrodes; to date, none has exceeded sixteen electrodes. Reasons for this are two-fold. First, these devices are hand assembled, and accurately positioning and aligning each fiber is difficult. As the number of fibers increases, this problem only grows. While silicon or 3D-printed fixtures can ease this challenge somewhat, scaling to one thousand electrodes by hand assembly is infeasible. Second, these devices currently have one connector per PCB, and scaling to one thousand electrodes would require tens of PCBs with tens of connectors fanning out from a small array of fibers. Both connector volume and interconnect area quickly become prohibitively large, and the interfacing electronics (amplifiers, filters, and acquisition system) must be equipped to handle the large number of incoming signals. As was suggested in the preceding chapter, the appropriate solution is to provide a means of either space-efficiently bonding a CMOS die with these electronics, or ideally incorporating the electronics directly into the array itself.

2.2 A silicon-based carbon fiber array can provide the desired pitch and potential for scalability

The pitch requirements stated lend themselves to microfabrication, as few other fabrication techniques are suitable for such fine features, particularly as a combination of conductors and insulators must be integrated into the fabricated device. Further, because a two-dimensional array comprised of stacked linear arrays requiring bulky interconnect of their own is impractical for the reasons stated above, it is necessary to pattern all contacts and interconnect on or into the surface of the wafer, requiring the carbon fibers to extend out of plane. These requirements begin to suggest a two-part construction to the array, with the first part being of a microfabricated substrate with associated signal routing and interconnect, and the second part comprised of the carbon fiber recording electrodes. Because silicon is amenable to CMOS integration or a variety of chip-to-chip bonding techniques in addition to a broad set of standard microfabrication processes, it is the natural choice for the substrate material.

Standing fibers on end on the face of a silicon substrate is infeasible, so such a substrate needs holes or wells etched into or through its face for the fibers to rest. Each hole must then be metallized to provide electrical connectivity to each fiber, and those signals then routed to the appropriate terminus off-chip. This dense routing further reinforces the decision to produce the substrate by microfabrication. Because most silicon wafers are doped to be moderately conductive, all metallization on the wafer must be electrically isolated from the silicon substrate by an insulating thin film. For purposes of this work, as this is a proof-of-concept device, electronics will not be incorporated into the final device; however, no design decision will fundamentally preclude the possibility of bonding a CMOS die to the microfabricated substrate. These considerations will be discussed in more detail in the final chapter.

Given all of the above requirements and constraints, a picture of the device begins to emerge. An array of holes are microfabricated into a silicon substrate, and one carbon fiber recording elec-

trode is threaded through each hole. The signal from each recording electrode is routed from the sidewall of the hole to the top surface of the substrate, and subsequently to a bond pad. Isotropically conductive adhesive (ICA) applied to each hole provides a suitable electrical and mechanical bond between the carbon fiber and substrate. This proof-of-concept array will be limited to only six by six electrodes, thirty-two of which are routed to a standard headstage connector for compatibility with an existing recording interface. The remaining four electrodes can either be left open or not populated. From a layout perspective, six by six is also the largest square array that can be routed with only one trace passing between any pair of holes; thus it proved a convenient starting point. The substrate microfabrication process, however, is fundamentally scalable to any number of recording sites with no change in the design or procedure other than a trivial mask redesign. It is shown in the following chapters that the assembly procedure is likewise scalable.

Quantitative layout design decisions

Selection of a 20 μm hole diameter presents a compromise between topographical impact on photoresist spinning versus ease of assembly. While no optimization was performed in this regard, additional constraints relating to the performance of the ICA (detailed in chapter 4) indicate that this is likely the minimum sized hole in which reliable connectivity is possible using an ICA. Traces were selected to be half as wide as the gap between traces (2 and 4 μm respectively) in anticipation that photoresist would be thicker near the edges of the holes and thus would be more difficult to fully expose. A 2 μm annulus of metal surrounds each hole to allow for moderate misalignment between the holes and metallization while still ensuring connectivity. This 2 μm minimum feature size was deemed to be sufficiently larger than the 0.7-1.0 μm minimum feature size afforded by the i-line (365 nm) lithography tools. Taking these dimensions together, the resulting pitch between holes, and thus recording sites, came out to be 38 μm, which is squarely within the 12-50 μm target range proposed in section 1.4.

Materials design decisions

Silicon was the appropriate material for the substrate due to the broad range of processesing options available and the need for a deep, near-vertical etch. Silicon dioxide then became the natural material to electrically insulate the patterned metal from the silicon substrate, as thermally grown SiO_2 is both conformal and essentially defect-free. Because the inner wall of the hole must be electrically connected to the top metallization, a thin film both conductive and conformal was necessary. Standard physical vapor deposition techniques are nonconformal, and among the chemical vapor deposition (CVD) processes available, only CVD polysilicon and ALD titanium nitride processes were potentially suitable. ALD TiN was chosen for its resistance to passivating oxide formation. While a variety of material options were available for top-level metallization, aluminum can be etched using the same processes as the TiN and thus eliminates an additional process step. Titanium would have been a viable alternative from a processing perspective, but titanium is approximately sixteen times as resistive as aluminum. Because the metal is not in direct contact with physiological fluids, the biocompatibility of this material choice was of secondary

concern. Finally, parylene-C, a conformally deposited insulating polymer widely regarded as a good diffusion barrier suitable for use in implantables, insulates both the substrate and the carbon fibers (excluding the recording sites) from the physiological medium.

2.3 Substrate microfabrication process

Overview: Microfabrication of the silicon substrate is a three-mask process. The first mask defines the holes for the carbon fibers, the second defines the metal routing on the top surface, and the third defines the outline of the device, as shown in Figure 2.1a,b. The substrate, which is monolithically fabricated from a conductive silicon wafer, must be electrically insulating such that the thirty-six channels of routing don't short to one another. A thin silicon wafer is used in order to reduce etching time and ease assembly. These considerations guide the following description of the microfabrication process performed in the Marvell Nanofabrication Laboratory (MNL).

The full microfabrication process flow for the silicon substrate is summarized in Figure 2.1c. First, 150 mm diameter, 280 µm thick double-side-polished prime-grade silicon wafers are cleaned in a 120 °C piranha bath for 10 min, rinsed thoroughly in 18 MΩ water, and spun dry. A layer of 1.05 µm thermal silicon dioxide is grown by wet oxidation in a Tylan furnace at 1050 °C and atmospheric pressure for 3 h. The pattern for the holes extending through the silicon is defined by standard photolithography using a GCA 8500 wafer stepper with 5x optical reduction to expose a 2.8 µm thick film of positive i-line photoresist (OiR 906-12, Fujifilm, Valhalla, NY). Because the 280 µm wafer is thinner than the focal limits of the wafer stepper will tolerate (typically 550-750 µm substrates), the process wafer is temporarily bonded during exposure to a 400 µm double-side-polished handle wafer using a single droplet of deionized water in the center of the wafer. Following exposure, the wafers are carefully separated and the photoresist is puddle developed for 60 s in a TMAH-based developer solution (OPD 4262, Fujifilm, Valhalla, NY) following a 60 s post-exposure bake at 120 °C. Additional photoresist is applied manually to cover any defects in the film. The photoresist is hard baked in a 120 °C oven for 6 h to fully cross-link the photoresist, improving the selectivity of the subsequent plasma etch processes.

Etching the holes through the silicon proceeds in two steps. First, the thermal oxide is etched in an inductively coupled plasma (ICP) for 4 min (15 sccm C_4F_8, 8 sccm H_2, 174 sccm He, 1500 W coil, 350 W bias at 13.56 MHz, 0 °C platen, SPTS Technologies Advanced Planar Source Oxide Etch System, Orbotech, Billerica, MA). Next, 20 µm diameter holes are etched through bulk silicon by deep reactive ion etching (DRIE), stopping on the backside thermal oxide (SPTS Technologies ICP-SR Deep Reactive Ion Etch System, Orbotech, Billerica, MA). Detailed etch parameters are provided in table 2.1. Following the etch, the photoresist is stripped in a Matrix 106 Resist Removal System flowing reactive oxygen species (450 s, 250 °C, 400 W, 3.75 Torr O_2), and the wafers are further cleaned for 10 min in 75 °C RCA2 (5:1:1 H_2O:HCl:H_2O_2) to remove any residual organic residue followed by a rinse in 18 MΩ water as before. The SiO_2 is etched completely in 60 min in 5:1 buffered hydrofluoric acid (BHF), and the wafers are again rinsed and spun dry. The etched silicon is annealed for 10 min at 1090 °C in 10 Torr pure H_2 to smooth the scallops resulting from the DRIE process and round the corners at the mouth of each hole (Epi 200 Centura, Applied

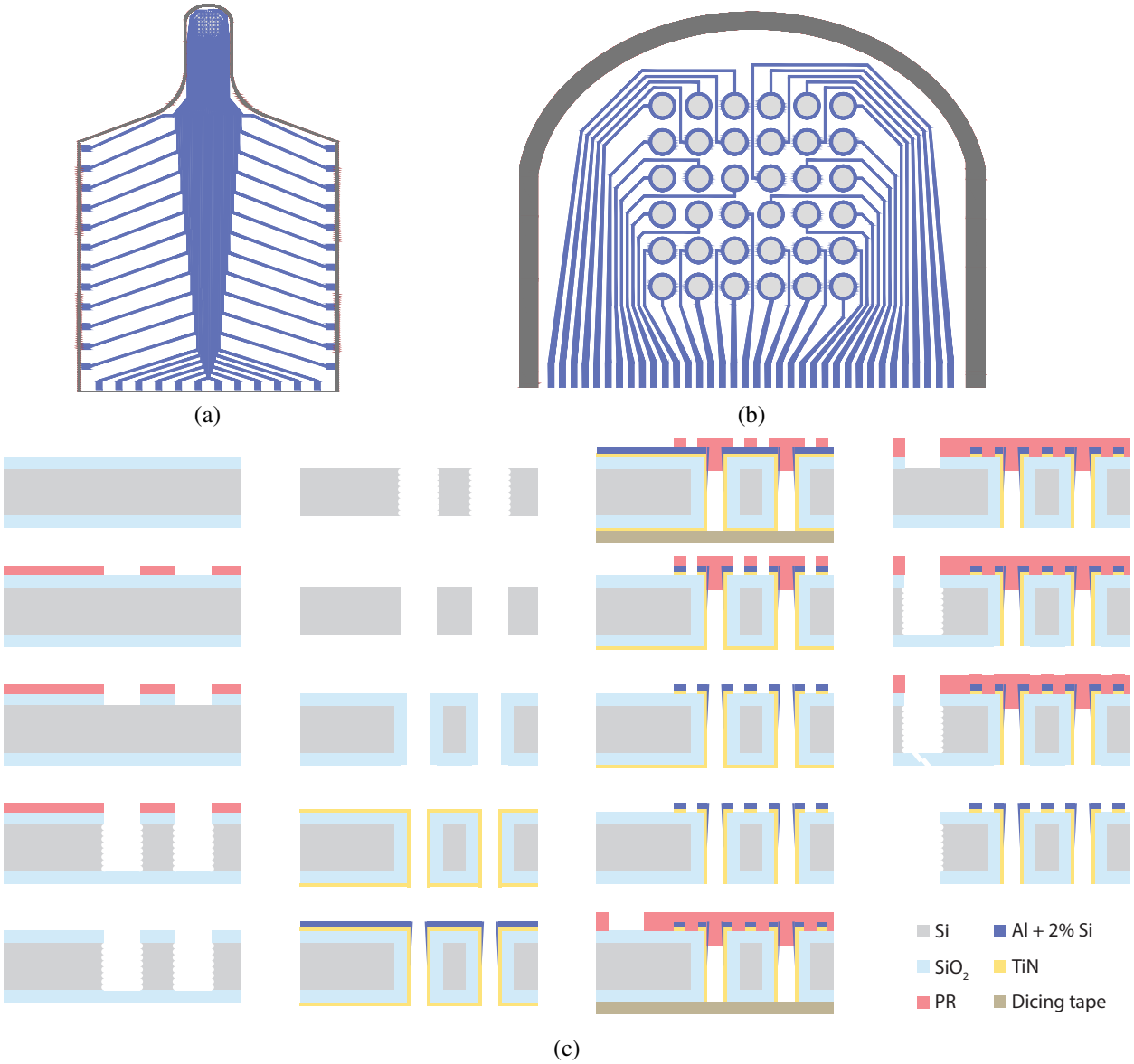

Figure 2.1: (a) Layout (top) view of silicon substrate. (b) Close-up of head of silicon substrate. Through-holes are indicated in red, metal traces in blue, and the device outline singulation etch in maroon. (c) Cross-sectional diagrams of the bulk silicon microfabrication process of the array substrates.

Materials, Santa Clara, CA) [110].

The wafers are then oxidized as before, and 300 cycles of conductive titanium nitride is deposited by plasma-enhanced atomic layer deposition (PEALD) to coat all surfaces of the wafer (Fiji Advanced Atomic Layer Deposition System, Cambridge NanoTech/Veeco Instruments, Waltham, MA), notably including inside the holes, using a modified version of the recipe provided in Burke *et. al* [111]. Following TiN PEALD, the wafer is dehydrated at 200 °C on a hot plate, and 120 nm Al/Si (98%/2%) is deposited in an MRC/TES-944 5 kHz pulsed-DC sputter system (8 mTorr Ar process pressure, 1 kW power, 20 passes at 70 cm/minute; Technical Engineering Services, Santa Cruz, CA). The metallized wafers are lithographically patterned as before with the pattern for the upcoming metal etch, with two notable deviations. First, spinning photoresist now requires that the wafer be backed with a layer of dicing tape (Ultron Systems, 1005R) in order to hold vacuum on the spin chuck due to the through-holes etched previously. This dicing tape is removed during exposure and the post-exposure bake step, and it is reapplied during puddle development, which also occurs on a spin chuck. The second notable deviation is that this layer of photoresist is spun manually, as opposed to using an automated coat track, to accommodate customization of the spin recipe. This customization is necessary due to the severe topography now present on the surface of the wafer and the aggressive feature sizes targeted and proximity to the through-holes. Specifically, the photoresist is dynamically dispensed at 100 RPM for 10 s, after which the spinner is ramped up to 1000 RPM at 100 RPM/s and held at that speed for 30 s before returning to a stop at a rate of -100 RPM/s. Once photolithography is complete, the photoresist is hard baked as before.

Prior to etching the metallization stack, wafers are bonded under vacuum with polyphenyl ether (Santovac 5, SantoLubes LLC, Spartanburg, SC) at 120 °C to standard prime grade handle wafers using a custom wafer bonding tool (Appendix B.2). The aluminum and titanium nitride are etched for 50 s in a TCP metal etcher (Lam Research Corporation, Fremont, CA) using a 200 W plasma of 90 sccm Cl_2 and 45 sccm BCl_3 at 100 W bias. Integrated endpoint detection indicates when the etch has reached the underlying oxide by spectroscopy of the etch products. The process wafer is debonded from the handle wafer and the photoresist stripped by soaking in acetone, with razors inserted around perimeter of the wafer after two hours to provide a small deflection encouraging acetone to flow into the interface and for the wafers to separate. An argon ion mill removes residual TiN from the backside of the wafer (500 V, 300 mA, 10 min, 0° angle, 15 RPM stage rotation; Pi Scientific, Livermore, CA). The high degree of anisotropy inherent to ion milling ensures that the TiN inside the holes is not affected, and less than than 80 nm of SiO_2 is milled from the backside of the wafer as a consequence of the TiN removal.

Lithographic patterning of the device outlines is performed using a 12 µm film of AZ P4620 photoresist (MicroChemicals GmbH, Ulm, Germany) spun at 2000 RPM and rehydrated, exposed, and developed according to manufacturer specifications. After hard baking the photoresist at 90 °C for 30 min, the SiO_2 is etched from within the patterned trench in eight 30 s cycles using the SPTS Oxide Etch System described previously. A 90 s cooldown between etch cycles reduces the heating of the photoresist and thus the risk of destructive crack formation. The Si is subsequently etched as before, but the trench etch is carefully timed to stop on the backside SiO_2 film. The devices are easily removed by breaking the SiO_2 membrane, and the photoresist is stripped in Microposit Remover 1165 (Dow Chemical Company, Midland, MI), followed by subsequent rinses in acetone,

isopropanol, and deionized water.

Table 2.1: DRIE parameters used. Etching through a 280 µm thick wafer required 475 such cycles for 20 µm diameter holes and 420 cycles for 20 µm wide trenches.

Parameter	Deposition cycle	Etch cycle
Cycle time (s)	7	10
Process pressure (mTorr)	18	35
C_4F_8 flow (sccm)	80	0
SF_6 flow (sccm)	0	130
O_2 flow (sccm)	0	13
Coil power (W)	600	600
Platen bias, 13.56 MHz (W)	0	20
Platen chiller (°C)	25	25

2.4 Array substrates can be microfabricated at scale

Fabricated substrates and completed devices are shown in Figure 2.2. Substrate microfabrication yield was 60-70%, limited by the patterning of the 2 µm line, 4 µm space metallization between the vias. Surface tension effects due the topography, as well as inconsistencies in the thickness of the photoresist due to the manual dispense process, resulted in all metal traces on a given substrate either shorting or being completely removed in some regions of the wafer. Defective substrates were quickly identified by eye and removed, and with 912 substrates per wafer this did not present a significant limitation, particularly as it was the only significantly yield-limiting step in the microfabrication process.

Because the occurrence of this yield-limiting defect either affected all or no traces on a given substrate, the yield of a microfabrication process scaled to one thousand recording sites or more is projected to be similar. Further, this limitation can be obviated entirely with a photoresist spray coater (i.e EVG101, EV Group, St. Florian, Austria), which is available in many clean rooms around the world.

2.5 Special considerations and microfabrication process decisions

The microfabrication process presented in Section 2.3 has been designed to be robust and amenable to the subsequent assembly procedure, and many of the design decisions reflect optimizations and trade-offs critical to the repeatability of the process.

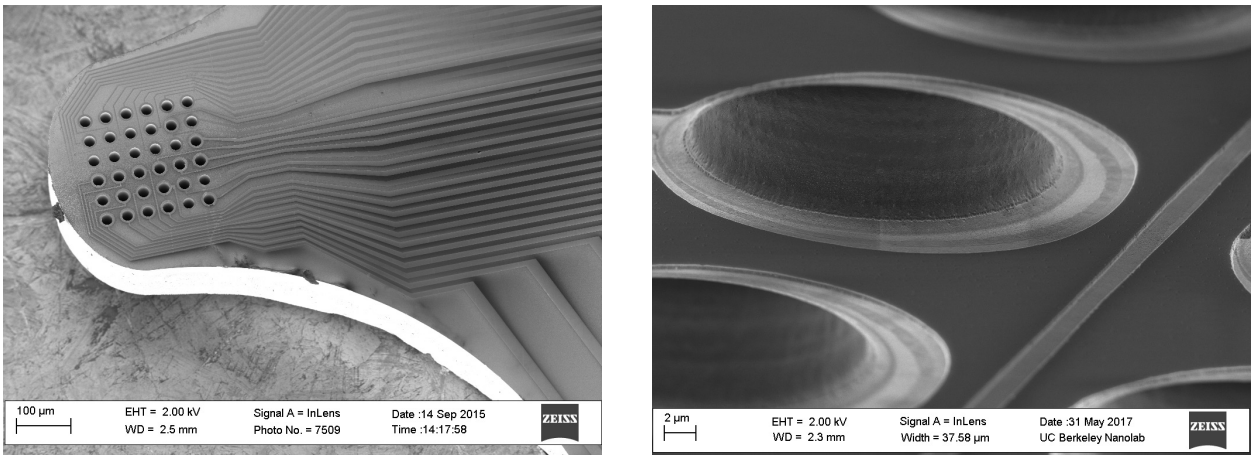

(a) (b)

Figure 2.2: (a) SEM of microfabricated substrate and (b) a close-up on a portion of the head with a view into one of the holes.

Processing thin silicon wafers

First among these decisions was the choice to use thin wafers. Inherent to DRIE is an aspect ratio limitation, such that there is a practical limit to the depth of an etched feature [112]. Even upon optimizing the etch process by increasing process pressure and bias power as a function of depth, the deepest 20 µm diameter cylindrical hole we could etch was 350-400 µm deep. Thinning a standard 525-675 µm thick wafer late in the microfabricaton process would compromise the backside insulating silica and present an opportunity for electrical shorting through the substrate; thus, beginning with a 280 µm thin wafer was deemed necessary.

Processing thin wafers comes with specific challenges, however. First, the wafers are outside the focal range of lithographic steppers, necessitating bonding the wafer to a 400 µm handle wafer as previously described. Second, because the thin wafer is more fragile than a typical wafer, standard temporary bonding methods present an elevated risk to the wafer, whether from trapped air bubbles cracking the wafer under vacuum or the debonding process itself requiring moderate flexion to separate the wafers. A water droplet provided the necessary bonding force for the gentle atmospheric environment of the lithographic stepper, and dicing tape carefully applied to the backside of a wafer allowed processing on low-temperature tools with vacuum chucks, namely photoresist coaters and developers. For plasma etching, in which neither water or dicing tape was suitable, we developed the aforementioned custom wafer bonding tool to enable uniform, void-free bonding of two wafers using a thin film of polyphenyl ether. While mobile electrostatic chucks (MESCs; Beam Services, Inc., Pleasanton, CA) became available toward the later stages of processing, the electrostatic charge dissipated quickly, particularly when placed into plasma tools or on spin chucks for coating or developing photoresist. MESCs ultimately proved unreliable and were abandoned despite significant process/technique development to improve the outcome.

In addition to these wafer bonding challenges, the thin wafers were prone to developing defects

in the oxidation furnace that resulted in significant warping at the edge where the wafer contacted the quartz boat. Because the wafers were no longer flat, additional care was necessary during bonding and cleaning to minimize pressure applied at the edges of the wafers that could result in hairline crack formation.

Alternate methods of wafer thinning

Before deciding to purchase thin wafers, we also explored thinning standard wafers. In an early version of the process, metal deposition and patterning was performed before DRIE to simplify lithography. Processing in this manner left the back side of the wafer and via sidewalls uninsulated after processing. While this might be tolerable with intrinsic (undoped) silicon, using doped silicon would result in unacceptable electrical shorts between channels. Among the methods investigated for thinning the wafers were etches using KOH, XeF_2, and SF_6. In each case, the insulating material, SiO_2 or low-stress silicon nitride (LSN) was removed prior to silicon etching with an ICP etch.

KOH etching was performed using a screw-tightened polyether ether ketone (PEEK) wafer holder designed for wet etching (AMMT GmbH, Frankenthal, Germany) to protect the front side of the wafer while immersed in a bath of 24% KOH maintained at 80 °C. LSN deposited by LPCVD was used to electrically insulate the metallization on the wafer from the substrate instead of SiO_2, as LSN provides better resistance to KOH than SiO_2. While the KOH was effective at uniformly etching the wafer, trapped air behind the O-ring-sealed wafer exerted a large force on the wafer and could easily break it below 200-250 µm. This pressure differential caused more significant problems in early versions of the fabrication of the alignment device described in section B.1, which was only 15-17 µm thick. Further, the residual ring of thick silicon left at the edge of the wafer where the O-ring made contact meant that the backside of the wafer wasn't flat. Non-flat wafers are not acceptable in many cleanroom processing tools, and thus this method for wafer thinning was rejected.

The XeF_2 wafer thinning process similarly used a front-side masking material, but the selectivity of the XeF_2 etch to silicon over the other materials present (SiO_2, Au, Pt, and TiN). XeF_2 etching was performed in an Xactix XeF_2 Release Etch System (SPTS Technologies Ltd., Newport, UK) with 3.5 torr XeF_2 in 30 s cycles; however, even for a square die 22 mm on a side, over one thousand cycles were necessary to sufficiently thin the silicon. Because the etch is XeF_2 limited, this will increase with exposed area and etching full wafer will be prohibitively slow. Further, the etch was nonuniform, etching faster at the edges and resulting in a dome-shaped profile. While the shower head holes through which the XeF_2 flow can be selectively plugged to control the local quantity of etchant in the process chamber to combat this nonuniformity, the speed of the etch rendered the matter moot.

Finally both a standard DRIE process (alternating fluorcarbon passivation and etch cycles) and blanket SF_6 etches (no C_4F_8) were tested. The excessive silicon area exposed during the DRIE process causes pillar formation on the wafer due to incompletely removed C_4F_8. Blanket SF_6 etching resulted in a dome-shaped etch profile, as the process gases were largely consumed at the edges of the wafer, and the distribution of process gas in in the DRIE tool was not controllable.

Doubling the gas flow was beneficial, and this process was sufficient for thinning the first generation of process wafers, but this process proved inadequate in later generations when processing following thinning became necessary and the dome was intolerable. The directionality of the SF_6 etch was sufficient to protect the patterned front side of the wafer without a specifically selected masking material.

Hydrogen annealing to smooth via sidewalls

Hydrogen annealing was helpful following DRIE in order to smooth the sidewalls for two reasons. First, the sidewall scallops resulting from DRIE would shadow the sputtered aluminum deposition, resulting in a discontinuous film along the sidewall of the via (Figure 2.3a,b). While the TiN film deposited by PEALD ensures coverage of the via sidewall, this additional coverage with aluminum reduces the resistance of the conductive film stack near the top of the via and doubly ensures continuity where it is most critical. Second, this annealing process results in rounding at the lip of the via (Figure 2.3c,d), which makes it more energetically favorable for photoresist to enter the vias. This photoresist not only protects the vias and their sidewall metallization from the subsequent etch processes, but also greatly diminishes the streaking effect of spinning photoresist over deep topography.

Spinning photoresist over severe topography

To this latter point, spinning and patterning the photoresist near the vias presented a particular challenge, as the finest features in the process needed to be resolved immediately beside and between these aggressive topographical features. Because such topography is known to result in photoresist streaking during the spin process, and the dense square grid of holes presents an unfavorable energy landscape for photoresist coverage, the specific spin-coating process described above was critical. The dynamic dispense allows coverage of the holes without trapped air inside the vias creating thick bubbles of photoresist around the holes, while still avoiding surface energy-generated voids of photoresist in a close radius around the entire array of vias. The slow ramp rate and spin speed ensure that the photoresist doesn't streak and is not removed from the vias, while still being fast enough to provide complete wafer coverage and uniformity of the photoresist film. Spinning or ramping too quickly can result in photoresist either being irregularly thin among the array of holes or receding entirely (Fig. 2.4).

Before this procedure was finalized, several unsuccessful methods of spinning the photoresist were tested. Automated photoresist dispensing programs on the coat tracks resulted in terrible streaking ("comets"). Dispensing the photoresist statically (as a puddle) and letting it rest and spread on the wafer rather than dispensing dynamically (while spinning) resulted in trapped air pockets inside the vias. The air (and released solvent) expanded during soft bake, causing the photoresist to locally swell and become difficult to fully expose and develop. A second exposure and devleop step (*i.e.* spin, expose, post-exposure bake, develop, expose, develop) can help to clear the thick photoresist, but this process was unreliable and often resulted in over- or under-exposed features.

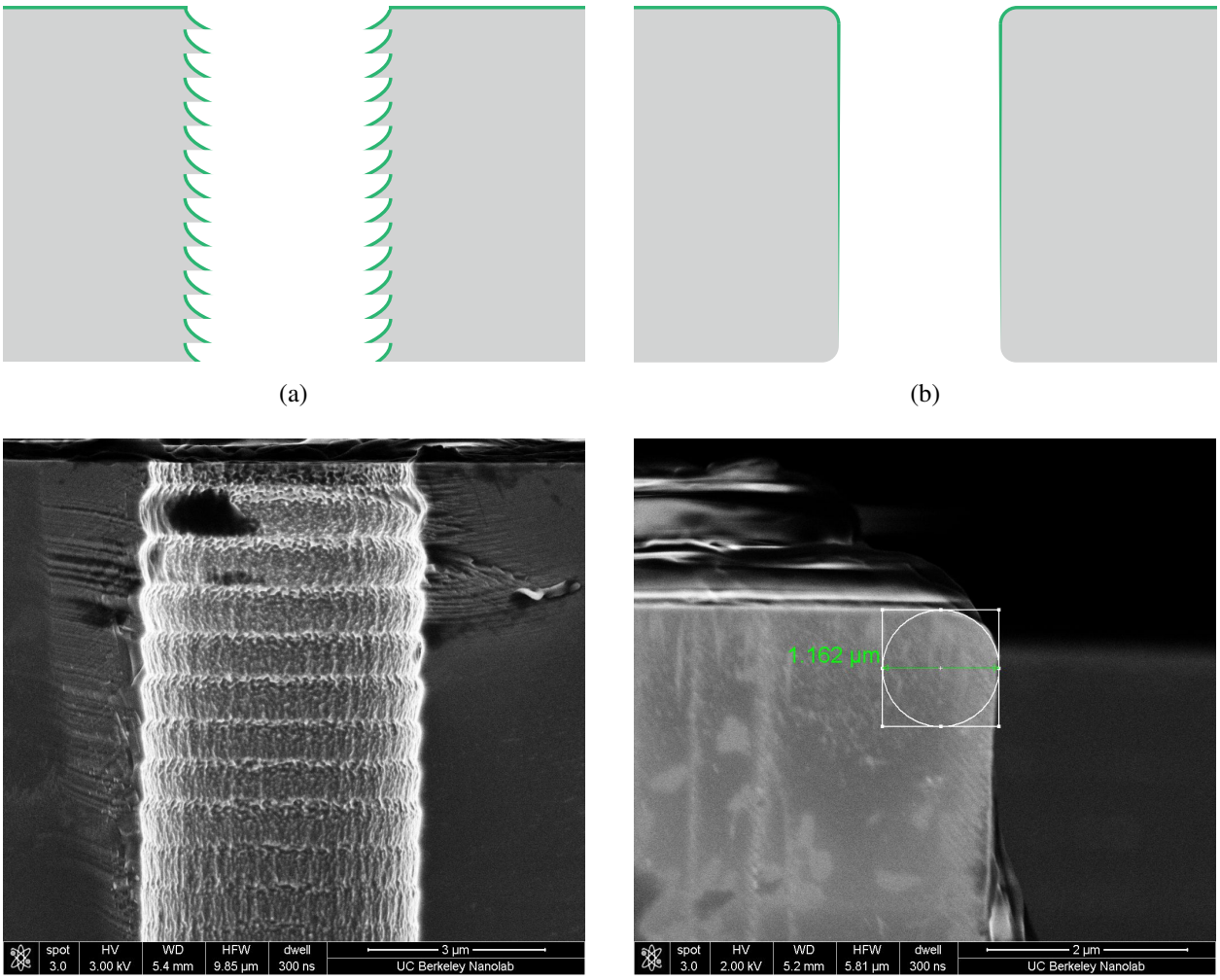

Figure 2.3: (a,b) Diagrams illustrating the effect of scalloped (a) and smooth (b) sidewalls on sputtered metal (green) deposition. (c,d) SEMs of silicon etched by DRIE before (c) and after (d) hydrogen annealing to smooth the sidewall and round the top corner.

Layering several films of spun and soft baked photoresist can also help to planarize the photoresist, but several problems arise [113]. First, accumulated stress at the interface of successive layers causes the photoresist to become brittle and crack or delaminate. Further, the interfaces present an optical mismatch at which some of the incident light is reflected, making it difficult to fully expose the lower layers. Soft baking the lower layers of photoresist for reduced time can mitigate these effects, but the increased soft bake time to which the bottom layer of photoresist is subjected still typically results in the photoresist being difficult or impossible to fully develop.

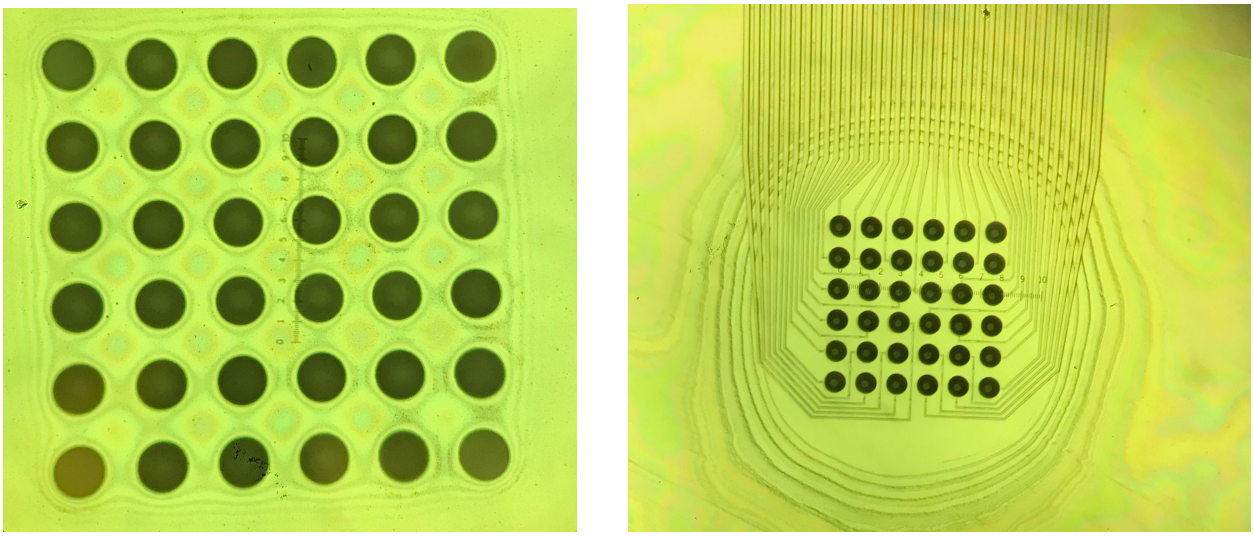

(a) (b)

Figure 2.4: Optical photographs of photoresist (a) displaying irregular thickness and (b) having receded from the hole array due to surface energy effects. Both are effects of spinning photoresist too quickly or not adequately covering or filling the vias.

Another popular planarazation technique attempted is to fill deep structures with photoresist, then use an oxygen plasma to etch the photoresist back to the surface of the wafer [114]. This would provide a smoother wafer surface over which to spin a second layer of photoresist for lithographic patterning. This so-called etch-back technique can work well for large trenches, but air trapped in the vias keep them from filling with photoresist. When the photoresist is ashed back, the holes are once again exposed, leading to similar or worse comets on the next coating of photoresist (Figure 2.5). Lift-off resist (LOR; LOR-5A, MicroChem Corp., Westborough, MA) doesn't cross-link, and as such isn't susceptible to hard baking, allowing it to be reflowed at a temperature above its glass transition (T_g) of 195-200 °C. While reflowing LOR can ameliorate thickness variations due to comets, it also allows surface tension effects to take effect near topographical boundaries, namely at the edge of the via. This can be seen in Figure 2.5 where the photoresist has formed bridges between adjacent vias. Notably, however, LOR has better adhesion to most substrates than photoresist, and may yet be helpful in surface tension-limited scenarios such as that depicted in Figure 2.4b.

Because many challenges relate back to air trapped inside the vias, attempt was made to remove air from the vias after dispensing photoresist by transferring the wafer to a vacuum chamber immediately after spinning resist (before soft baking). The chamber was pumped to a base pressure of approximately 1/50 atm within 30 s and held for 5 min. While this didn't significantly increase the solvent evaporation rate, the pressure differential also was ineffective in removing most trapped air from inside the vias.

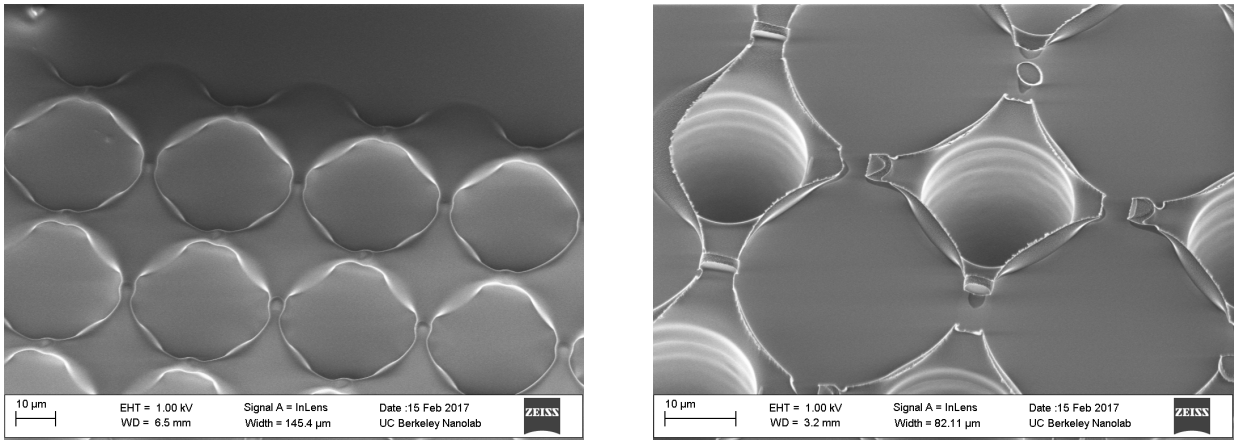

(a) (b)

Figure 2.5: SEMs of reflowed 1.0 µm LOR-5A photoresist spun over vias both (a) before and (b) after etching the resist back with oxygen plasma. The photoresist forms a bubble over the top of the via, trapping air inside. When ashed back, the hole is once again exposed.

Choice of TiN over Ru ALD

In addition to the aforementioned oxidation resistance, titanium nitride was selected as the ALD material for its conductivity, ease of deposition, and ease of etching. The only other available conductive film that can be deposited in the Marvell Nanofabrication Laboratory (MNL) is Ru/RuO_2. Whether the film deposited using the Bis(ethylcyclopentadienyl)ruthenium(II) (Ru(EtCp)2) was Ru or RuO_2 is controversial; however deposition did not yield a reflective surface, and oxygen contamination in an ALD process chamber without a turbomolecular pump is speculated to result in inadvertent RuO_2 deposition. Equipment to conclusively determine the film composition was unavailable. Regardless, Ru and RuO_2 are also less straightforward to etch (Ru is noble), and thus TiN was the appropriate choice.

Soldering and brazing using thin-film deposited metals is an ineffective method of contacting fibers

The process described above is the third generation process developed, with the significant impetus for each redevelopment tracing back to challenges forming a reliable electrical connection between each carbon fiber and the associated metal annulus and trace for a given via. While the process of forming this connection and the considerations therein are be discussed at length in Chapter 4, the relevant microfabrication processes of the first two generations and the resulting limitations are best discussed here.

The first generation substrate had a metal stack of evaporated gold, evaporated platinum, and sputtered titanium nitride. The titanium nitride served as a high-temperature-compatible adhesion layer, the platinum as a diffusion barrier and potential wetting layer for the gold, and the gold was

both the primary conductor and a favorable choice for wire bonding. Titanium nitride is reported to remain effective as an adhesion layer and diffusion barrier up to 1100 °C, whereas titanium begins to fail as an adhesion layer for platinum at 600-700 °C due to interdiffusion [115–117]. Because the titanium nitride was deposited in a separate system from the noble metals, it was necessary to break vacuum. To minimize physisorption of compounds from the air that could interfere with adhesion, the wafer was exposed to air only for the absolute minimum time necessary to move from the sputterer to the evaporator (less than 3 min).

In this first generation process, the thought was to anneal a gold-coated carbon fiber to the gold annulus, which overhung the via slightly, based upon the observation that gold-coated carbon fibers would electrically bond to evaporated gold lines on a chip at temperatures ranging from 250-500 °C, well below the bulk melting temperature of gold (1064 °C). This annealing and surface reflow phenomenon has been previously documented [118, 119]. The substrate was heated in air using a 6 W, 450 nm laser; however, a reliable electrical continuity was established between fiber and annulus approximately only one quarter of the time using this method, and the bond had no mechanical strength. Because reflow only occurred on the surface layers of atoms where the liquidus temperature is significantly depressed [118], formation of even a minuscule bond depended upon fortuitous positioning of the fiber in the hole such that it contacted the annulus. Any lithographic misalignment resulting in lateral shift of the annulus could further reduce the chances of a successful contact.

Because this process depended upon an imperceptible contact, the process was revised in the second generation to use a 80% gold, 20% tin (by mass) fluxless solder composition deposited by evaporation (300 nm Au, 400 nm Sn, 300 nm Au), to form a larger-area contact [120–125]. Though less costly, tin-rich gold-tin eutectic compositions are undesirable because they are brittle and prone to oxidation [126]. Still, the odds of the gold- or gold-tin-coated fiber contacting the gold-tin annulus were small, and yield was still approximately 25%.

These methods of soldering and brazing between a metal-coated fiber and the annulus around each hole were found to be ineffective; thus, in the final generation of devices steps were taken to doubly ensure that the interior of the via was electrically conductive (ALD and metal sputtered on a smoothed sidewall). Further, we moved to using an isotropically conductive adhesive to form the electrical and mechanical connection between the fiber and substrate as detailed in Chapter 4.

2.6 Conclusion

Through this chapter I have established the limitations of conventional microwire neural recording arrays, the need for a carbon fiber neural recording array and the high-level design thereof, and the steps and considerations involved in the microfabrication of the silicon substrate for such a device. However, a silicon substrate is far from being a functional neural recording array; this is only the first step in the process. The upcoming chapter investigates how one might scalably assemble such an array by automating the steps that will scale with the number of electrodes.

Chapter 3

An automated system for inserting carbon fibers during the assembly process

Adapted with permission from:

Massey TL, Lee JH, Ray M, Sathe NS, Liu X, Pister KS, Maharbiz MM *"Open-source automated system for assembling a high-density microwire neural recording array"* in IEEE Manipulation, Automation and Robotics at Small Scales (MARSS), July 2016.

3.1 Introduction

Assembly at the microscale involves manipulation of one or more components relative to another in order to create a microstructure or device that would be difficult or impossible to monolithically fabricate. One specific class of problems that is well suited to microassembly rather than microfabrication is the creation of very high aspect ratio out-of-plane microstructures. As size and complexity of these out-of-plane microstructures grows, it becomes compelling if not necessary to automate the device assembly. This chapter presents an automated assembly system for one such device, a microwire array for intracortical neural recording and stimulation in animals.

The current goal in the development of neural recording arrays is to fabricate an array with thousands of recording sites that is fine and compliant enough to not cause an adverse biological response, which degrades recordings [55],[84]. Prior work suggests that glial encapsulation of fibers does not occur below diameters of 6-12 μm [77, 78]. The ideal array also has electrodes

spaced at a pitch of 30-50 µm such that each unit is recorded at multiple sites in the array and the spatial arrangement of neurons can be determined [106, 127]. Among planar arrays [28], silicon shank Michigan style probes [24], monolithic Utah arrays [26], and microwire arrays [25], the four major classes of neural recording arrays, microwire arrays are currently the most broadly used. Microwire arrays are still almost exclusively hand-assembled [42, 44], however, which limits the extent to which we can increase the electrode count and the reduce the size and pitch of the electrodes. Here we describe an automated assembly system to address this limitation.

Microwire arrays generally have three components: the microwires that penetrate the cortex, a substrate to which the microwires are connected above the surface of the brain, and a backplane to interface with a headstage or recording system. The substrate and backplane may be integrated into one component, but together route signals from the individual electrodes to the back-end interface connector. Connections from the substrate to the backplane may be established by standard techniques including wire bonding, flip-chip bonding, conductive adhesive, or even soldering, but it is less trivial to electrically connect the microwires to the substrate. Our array uses 5.4 µm carbon fiber monofilaments in place of traditional 12.5-25 µm tungsten microwires. These 1-4 µm long fibers extend through 20 µm through-silicon vias etched in a microfabricated silicon substrate at a pitch of 38 µm. Each substrate via is surrounded by a patterned metal annulus that is routed to a bond pad. The substrate is wire bonded to a polyimide printed circuit backplane that routes the microvolt-level neural signals to a standard headstage connector.

Assembly steps that occur only once per device may reasonably be performed manually, but it is necessary to automate steps that are performed once per electrode in order for the array to be feasibly scalable to hundreds or thousands of electrodes per device. To underscore this point, manually inserting 36 carbon fiber electrodes through this substrate takes 2-4 hours for someone experienced with the procedure. To address this scalability limitation and increase throughput, this system automates the process of inserting carbon fibers and electrically connecting them to the substrate.

Many automated or otherwise scalable techniques for microscale fabrication and assembly exist, but none are singularly suited to creating microwire arrays. The ideal automated assembly technique fulfills the following requirements: (a) accurate and repeatable positioning with single micron resolution; (b) able to manipulate flexible microwires with $>$ 1000:1 aspect ratio; (c) minimize electrostatic and hygroscopic/capillary interactions that could cause the fibers to deflect or bundle [107]; (d) be comprised primarily of affordable off-the-shelf components so that the system is reasonably reproducible by others. Unfortunately, microwire arrays are traditionally hand-assembled because there are no such suitable options for out-of-plane assembly.

Microassembly techniques are broadly grouped into two categories, parallel and serial processes. Parallel (batch) process may be further subdivided into three subcategories. The first of these subcategories is wafer scale processing, such as in MEMS processing or flip chip bonding [128, 129]. Second, partially stochastic motion of a free element over a carefully designed mechanical, biological, chemical, or electrostatic trap structures or binding sites on a static element may be employed to selectively capture one or more components relative to some static element. Cohn presents a thorough review of such techniques [130]. Third, application of some force or environmental stimulus (electrostatic, capillary, magnetic, thermal, pressure) may induce

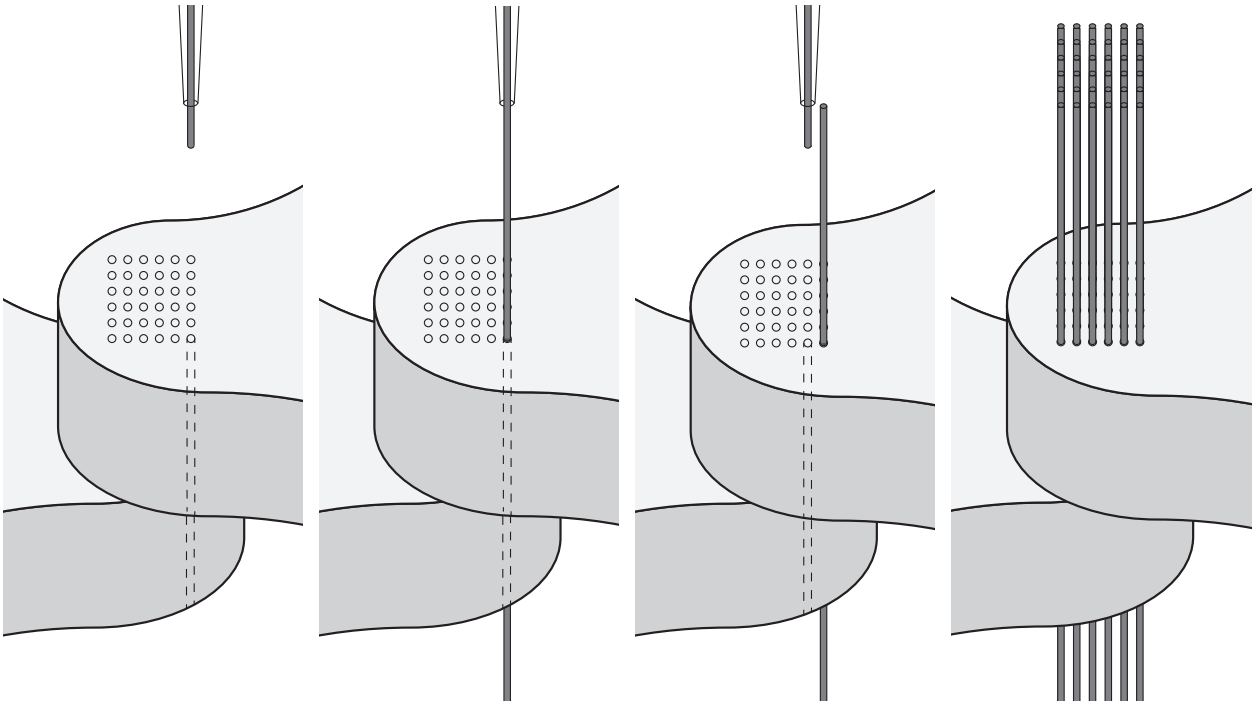

Figure 3.1: The procedure of feeding carbon fibers through substrate vias is shown (not to scale). Two substrates' via arrays are aligned. (a) A glass capillary with a single long fiber is aligned to the first via. (b) The fiber is fed down through the via and subsequently cut to length. (c) The capillary is aligned to the next via. (d) After iterating, fibers have been inserted through all vias.

a semi-permanent conformational change in a structure [131, 132]. Serial assembly processes typically involve mechanical manipulation of individual elements [133], but the additional degrees of freedom (DOF) afforded by individual mechanical manipulation enable more complex structures to be assembled. The complexity of mechanical micromanipulators ranges from tungsten probes to sophisticated microgrippers mounted on 5-DOF robotic arms [134]. Serial assembly processes can be effective, but not only is throughput limited, the sophisticated mechanical manipulators can be prohibitively costly. This pair of limitations can render serial microassembly uneconomical for either high- or low-volume applications. Thus, cost and throughput must both be factors in the design of any serial microassembly system.

Our neural recording array design necessitates a serial assembly approach given the aspect ratio of the carbon fiber monofilament, but throughput requirements are low. Care was taken to ensure that the design is financially accessible to those who wish to replicate the system, using off-the-shelf components wherever possible. The assembly system described herein is comprised of a monofilament feeder, a sub-micron three-axis positioning platform, and a vision system to track the substrate, as well as the necessary vision and control algorithms to automate the carbon fiber threading portion of the array assembly. Following the design, we present and discuss the perfor-

mance of the system. Included is a comparison of several micropositioning methods generalizable to many micropositioning applications.

3.2 Methods

The basic functionality of the automated assembly system is to serially insert carbon fibers through the substrate vias. The feeder assembly and camera are stationary, and the substrates mounted on the substrate platform are micropositioned directly above the camera and below the feeder capillary. The substrate plaform is stepped, via by via, until the substrate is fully populated with fibers. Fig. 3.1 illustrates this process. Once all fibers have been inserted, a laser is used to heat the substrate to either cure an isotropically conductive adhesive or reflow thin-film solder to join the fibers to the substrate both electrically and mechanically.

The system has several major hardware components and key algorithms central to the automated assembly process. Three linear stages precisely position the substrate platform along the Cartesian axes. The substrate platform holds the substrates and alignment micropositioners, as well as the laser. The camera provides visual information to supplement the feedback from the incremental linear optical encoders on the linear stages. A feeder assembly is responsible for feeding the carbon fiber through each substrate via. Finally, a custom program written in MATLAB controls the three linear stages, the feeder, laser, and coarse vertical positioning of the camera. A model of the system is shown in Fig. 3.2.

Several components of the system are included for one-time or once-per-array alignment steps, namely the two micropositioners holding the substrates, the laser alignment micropositioners, and the feeder alignment micropositioner. Because these components are aligned at most once per device, it is less critical that these alignment steps are automated compared with N-per-device micropositioning operations. Additionally, fibers are fed through two device substrates in order that, later in the assembly procedure, the substrates may be manually vertically separated using the micropositioners to ensure that all fibers are parallel. The laser reflow step has been automated for safety.

Linear Micropositioning System

We use three 300 mm Parker Daedal 404XR precision stages equipped with Compumotor ES21B stepper motors for x,y, and z-axis movements. The x and y stages are equipped with Renishaw RGH24Y read heads and RGS20-S scales to encode position within 0.1 µm. The stepper motors, driven at 0.2 A by Gemini GT digital stepper drives and a 6K4 motion controller, also from Parker, drive 5 mm lead screws at 25000 counts per revolution. We set running and standby current to double that required to reliably move the motors and hold their positions, respectively. The positioners are rated to have an accuracy of 14 µm and a bidirectional repeatability of 1.3 µm, but with 0.1 µm encoder resolution and 0.2 µm microstep resolution, reliable sub-micron positioning is possible with feedback. We run the stages at $5\,\mathrm{mm\,s^{-1}}$ with a $50\,\mathrm{mm\,s^{-2}}$ S-curve acceleration profile.

Feeder Assembly

The feeder assembly advances the carbon fiber monofilament through each substrate via positioned beneath. A stepper motor with rubberized drive shaft drives a fixed-position idler bearing by direct contact. A freely pivoting swing arm with a second end-mounted idler bearing descends from above the fixed idler bearing. The weight and off-vertical angle of the arm producing a torque to hold this swinging idler bearing against the fixed idler bearing. The fiber is symmetrically constrained by the two idler bearings, and is fed downward as the stepper motor turns the directly coupled idlers.

The feeder assembly is built into an aluminum frame and suspended from a horizontal mounting rod by a two-axis manual micropositioner for one-time manual alignment of the feeder capillary to the center of the camera's image. The twenty step per revolution motor is controlled using an Arduino microcontroller with Adafruit Motor Shield driver to advance the fiber approximately 300 µm per step. Glass capillaries guide the fiber between the feeder wheels and toward the substrate. The lower capillary is pulled to a 6-8 µm tip to enforce precise positioning of the fiber relative to an aligned substrate via.

The lower capillary is formed by heating a borosilicate glass capillary tube (Chemglass CG-1182-02) over a flame and manually and pulling it to a point. Excess length of the capillary tubing beyond approximately 2.5 cm is carefully broken off by hand and discarded. A carbon fiber is inserted in the remaining short segment up until the capillary closes off and it can progress no further. Once the fiber has reached this endpoint, it is assumed that the inner diameter of the capillary is equal to the diameter of the fiber. A quartz scoring scribe is used to score and fracture the glass as close as possible to this point.

Once the fiber is inserted through each via, the fiber is cut near the tip of the lower capillary. In the current instantiation of the feeder assembly this is done manually with a pair of fine surgical microscissors, but in an upcoming revision this will be automated with another computer-controlled servo driving a blade mechanism anchored in a precise location.

Vision System

The camera (2 MP OEM USB microscope), mounted beneath the feeder and substrate platform, provides visual feedback to the system through a MATLAB interface and is used to locate the substrate vias. This camera was chosen largely for its narrow form factor, which allows easy integration into the system. The sensor resolution was deemed less critical, as it is often lens quality and sensor noise that ultimately limit the effective resolution of inexpensive USB cameras; however, additional tests employing sub-pixel interpolation demonstrated that there may yet be some benefit in a higher resolution sensor with similar pixel noise characteristics.

In order to ensure that the camera is vertical, it is mounted on a kinematic mirror mount providing two degrees of freedom of fine adjustment. The camera is coarsely positioned vertically by a stepper motor with a lead screw driving a one-inch linear translation stage. This enables the camera to be moved out of the way during large stage movements or when the laser is active. The

substrate is finely positioned relative to the camera by adjustment of the z-axis micropositioning stage to bring the image into focus.

The image is focused automatically, as per [135]. With the substrate initially positioned above the focal plane, the camera captures an out-of-focus image and computes a one dimensional Fourier transform upon several vectors sampled from the image. We lower the substrate in 20 µm increments toward the camera, capturing a new image at each increment. The Pearson's correlation is computed between the first image and each subsequent image, with the minimum correlation indicating the best-focused image. Compared to standard autofocus algorithms based on contrast detection, which compute the global variance of a series images and take the image with maximum variance to be the sharpest image, this method samples only a limited number of vectors and thus scales more favorably with image resolution. [135] showed a three hundred-fold improvement in execution time for an image of similar resolution.

Via Identification and Positioning

To identify substrate vias, we compare a grayscale image of the substrate and a template image of a single via by cross-correlation. The thirty-six points with highest cross-correlation values are determined to be substrate vias. The via identification algorithm checks to confirm that cross-correlation peaks are approximately spaced at expected spatial intervals in order to rule out duplicates or other false positives. Once all vias have been identified, we stably sort them by their x positions. If the x positions of two vias are within one pixel of each other, the vias are additionally sorted by their y values to ensure robust sorting. The system steps through the vias in this order during the fiber feeding process.

In order to determine the appropriate positioning method for this and similar applications, we compare several positioning techniques: open-loop with and without compensation for nonlinearities, closed-loop with visual feedback, and closed-loop with encoder feedback. For each method, we compare the positional error and the time required to complete each positioning task.

Open-loop testing proceeded by first establishing an approximate baseline relationship between stepper counts (microsteps) and pixels by moving 1000 stepper counts and measuring the pixel distance moved. We repeat this test several times to average out minor variation in the individual measurements. Because of nonidealities in the motors and stages, this relationship may not match theoretical predictions for small movements and is non-constant. We use pixels as the base unit of movement in our tests rather than counts or microns because pixels are our measured quantity to determine the distance moved. Pixels and microns can be converted interchangeably for a given image since the precise center-to-center spacing the vias is known, but for consistently of this conversion factor, the relative positions of the camera and substrate were not changed throughout any of the subsequent tests.

Once this pixel-to-count conversion factor is established, we step each axis in integer numbers of intended pixel distances, from 1 to 125 pixels, in both the positive and negative directions. Twenty movements are made at each pixel value, and the pixel distance moved is measured. The order of all movements is randomized to eliminate potential systematic bias. We perform this test for twice both x and y axes, first incurring backlash with each movement, and second with

backlash eliminated. Motor backlash is present whenever the motor reverses direction, so backlash is eliminated by ensuring that each measured movement follows a prior motor movement in the same direction.

The initial open-loop tests may be used to quantify the nonlinearity of the open-loop operation of the stepper motors and linear stages. We fit the input-output motion relationship for each axis to a seventh-order polynomial function and repeat the tests with this function applied to each movement to determine whether the open-loop nonlinearity can be characterized and repeatably calibrated out in a given system. Optical nonlinearities were observed to be negligible and are thus not considered in this characterization.

Closed-loop testing with vision feedback began by establishing a similar initial relationship between stepper counts and pixel distance in both x and y directions for a 200 stepper count movement. The algorithm estimates the pixel distance to the center of the current via, and then calculates based on that relationship the number of stepper counts to move and repositions the substrate accordingly. This process repeats iteratively until the via is centered to within ± 1 pixel. This test is repeated twenty times for the full set of vias.

The process for closed-loop positioning with encoder feedback assumes each encoder count corresponds to exactly 0.1 µm. Because the distance between vias is precisely known, the encoder distance in each x and y may also be known. Because x and y stepper movements don't necessarily correspond with the camera's notion of x and y, an initial 1000-count movement is taken in each axis to establish the rotation of the image and an approximate relationship between motor counts and encoder counts. With this information, the algorithm computes the target encoder position of each substrate via in the array. Note that these positions may be computed for all thirty-six vias initially and remain invariant throughout the test. The algorithm attempts to successively move to each position until it is within a margin of eight encoder counts, or approximately one pixel distance in the current configuration, for ease of comparison with the visual feedback testing. As before, the test is repeated twenty times for the full set of vias.

Laser Module

Once all fibers have been inserted through the substrate vias, a 6 W maximum continuous power, 450 nm diode laser may optionally be used to heat the substrate to cure silver epoxy deposited in the holes to bond the fibers electrically and mechanically to the substrate. The laser module is press-fitted into an aluminum heat sink and mounted to manual micropositioners, allowing precise angular (θ) and radial (r) alignment. We use an Arduino interfaced with MATLAB to control the laser, and custom electronics to tune the current through the laser.

Because safety with any Class IV laser is of primary concern, three switches must be closed for the user to engage the laser: a toggle switch on the electronics module, the Arduino-controlled relay, and an interlock switch built into the aluminum enclosure surrounding the entire assembly system. The enclosure is sealed such that no specular reflections can escape. For additional safety, a single-element lens rapidly defocuses the laser beyond 50 mm. Furthermore, to minimize risk while tuning the laser, a voltage and current readout for the laser diode is mounted on the front panel. These engineering controls serve to minimize the risk to users and bystanders.

Graphical User Interface

In addition to scripts that fully automate the assembly process, the system may be controlled through a graphical user interface (GUI), enabling the user to manually control each step as desired. Features include:

Start/Stop Camera Enable/disable live image acquisition

Autofocus Automatically focus the image

Mark Allow the user to manually overlay a marker on the image

Capture Image Save a still photograph of the camera's current view

Kill Immediately cease all motion of the stages

Find Holes/Clear Find and mark all holes in the image, or clear all markers

Center Hole Center the image on a user-specified hole number

Move Substrate Move the substrate a user-specified number of counts (x,y,z)

Measure Initiate an automated measurement to relate x and y motor counts to pixels

Left/Right/Up/Down Move the stage such that the *image* moves in the $\pm x, y$ direction

Raise/Lower 100 Move the stage up or down by 100 motor counts for quick focus adjustment

Laser Enable the laser for a specified number of seconds

Feeder Go Advance the feeder by a given number of motor steps (retract if negative)

3.3 Results and Discussion

Repeatable Identification of Through-Silicon Vias

The vision system can repeatably identify the center of all thirty-six vias within a ± 1 pixel error, or about 0.8 µm, on an empty substrate (Fig. 3.3a). This one-pixel variability is attributed to the computational methods used to locate each via. Using standard sub-pixel interpolation, this variability can be reduced by over one order of magnitude; however, sub-pixel interpolation is extremely computationally costly and was deemed impractical and unnecessary given the positioning requirements of our application.

Comparison of Positioning Methods

Once the vias have been identified, the micropositioning system must successively center each via in the image in order to feed a fiber through each via. We found through our comparison of positioning techniques that feedback is necessary to consistently center each via within an acceptable margin of error. Visual feedback was used to center the right-most via in Fig. 3.3b to within one pixel.

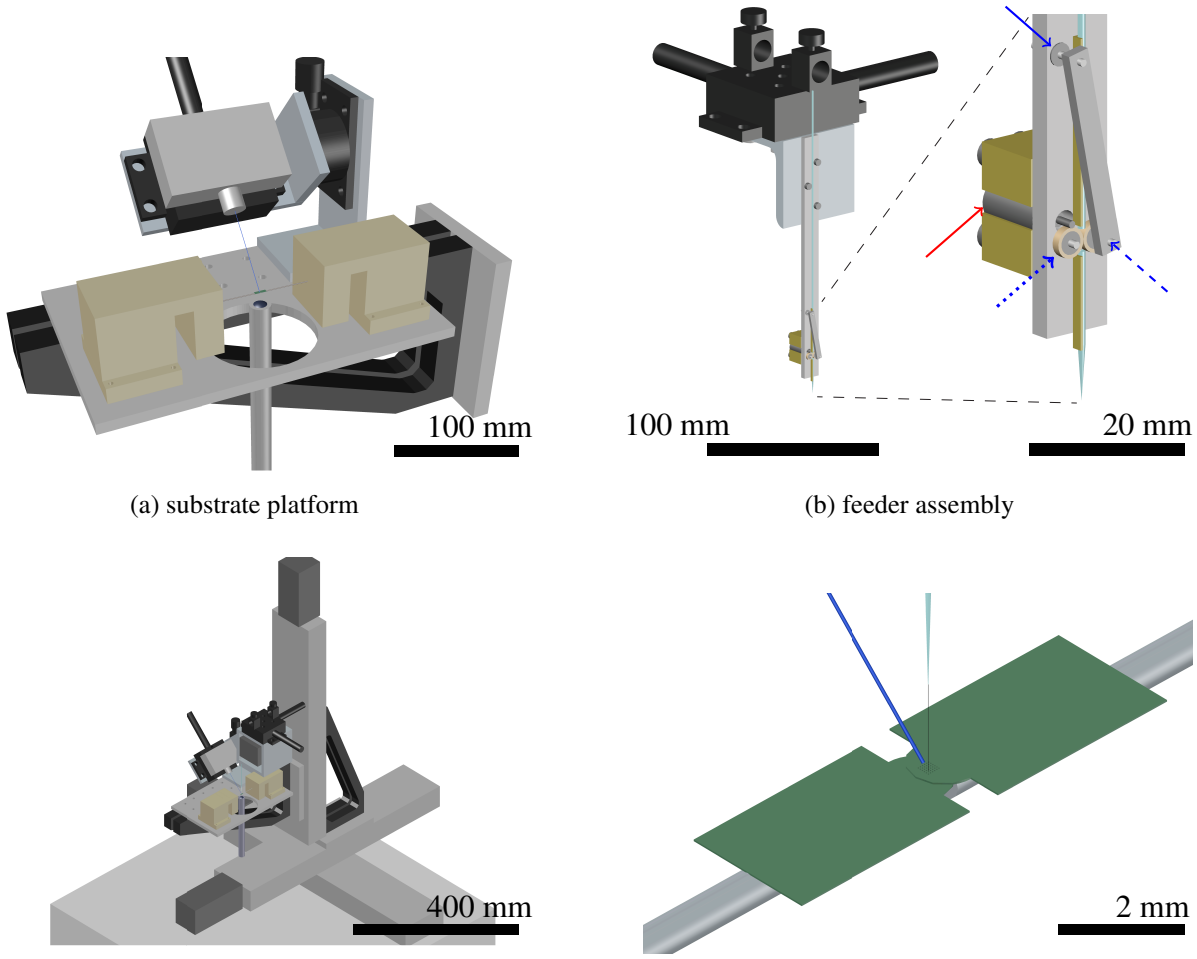

(a) substrate platform

(b) feeder assembly

(c) full system

(d) aligned substrates

Figure 3.2: CAD models of major system components. (a) The camera looks upward through a circular cutout in the substrate platform upon the substrates (green) suspended from three-axis manual micropositioners (beige) used for setup alignment. The blue (450 nm) laser is aimed with r and θ micropositioners (black) toward the substrates. The substrate platform is suspended by a mounting bracket affixed to the z-axis micropositioning stage (not shown). (b) The feeder assembly is comprised of a stepper motor (solid red arrow) that drives a fixed idler bearing (dotted arrow) against a second bearing on the swing arm (dashed arrow) to advance the carbon fiber. The swing arm is allowed to pivot freely about the point marked with the solid blue arrow, with gravity bringing it to rest against the fixed idler bearing. The fiber extends between two glass capillary segments above and below the rollers. The lower end of the glass capillary is pulled to a fine point. A two-axis manipulator sits atop the aluminum frame. (c) The full system is shown with the substrate platform and feeder assembly placed in relation to the three-axis positioning stages upon a 610 x 610 mm optical breadboard. (d) Close-up view of the substrates (green), feeder capillary tip (light blue), and laser (dark blue).

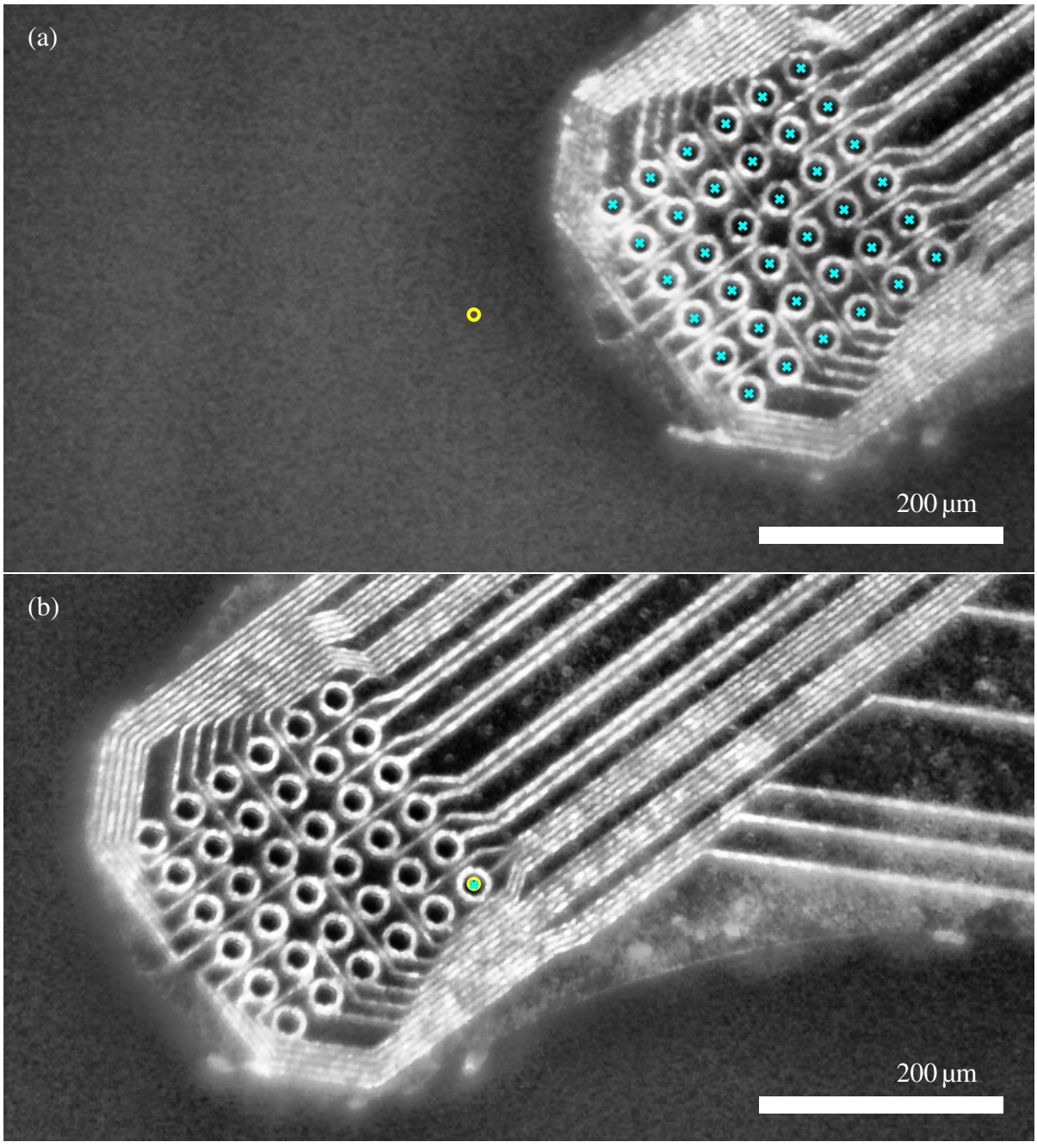

Figure 3.3: Array substrate as viewed through the camera. A yellow '○' indicates the center of each image. (a) The positions of 36 vias have been found and their centers marked with a cyan 'x'. (b) One of the vias has been centered in the image. The cyan 'x'on that via overlaps the yellow '○' representing the image center.

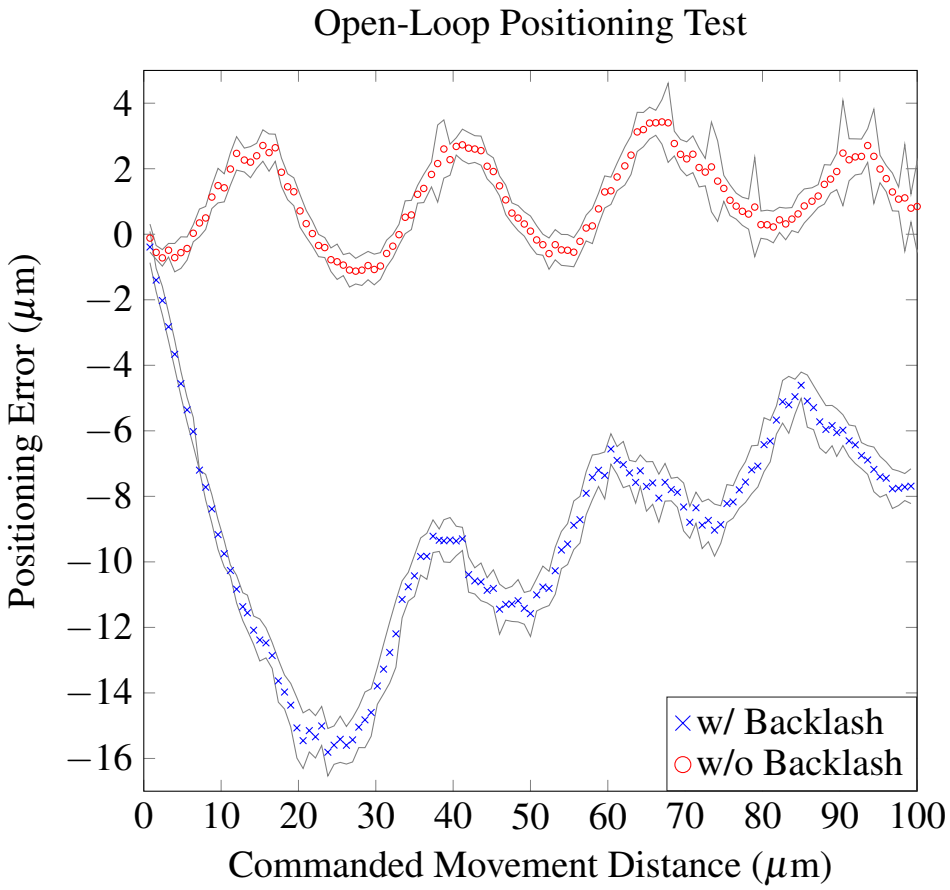

(a)

Figure 3.4: (Part 1/2) Plot of the open-loop positioning accuracy (a) with error bounds indicating $\pm\sigma$.

We compared open-loop positioning methods to both visual and encoder feedback positioning methods on the bases of mean positioning accuracy and time to complete each positioning task. Open-loop operation is the simplest and fastest positioning method, but is inaccurate due to the nonlinearity of the micropositioning stages. Closed-loop operations take more time due to their iterative approach to precise positioning, and visual feedback in particular requires considerable computational time for image processing. Time comparisons are inherently dependent upon the computational resources available and should be regarded qualitatively; for reference, all processing was done on a computer running 64-bit Windows 7 with an Intel Xeon E3-1240 3.4 GHz processor and 8 GB RAM.

The positional error, or difference between the attempted movement and the actual distance moved, is dominated in open-loop operation by backlash in the motors due to nonzero tolerances in the mechanical components and a second sinusoidal component (Fig. 3.4a). We can compensate for backlash with carefully designed movements, making precise movements only after a prior movement in that same direction, but the sinusoidal component is more difficult to eliminate. The period of the sinusoid corresponds to 1/200 motor revolutions, or one full step. Because in the general case the phase of this sinusoid is unknown for a given movement, this variation cannot be eliminated without painstakingly tracking one's position in the sinusoid between full-step stepper motor positions. Phase is preserved in our tests and the sinusoid visible in Fig. 3.4a because we followed each movement with an equal movement in the opposite direction. One would speculate that we can account for systematic error in the movement of the stages by applying the inverse function of the characterized nonlinearity, but results indicate that this yields no appreciable improvement, particularly in response to the sinusoidal trend. Variation among identical movements appears small compared to other sources of error.

Closed-loop feedback enables precise sub-micron positioning, but it requires iterative positioning attempts that may be computationally costly depending upon the feedback method. Any feedback method also requires additional hardware to provide the feedback signal and processing to interpret and act upon that feedback signal. Visual feedback (Fig. 3.4c) tends to reach to the desired position within 60 s. Encoder feedback (Fig. 3.4e) tends to reach the desired position much more quickly, averaging only 3.8 s. Time for each test is summarized in Table 3.3. Either method is capable of reliable sub-micron positioning, but encoder feedback is considerably faster given the computational requirements of the image processing required for vision feedback and is robust to image degradation as more fibers are inserted. Furthermore, just as one may purchase more expensive encoder read heads with finer resolution and better positional accuracy, one may likewise spend additional computational resources or time to improve visual precision through sub-pixel interpolation of the image. ± 1 pixel variation in the position of identified vias contributed to the increased number of convergence attempts required when positioning with vision feedback.

Costs

Cost is a third metric in addition to the aforementioned positioning accuracy and time, and is a consideration for anyone designing an automated system with similar positioning requirements. Used but fully functional steppers, stages, drives, and a controller mentioned above were purchased

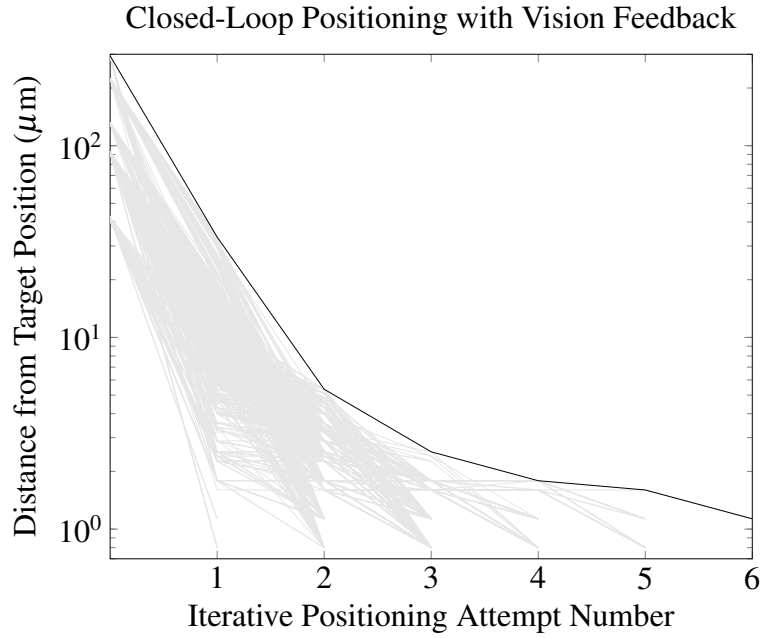

(b)

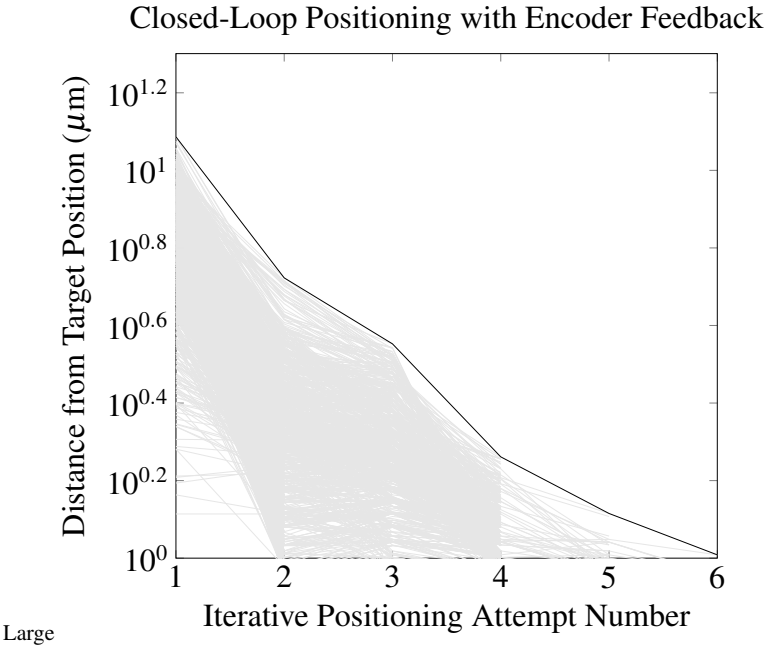

Large

(c)

Figure 3.4: (Part 2/2) Plots of closed-loop position convergence versus number of attempts using vision feedback (b) and encoder feedback (c) with an envelope (black) indicating the maximum number of iterations required to position within a given distance of the target position.

Table 3.1: Time to Complete Each Positioning Task

Test	Precision (μm)	Time per positioning step (s)
Open-loop	n/a	2.1 ± 0.02
Closed-loop, vision	0.8	59 ± 19
Closed-loop, vision	3.2	45 ± 16
Closed-loop, encoder	0.8	3.8 ± 1.2
Closed-loop, encoder	3.2	3.0 ± 0.7

Table 1. Time to complete each positioning task open-loop or under each feedback method. Two positioning accuracy thresholds are listed for each feedback method. 3.2 µm approximately corresponds to the best-case open-loop positioning accuracy for short movements.

Table 3.2: Cost of System Components

Method	open-loop	vision feedback	encoder feedback
Cost (USD)	$1400	$1468	$2369

Table 2. Monetary costs for system components necessary for three positioning methods.

used for US$1000 via eBay. Used encoder read heads were purchased similarly for $475, and an optical breadboard base for $400. New encoder scale tape was purchased from Renishaw for $426. The USB camera was purchased new for $68 from Amazon. We have omitted expenditures related to fiber feeding or laser operation because they do not relate to positioning, and it is assumed that computers are generally available. The cost of each positioning method is summarized in Table 3.2. The added cost of vision feedback is a negligible 5% increase, whereas the added cost of encoder feedback is a significant 69% increase and may not be tolerable in all applications.

Feeding Fibers through Holes: Success and Challenges

We have successfully fed fibers through the holes in the array, but the process still requires some manual intervention to align the fiber to the hole. The capillary tip, in practice, was over 20 µm in diameter, owing to the crude method by which the lower capillary tip is formed. The assertion that the inner diameter of the capillary is equal to the outer diameter of the fiber rests on two assumptions: first, that the tip is fractured precisely and squarely at the point at which the fiber can progress no further, and second, that the taper of the inner diameter of the capillary is gradual. The former is a matter of skill; however, it is notable that an error of 400 µm would result in a tip 14 µm larger than intended (assuming a linear taper). The latter is dependent upon the profile of the capillary pull, specifically on the combination of force, speed, and heat. These parameters are not carefully controlled when I pull the capillary by hand, but could easily be controlled using a commercial capillary puller. If the glass is too soft, for example, surface tension will close the narrowest portions of the capillary, and it becomes possible that the point at which the fiber ceases to progress further has a diameter significantly larger than the diameter of the fiber.

The fiber is never positioned in the center of the capillary. Rather, it rests against the capillary wall, particularly at the tip. The positional error of the fiber at the capillary tip is equal to the radius of the capillary tip aperture minus the radius of the fiber. As other sources of positioning error in the system can be reduced to less than one micron, this error quickly dominates. If there is no other error in the system, it becomes impossible to insert a fiber through a hole if the inner diameter of the capillary tip is larger than the diameter of the hole. As this was the case in the prototype, it was necessary to provide a manual offset to ensure the fiber itself was positioned over the hole. A fixed systematic offset cannot not be applied, because the fiber is free to move along the perimeter of the inner wall of the capillary.

Another challenge in feeding fibers throughout an array is that the fiber can electrostatically attract to the feeder assembly rollers, wrapping itself around the rollers. This is mitigated by minimizing the distance between the rollers and the lower capillary, and by minimizing the radius of the rollers themselves. I tested electrostatic ionizers, but found they didn't sufficiently reduce electrostatic attractions. Controlling humidity to between 40-60%, however, had a small impact. Greater humidity increased hygroscopic interactions and proved to be detrimental. Electrostatic interactions also occurred between the fiber and capillary, making it difficult for the rollers to advance the fiber through the lower capillary. Rather than advancing, the fiber would stick to the glass wall and buckle at the top of the lower capillary. While humidity plays a minor role in dissipating the electrostatic charge, minimizing the length of the lower capillary played the greatest role.

3.4 Conclusion

We have demonstrated an automated system for assembling fine-pitch microwire-style neural recording arrays. This approach is scalable to arrays of arbitrary numbers of electrodes, enabling unprecedented high-density neural recording arrays for chronic recording, and is generalizable to any micron-scale filament or microwire threading task.

The CAD and code for this system are available at *https://github.com/tlmassey/cf-robot*, and the components are affordable. We have also provided a comparison of several open- and closed-loop micropositioning methodologies, comparing their accuracy, repeatability, time, and cost for the benefit of others building low-cost sub-micron positioning systems.

For the automated assembly system to be production ready, two key improvements are necessary. First, the capillary pulling needs to be performed using a capillary pulling tool in order to achieve the proper capillary profile and tip diameter. Second, an automated mechanism to cut fibers after insertion must be developed. Plans for this latter were developed involving a servo actuating a fine pair of tissue scissors to replicate the manual process, but as the principle has been demonstrated, these plans have been left for future development. Once these improvements are in place, fully automating the threading of full arrays of carbon fibers is immediately feasible.

Threading carbon fibers through each hole is only one piece of the assembly process, albeit a significant one. The remainder of the assembly process is detailed in the following chapter, and applies whether or not one is threading arrays manually or automatically.

Chapter 4

Assembly procedure, characterization, and testing of the carbon fiber neural recording array

With the substrate fabricated and the challenge of scalable assembly addressed, the final major aspect of the device development process is the array assembly procedure. While previously mentioned only in passing beyond the threading of the carbon fibers, this assembly procedure is as involved as the substrate microfabrication process and contains its own set of critically important subtleties that are examined in detail in this chapter. Testing and characterization are also discussed, as these results feed back to inform the assembly process.

4.1 Array assembly procedure

Bond silicon substrate to flex PCB

The process of assembling the complete arrays from the microfabricated substrates begins by epoxying a device substrate to a polyimide flex printed circuit board (PCB) with low-viscosity epoxy (353ND, Epoxy Technology, Inc., Billerica, MA), curing at 150 °C for 1 h. The PCBs and substrates are cleaned in IPA and flowing DI water and dried with N_2 immediately before wire bonding the substrate to the PCB using a WestBond 747677E wedge bonder outfitted with 25 µm aluminum bond wire and corresponding wedge (WestBond, Anaheim, CA). The wire bonds are protected with the same 353ND epoxy, which is cured as above. A strip of aluminum is taped against the connector solder pads on the back end of the device to discharge all electrostatic charge from the substrate holes and carbon fibers during assembly.

Thread and bond carbon fibers to silicon substrate

The device and an alignment substrate (see section B.1 for microfabrication details) are mounted on micropositioners, with the silicon parallel to the work surface and the holes of the substrate overhanging the leading edge of each micropositioner. A droplet of water-based silver nanoparticle ink (Novacentrix HPS-030LV, Austin, TX) is applied to the head of the device substrate, covering all thirty-six holes. The ink-covered device can optionally be placed under vacuum for 2 min to aid filling the vias with silver ink; by removing air, the energy landscape more strongly favors the ink wetting the substrate and filling the via. A doctor blade (durometer 90A polyurethane rubber, McMaster-Carr, Elmhurst, IL) is then passed over the surface to force the silver ink into the holes and remove excess from the surface. A second layer of silver epoxy (Atom Adhesives AA-DUCT 24, Fort Lauderdale, FL) is applied to the holes and cleared with a doctor blade in the same way. Excess silver ink is cleaned from the back with the doctor blade, and a small piece of Kapton tape is applied behind the holes as a temporary backstop for the ink, epoxy, and carbon fibers.

The holes of the alignment substrate are precisely aligned above the device substrate using the micropositioners, leaving minimal or no gap between the two substrates, and the 5.2 µm carbon fibers (HexTow IM7, Hexcel, Stamford, CT) are serially threaded through each hole using a third micropositioner. The fibers are temporarily adhered to the probe tip of the third micropositioner by a thin film of cured silicone. Each fiber is lowered into its target hole, and the adhesion between the ink/epoxy and the fiber overcomes the adhesion of the fiber to the silicone, allowing the fiber to remain in the hole when the silicone-coated probe tip is removed. Once all thirty-two fibers are threaded this way (the back-end connector has only thirty-two channels, so four of the thirty-six holes need not be threaded), the alignment device is raised using the micropositioner nearly to the tips of the carbon fibers, ensuring that the fibers are parallel and vertical. The ink and the epoxy are cured in this position in a box oven at 230 °C for 3 h. Following cure, the alignment substrate, backside Kapton tape, and aluminum strip are all removed.

Solder external connections and insulate assembled array

An Omnetics nanostrip connector is soldered to the PCB, and the base is encapsulated in 353ND epoxy as before. An uninsulated 76 µm silver wire is soldered to a reference terminal, and the wire is tacked to the polyimide using UV-curable epoxy (Loctite 3526, Henkel, Düsseldorf, Germany) to provide strain relief. A 6 mm cube of polystyrene is cut and epoxied on the underside of the PCB beneath the device substrate. The tail is then folded back and epoxied to the opposite side of the polystyrene block, and the connector and silver ground wire are sealed and masked with Kapton tape. The entire device is electrically insulated in a conformal 0.8 µm film of parylene-C (Labcoter 2, Specialty Coating Systems, Indianapolis, IN), deposited per manufacturer parameters. Deposition is performed with the device sitting on a 100 mm silicon wafer for thickness characterization via ellipsometry, and the deposited film is verified free of pinhole defects by placing the wafer in KOH and monitoring for the evolution of bubbles indicative of KOH reaching the silicon surface.

Expose and electroplate recording sites

To expose the recording sites at the tips of the carbon fibers, the entire device is embedded in a block of Tissue-Tek 4583 embedding compound for cryotoming (Sakura Finetek USA, Torrance, CA) and frozen to $-80\,^{\circ}\mathrm{C}$. The embedded device is mounted into the cryotome held at $-55\,^{\circ}\mathrm{C}$ and progressively shaved in 10 µm sections with a TiN-coated blade (C.L. Sturkey, Inc., Lebanon, PA) until the tips of all fibers are exposed. The embedding compound is thawed and thoroughly rinsed in deionized water. A summary of this complete assembly procedure is provided in figure 4.1. A model, photograph, and SEM of an assembled device are shown in Figure 4.2.

With the tips of the fibers in 1x phosphate buffered saline, we apply $-18\,\mathrm{V}$ versus a platinum wire counterelectrode to reduce the impedance through the silver ink. Finally, the recording sites are electroplated with PEDOT:PSS at 7 nA for 60 s using a freshly prepared solution of 0.01 M 3,4-Ethylenedioxythiophene (EDOT) and 0.01 M Poly(sodium 4-styrenesulfonate) (PSS) with molecular weight of approximately 70 kDa (Sigma-Aldrich, St. Louis, MO).

4.2 Device characterization

Electrical characterization methods

All electrical impedance measurements are performed with the recording sites and silver wire reference electrode (if applicable) submerged in 1x phosphate-buffered saline (PBS). Electrochemical impedance spectroscopy (EIS) is performed over a range of 115 frequencies ranging from 5 Hz to 5 kHz using a nanoZ (White Matter LLC, Seattle, WA) and averaged over 40 cycles. Impedance between every pair of electrodes is measured using a Keysight E4980L precision LCR meter (Santa Rosa, CA) in conjunction with a custom software-controlled multiplexer from [136], taking for each pair the mean of five samples. These pairwise measurements were conducted first in air (open-circuit) before PBS for purposes of identifying potential shorts and quantifying crosstalk between channels. Fibers were submerged in liquefied Field's metal (51% In, 32.5% Bi, 16.5% Sn; melting point $62\,^{\circ}\mathrm{C}$) rather than PBS for short-circuit testing.

Noise was measured on two recording systems. The first set of noise measurements was performed inside a Faraday cage to minimize electromagnetic interference (EMI) using a PCIE-16AI64SSC-64-B General Standards Corporation (Huntsville, AL) data aquisition card sampling at 20 kHz and FA64I Multi-Channel Systems (Reutlingen, Germany) amplifier with a fifth-order bandpass from 0.1-6000 Hz. The second system was the Plexon Multichannel Acquisition Processor (MAP) recording system sampling at 40 kHz (spike band) and 1 kHz (field potential band) with J2 headstage and PBX-517 preamplifier (Dallas, Tx) used for *in vivo* experiments. While lacking a Faraday cage and subject to increased EMI, this latter set of measurements better imitates the noise conditions during *in vivo* testing. Signals were allowed a settling time of 7τ before data were recorded, and high-pass filtering data in the first set at 300 Hz (7th-order Type II Chebychev, 80 dB rejection) removed any residual low-frequency drift as well as 60 Hz interference and its significant harmonics with only a 5% reduction in measurement bandwidth. Noise amplitude is calculated as the root mean square of the signal. Data from the second set were filtered only by

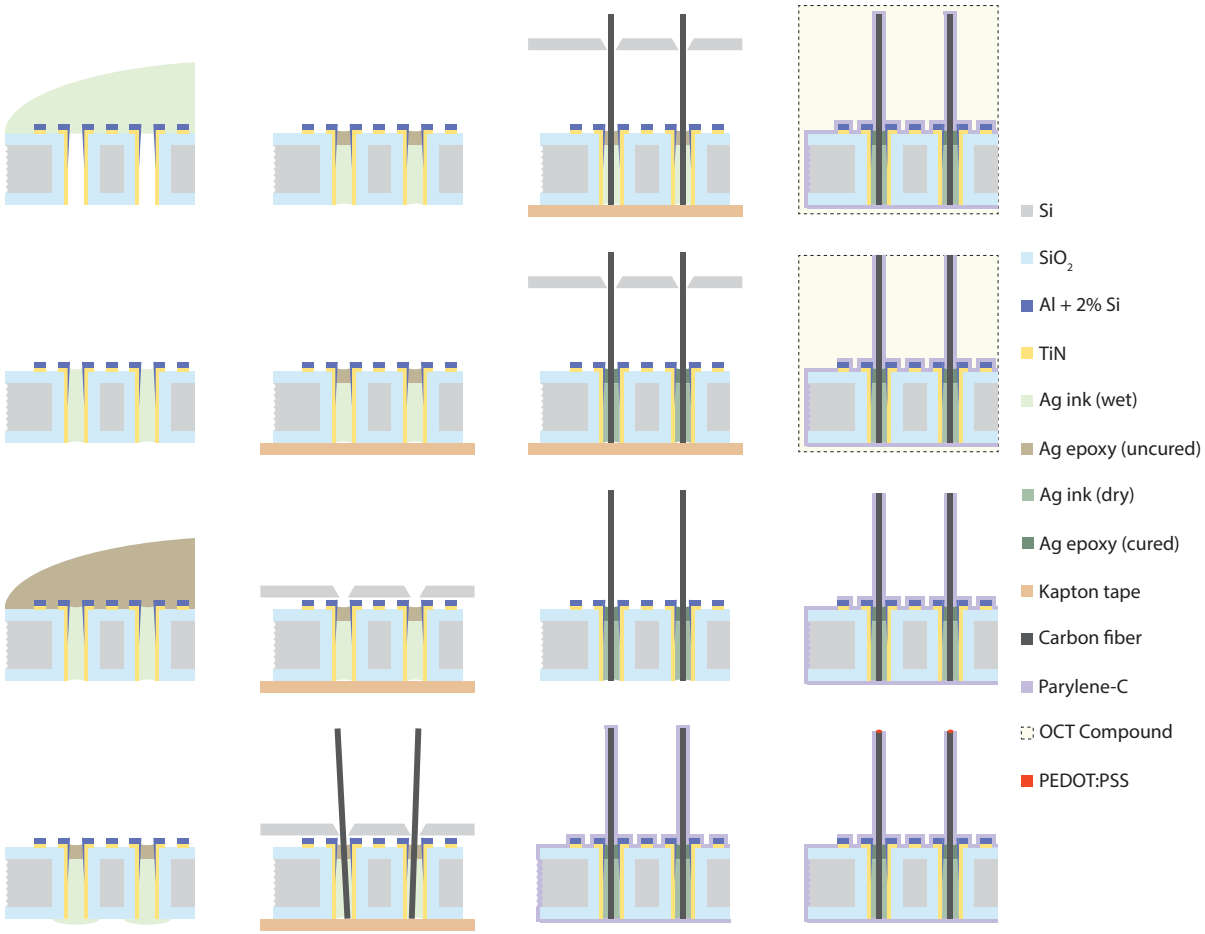

(a)

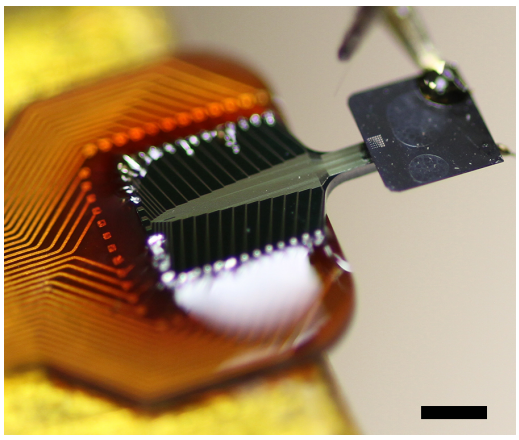

(b)

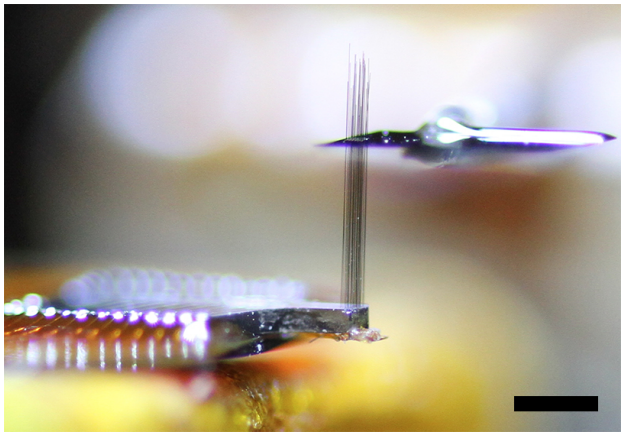

(c)

Figure 4.1: (a) Cross-sectional diagrams of the carbon fiber array assembly process. (b) Photograph of the threading process, with alignment substrate aligned to device substrate and a third probe tip guiding a fiber to the first hole. (c) Photograph of a threaded device during assembly. The alignment substrate has been separated from the device substrate to parallelize the 2.5 mm fibers. Scale bars: 1 mm.

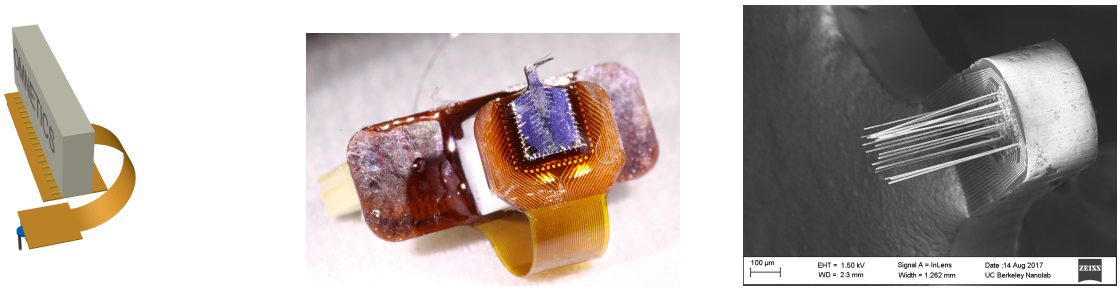

(a) (b) (c)

Figure 4.2: (a) Model of a complete assembled device showing the substrate (blue) with fibers (black) on the polyimide flex PCB (orange) with Omnetics header (white). (b) Photograph of an assembled recording array. (c) SEM of the head of a recording array with the carbon fibers clearly visible. Fibers in (b),(c) shortened for ease of imaging.

the in-built preamplifier filters, 500-8800 Hz (spike band) and 3-200 Hz (field potential band). The signal to noise ratio is calculated as the square of the ratio of the root mean square (RMS) voltage of the mean spike waveform on a given channel to the RMS noise voltage.

Electrical characterization results

Impedance measurements for an unexceptional device after exposing recording sites, after applying a breakdown voltage to the silver ink, and after electroplating the recording sites with PEDOT:PSS are summarized in Figure 4.3. Briefly, impedance consistently decreased by 2-10x upon applying a voltage across the electrode array, with those sites having higher initial impedance decreasing by a larger factor, and phase trending nearer to zero (more resistive). Figure 4.4 demonstrates this effect more prominently than in the typical case. Impedance decreased further upon electroplating, typically approximately 1.5-5x, with negligible change in phase.

The assembly process results in a high yield, with greater than 90% of recording sites showing continuity ($|Z| < 10\,\mathrm{M\Omega}$) and greater than 80% showing impedances below 2 MΩ at 1 kHz across all devices. Yield during assembly is limited primarily by continuity through the silver ink, as is discussed in Sections 4.3 and 4.3.

To confirm that the silver ink dominates the electrode impedance before applying the breakdown voltage, impedance was measured between every pair of electrodes with recording sites in liquefied Field's metal both before and after applying the breakdown potential. Similar impedance values measured in PBS and Field's metal (Figure 4.5) suggest that the impedance before application of the breakdown voltage is dominated by the silver ink rather than by interface between the electrode and the surrounding medium. After applying the 18 V potential, 100 Hz impedance was observed to decrease by 2x in Field's metal compared to PBS.

Thermal noise, which is a function of the electrode impedance and has a direct impact on the signal-to-noise ratio (SNR) of the recordings, was measured to be on average 8.4 µV over the 0.3-6 kHz band. The amplifier nominally contributes 1.3 µV ($17.5\,\mathrm{nV\,Hz^{-0.5}}$) of noise uncorrelated to

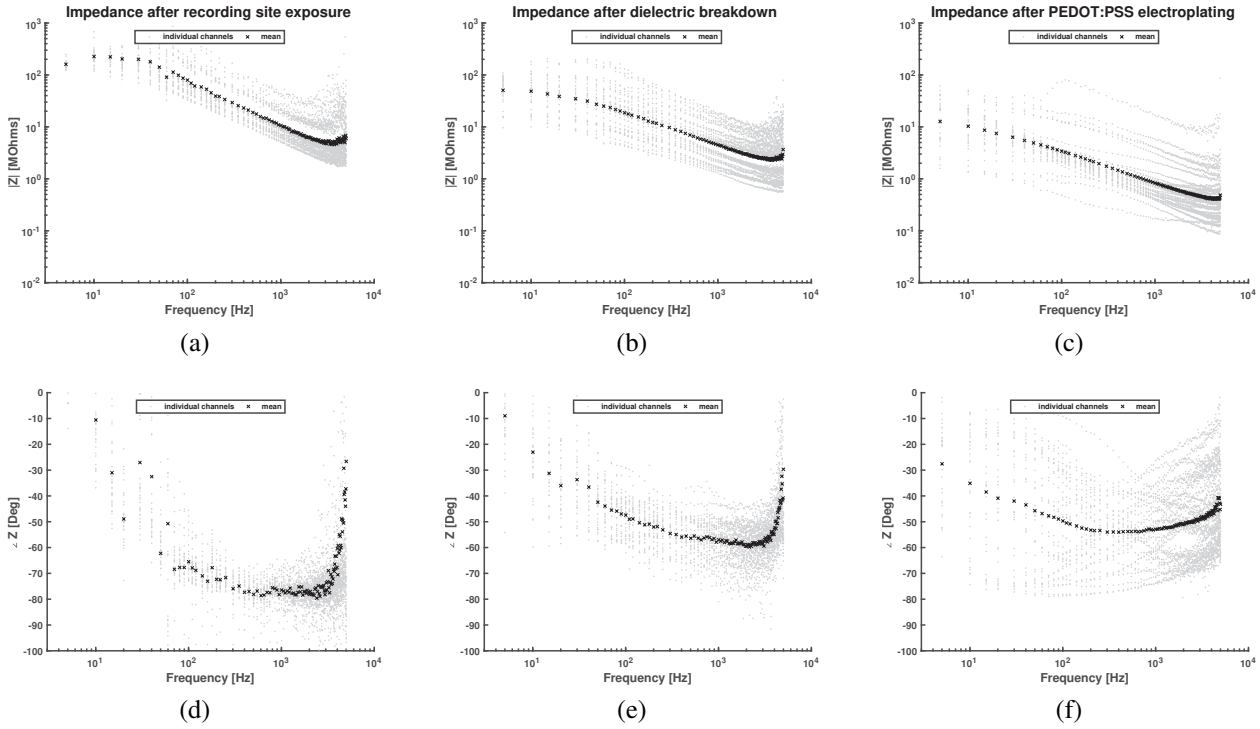

Figure 4.3: Impedance spectroscopy for electrodes on a typical device (a,d) immediately after recording sites are exposed, (b,e) after 18 V is applied to break down residual dielectric in the silver ink, and (c,f) after electroplating the recording sites with PEDOT:PSS. The geometric mean and geometric standard deviation of the magnitude of impedances at 1 kHz are in (a) $\mu_g \times \sigma_g^{\pm 1} = 10.62\,\mathrm{M\Omega} \times 1.81^{\pm 1}$, in (b) $\mu_g \times \sigma_g^{\pm 1} = 4.481\,\mathrm{M\Omega} \times 2.24^{\pm 1}$, and in (c) $\mu_g \times \sigma_g^{\pm 1} = 0.828\,\mathrm{M\Omega} \times 2.63^{\pm 1}$.

the electrode noise, and thus 8.3 µV (110 $\mathrm{nV\,Hz^{-0.5}}$) is attributable to the electrodes themselves. Spectral analysis confirmed that the measured noise was white; however, measurements taken on the Plexon recording system outside the Faraday cage showed greater electromagnetic interference. Spike-band noise density on the Plexon system is 450 $\mathrm{nV\,Hz^{-0.5}}$, approximately four times larger (41 µV over the 0.5-8.8 kHz band). Noise in the Plexon system's 3-200 Hz band was 15 µV (1100 $\mathrm{nV\,Hz^{-0.5}}$). This increase in noise density at low frequencies is consistent with 60 Hz interference and its harmonics visible in spectral analysis (not shown).

Crosstalk is likewise an important consideration in the evaluation of a neural recording array, and can be estimated by the ratio of the impedance between any pair of electrodes while out of solution (open circuit) and in PBS. Figure 4.6 shows the mean impedance measured in air and in PBS, where the mean was taken over all 496 pairwise combinations of the 32 electrodes. A control experiment is also shown where no device was connected to the measurement apparatus, confirming that the measured impedance of the device in air is very similar both in magnitude and purely capacitive phase to the control, and that the extent of the crosstalk is below what can be

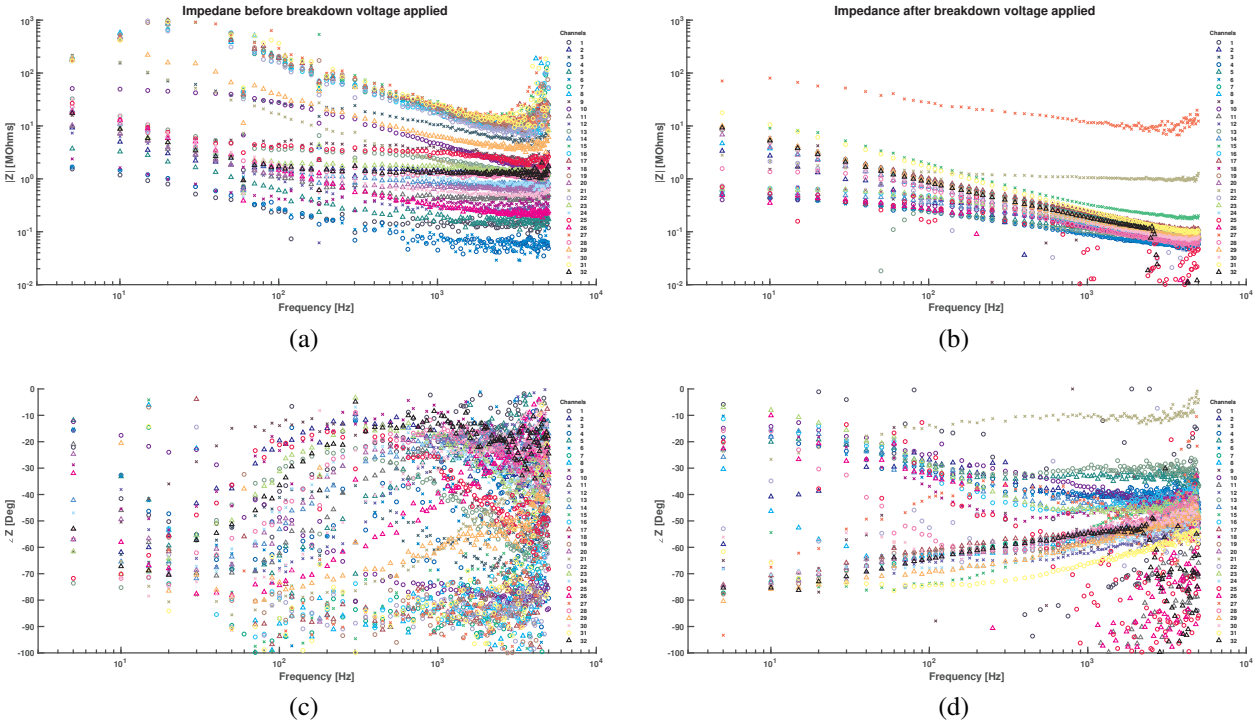

Figure 4.4: Impedance spectroscopy highlighting the decrease in impedance due to applying a breakdown voltage across the silver ink. (a,c) Plot of electrode impedance immediately after the recording sites are exposed, and (b,d) after 18V is applied to break down residual dielectric. Each color corresponds to one channel, illustrating that the low-impedance sites decreased in magnitude by about 3x after breakdown, and the high-impedance sites decreased by about 30x.

measured with the current setup. The finite impedance is attributable to the non-zero CMOS off current in the multiplexer [137].

Insertion testing in agar: Array penetration is strongly dependent upon fiber length but not upon angle

The effect of fiber length and angle on the success of penetration was tested by inserting assembled arrays into 0.6 w/w% agar gel to mimic many mechanical properties of the brain [138–140]. Devices were rotated relative to the agar in 0.2° increments to a maximum of 4.5° using a rotational micropositioner, and were subsequently advanced into the agar such that the direction of motion was off-axis from the fiber by the specified angle. 1.4, 1.9, 2.3, 2.8, and 3.5 mm lengths were tested. The agar was shifted slightly between each test so as not to penetrate the same point repeatedly.

Testing the effect of fiber length and angle revealed that the angle of the fibers plays essentially no role with regards to the success of insertion within the range of angles tested, up to 4.5 degrees off-axis. This is presumed to be because local dimpling at the tip of each fiber effectively presents

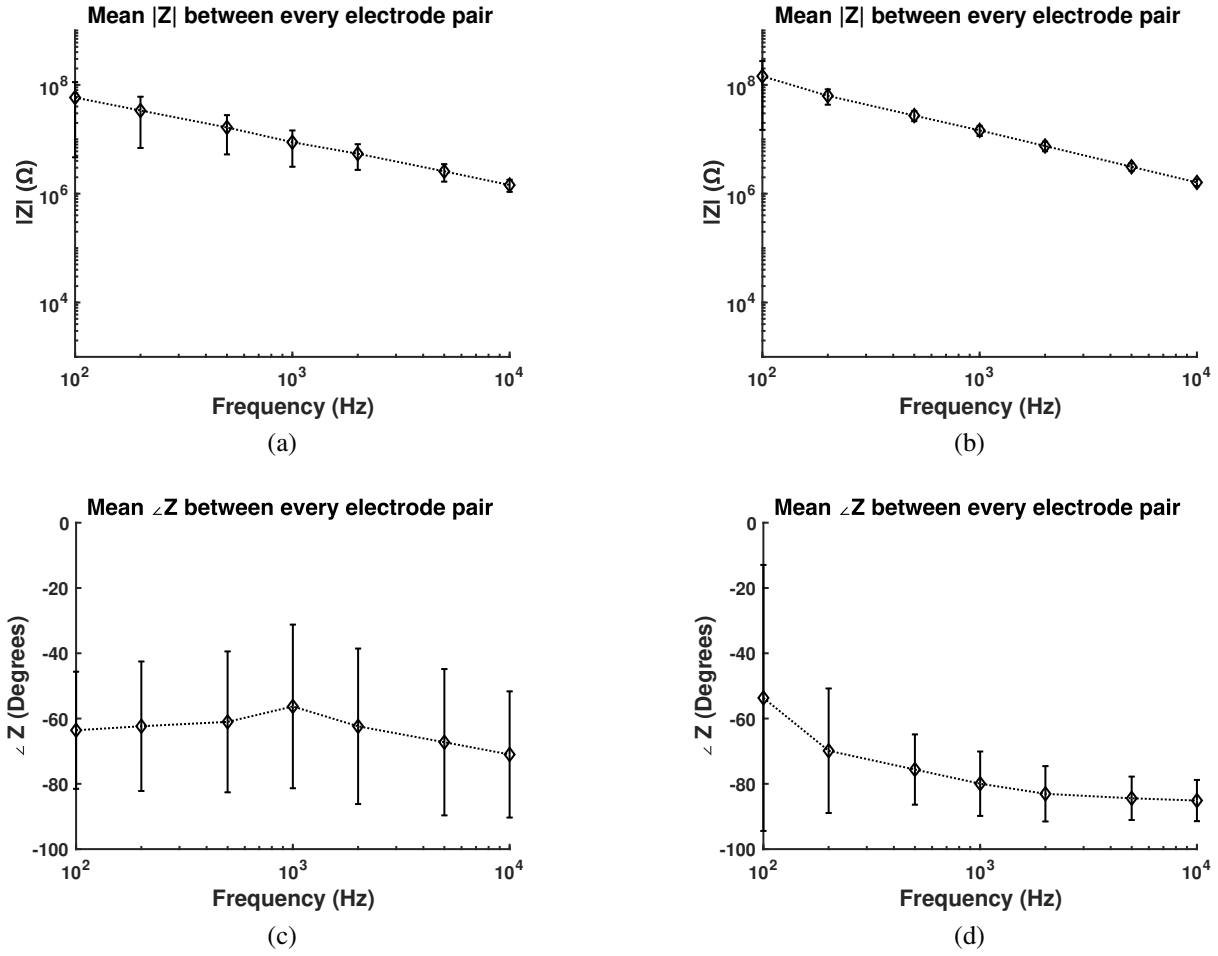

Figure 4.5: Average impedance ($\mu \pm \sigma$) between every pair of electrodes (a,c) in PBS and (b,d) in Field's metal before applying breakdown voltage. The similar impedance values between the PBS and Field's metal cases suggest that the impedance is dominated by the silver ink.

an orthogonal surface. This result suggests that while highly parallel fibers may have benefit for the distribution of recording sites, parallelism is not strictly required for successful insertion.

The length of the fiber, however, plays a strong role as expected from column buckling theory and as shown in [108]. Fibers shorter than 3.5 mm penetrated the 0.6% agar gel successfully on every attempt, but 3.5 mm fibers penetrated only with difficulty. Typically either multiple attempts were required, or some small lateral movement of the array was necessary while the fiber tips were in contact with the agar in order to coax the fibers to penetrate the surface. This set a practical upper bound of 2.5-3 mm for devices to be implanted *in vivo*, recognizing that agar is not a perfect model for cortical tissue.

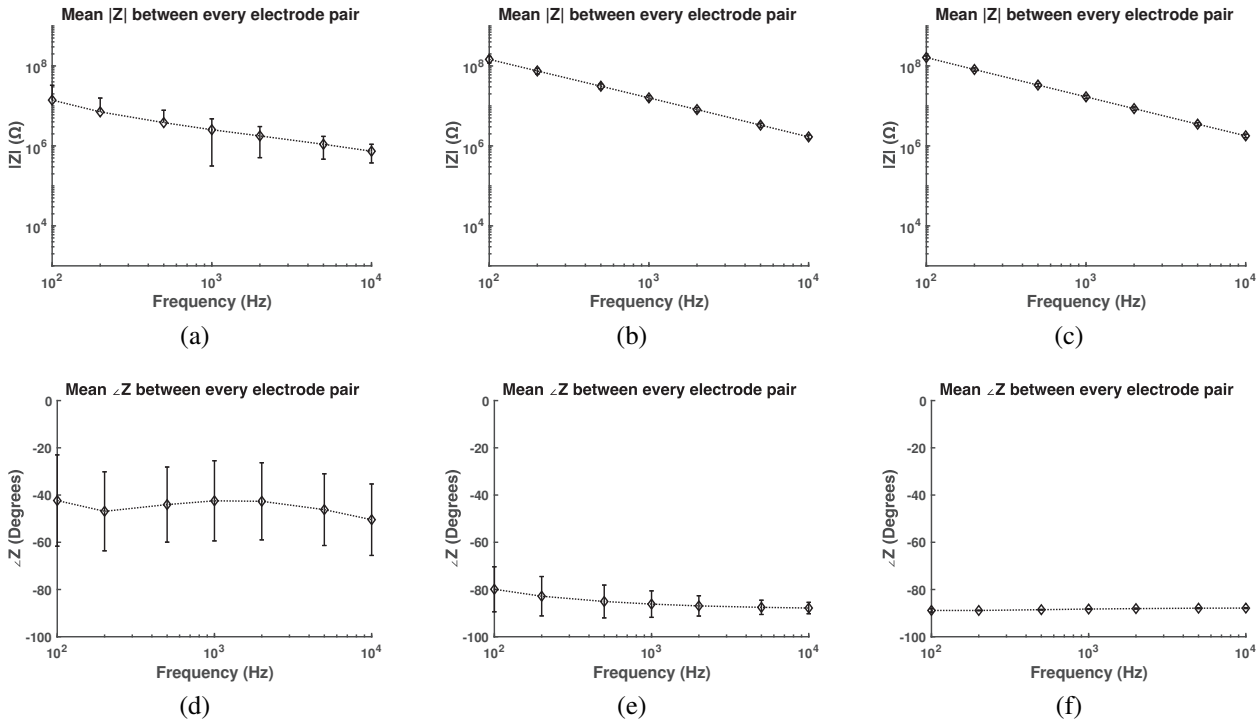

Figure 4.6: Average impedance ($\mu \pm \sigma$) between every pair of electrodes (a,d) in PBS, (b,e) in air, and (c,f) with no device connected as a control. The similar impedance values between the air and control cases suggest that the measured crosstalk is through the multiplexer rather than through the device itself, and thus that the crosstalk through the device is quite low.

4.3 Special considerations in the array assembly process

The properties of the isotropically conductive adhesive are critical for conductivity at small scales

Several aspects of the assembly procedure warrant note for their subtle importance. Primary among these is the choice of isotropically conductive adhesive (ICA) for use in electrically and mechanically bonding the fibers and the vias. ICAs, and silver-filled epoxies in particular, are commonly used in microassembly of carbon fiber-based recording electrodes [55, 80, 105, 108], but our early experiments yielded inconsistent connectivity between the fiber and the conductive inner sidewall of the substrate.

Most ICAs operate by the formation of percolation networks, with the contact among many randomly arranged particles in the bulk material forming a network of conductive paths between the two relevant surfaces to be electrically (or thermally) connected. The ICA's conductive particle (i.e. silver) content required to form a conductive network is function primarily of the average size, distribution, and shape of the particles in the ICA [141]. Size plays the most significant role, with a greater volumetric particle content, or fill, relative to polymeric binder required as the average

particle size decreases.

In a constrained volume such as the vias on the array substrate, the largest particles in the distribution may be physically excluded. This has the effect both of reducing the average particle size and reducing the fill of the ICA. This latter effect can be significant, as large particles accounting for a negligible fraction of the total particle count can account for a substantial fraction of the total fill due to cubic scaling. One percent of particles by count in off-the-shelf silver epoxy formulations, H20E and H20S (Epoxy Technology, Billerica, MA), may be as large as 45 and 20 µm, respectively, and the exclusion of these large particles is sufficient to decrease the epoxy fill below the conduction threshold on the majority of electrodes.

While it would initially seem straightforward to seek a silver epoxy formulation with a smaller average particle size or tighter distribution (AA-DUCT 24 was developed in part for this work and is quoted as having particles no larger than 2 µm), this correspondingly increases the required fill fraction, as noted above. An increase in the silver fill comes at the expense of the polymeric binder, which contracts as it cross-links during the cure to stress the silver particles and force them into intimate contact. With insufficient binder, this critical step in the process doesn't occur and no conductive path will be formed, despite the high silver fill. Thus, a minimum amount of binder is also required to form a conductive network. Given that smaller particles require an increase in silver fill without decreasing the binder content, it becomes apparent there is a minimum particle size below which silver epoxies cannot form a percolation network, and indeed H20S (1-2 µm mean particle size) is near this lower limit.

Silver ink operates by a similar but subtly different mechanism from silver epoxies, in that there is a third key component in addition to the silver and the polymeric binder. Inks also contain a solvent, which vaporizes during cure to aid in effecting a volume loss to draw the particles into contact. As a result, less polymeric binder is required, and the effective silver fill after solvent evaporation can be higher than in an epoxy. Correspondingly, slightly smaller silver particles (Novacentrix HPS-030LV: 400-800 nm) can form a conductive percolation network.

The presence of a solvent comes at a cost, however; it begins to evaporate at room temperature, after 20-30 minutes a skin impenetrable by the carbon fibers forms on the surface. To prevent this skin formation and extend the working time of the silver ink, solvent evaporation must be inhibited with a cap layer that won't interfere with the ink's chemistry. After exploring unsuccessful options including adding low vapor pressure solvents atop the ink, the silver epoxy we had explored initially proved to be the best candidate. Using an epoxy cap layer additionally served to mechanically reinforce the joint, as silver epoxy is significantly stronger than silver ink.

The silver ink impedance can be further reduced

Despite the aforementioned ICA optimizations, the impedance contribution of the silver ink still dominated the overall impedance of most channels. To confirm, we tested the impedance of an electrode array in saline and compared against similar impedance measurements taken with the recording sites submerged in liquefied Field's metal (51% In, 32.5% Bi, 16.5% Sn; melting point 62 °C), and found that the impedances were similar [does this need a figure?]. This suggested that there was still a thin residual film of polymeric binder between silver particles in the ICA.

Given the sub-micron size scale of silver particles, we hypothesized that the residual dielectric must be less than 100 nm in thickness, and breakdown of that dielectric would result in pyrolysis of the polymer and the formation of a graphitic short between silver particles. Typical values for polymer breakdown voltages range from 20-200 MV/m, so the expected breakdown potential was expected to be less than 20 V. Indeed this is what we found, with an application of -18 V DC proving sufficient to reliably reduce the impedance by 0.5-1.5 orders of magnitude. The formerly highest impedance recording sites were reduced most significantly, with the overall effect that the variability in electrode impedance within each device was substantially reduced following this dielectric breakdown treatment. Below -18 V, the submerged portion of the carbon fibers could be destructively oxidized due to the energy provided by the large potential. With the electrodes reversed, such that electrolysis produced oxygen at the carbon fibers rather than hydrogen, the voltage at which oxidation occurred was significantly lower.

Mitigating electrostatic interactions during assembly is necessary for fibers to remain parallel

The fibers naturally acquire electrostatic charge during assembly, causing the fibers to repel each other and splay outward. If the silver ink and epoxy are cured while the fibers are electrostaticlly splayed, they will maintain some of that divergence even if later discharged. Steps can be taken to minimize electrostatic charging of the fibers during assembly, including increasing the ambient humidity and using a neutralizing ion generator, and indeed this has merit in mitigating complicating interactions among fibers or between fibers and other objects during assembly, but it is impossible to prevent the accumulation of some charge. Thus, it is critical that the fibers be discharged until after the ICAs are cured. This is most conveniently achieved with the application of the aforementioned aluminum strip short circuiting all channels to ground during assembly.

Embedding temperature, compound, and blade choice are critical to cleanly exposing recording sites

In exposing the recording sites, several parameters were experimentally varied to qualitatively achieve the cleanest possible cut. After each trial, the fibers were examined under an optical microscope and/or SEM to assess the length of fiber removed, the number of fibers cut, the occurrence of incompletely severed parylene insulation, and stretching of the parylene insulation beyond or over the tip of the fiber. The carbon fiber itself was trivial to cut (or break) through; parylene is more challenging. Temperature, embedding compound, and cryostat blade choice each play a significant role in the quality of the cut through the parylene-coated carbon fiber.

Given the above, the goal is to cut through the majority of parylene-coated fibers on every pass with minimal inelastic deformation of the parylene. Thus, the ideal embedding compound has similar mechanical properties to the parylene insulation. Because the hardness and compliance of embedding compounds is a strong function of temperature, and embedding compounds are generally much softer and more compliant than parylene, lower temperatures are favorable. We

tested the standard Tissue-Tek OCT (optimal cutting temperature) compound at −26 °C, −38 °C, and −55 °C, and found that the cuts were consistently of the highest quality at −55 °C. We observed greater elongation of the parylene at higher temperatures, and at higher temperatures each fiber was cut only every second or third 10 µm pass of the cryostat. Liquid nitrogen was tested briefly to freeze the OCT compound even further, but the thermal shock cracked one of the silicon substrates and further liquid nitrogen testing was abandoned.

Based on the observation that temperature and thus hardness was critical, we also tried an embedding compound designed for low-temperature use and water ice. The low-temperature embedding compound was actually softer than the standard embedding compound at a given temperature, having been designed for sectioning lipid-rich tissue at −40 °C. The water ice, which was considerably harder than both polyvinyl alcohol and polyethylene glycol-based embedding compounds, was unacceptably brittle and resulted in cuts of widely variable thicknesses as the blade struggled to engage such a thin layer of ice.

Lastly, the exact blade type matters. Infinity, Gold, Extremus, and Diamond blades were purchased from C.L. Sturkey, Inc., Lebanon, PA. Infinity blades had no advertised ceramic coating, but were ground with three bevels; gold blades were coated in a titanium nitride thin film; diamond blades were coated in an amorphous diamond thin film; and extremus blades were coated in an unknown film, advertised as being well suited to a wide variety of cutting conditions. Upon examining fibers cut by each blade under otherwise ideal conditions under an SEM, the "Gold" blades consistently produced the cleanest cuts, closely followed by Infinity and Extremus with more frequent elongation of the parylene. The Diamond blades performed poorly for this application, resulting in many broken fibers still attached by incompletely severed parylene.

4.4 Action potentials can be recorded in the CNS on multiple recording sites

Following the assembly and characterization, we tested the devices *in vivo* to demonstrate that they are capable of robustly recording neural activity. Animal experiments were conducted in accordance with the University of California Animal Care and Use Committee regulations and National Institutes of Health guidelines. One adult male Long-Evans rat (625 g) was unilaterally acutely implanted in M1 with the carbon fiber neural recording array. The rat was anesthetized with isoflurane gas throughout the procedure and was injected with 0.4 mg dexamethasone prior to the procedure to reduce swelling. Body temperature was monitored and maintained at 36 °C. A craniotomy was performed above the primary motor cortex with the rat fixed in a stereotactic mount, the dura and pia were resected. The neural recording array was lowered using a manual micropositioner until the recording sites penetrated 0.5-0.9 mm into the cortex. Spontaneous activity was recorded using a Plexon Multichannel Acquisition Processor (MAP) recording system with a J2 headstage and PBX-517 preamplifier (Plexon Inc., Dallas, TX), with spike-band (0.5-8.8 kHz) data sampled at 40 kHz and LFP-band (3-200 Hz) data sampled at 1 kHz. Activity was sorted online and sorting templates were further refined using offline sorting software (OfflineSorter, Plexon Inc., Dallas

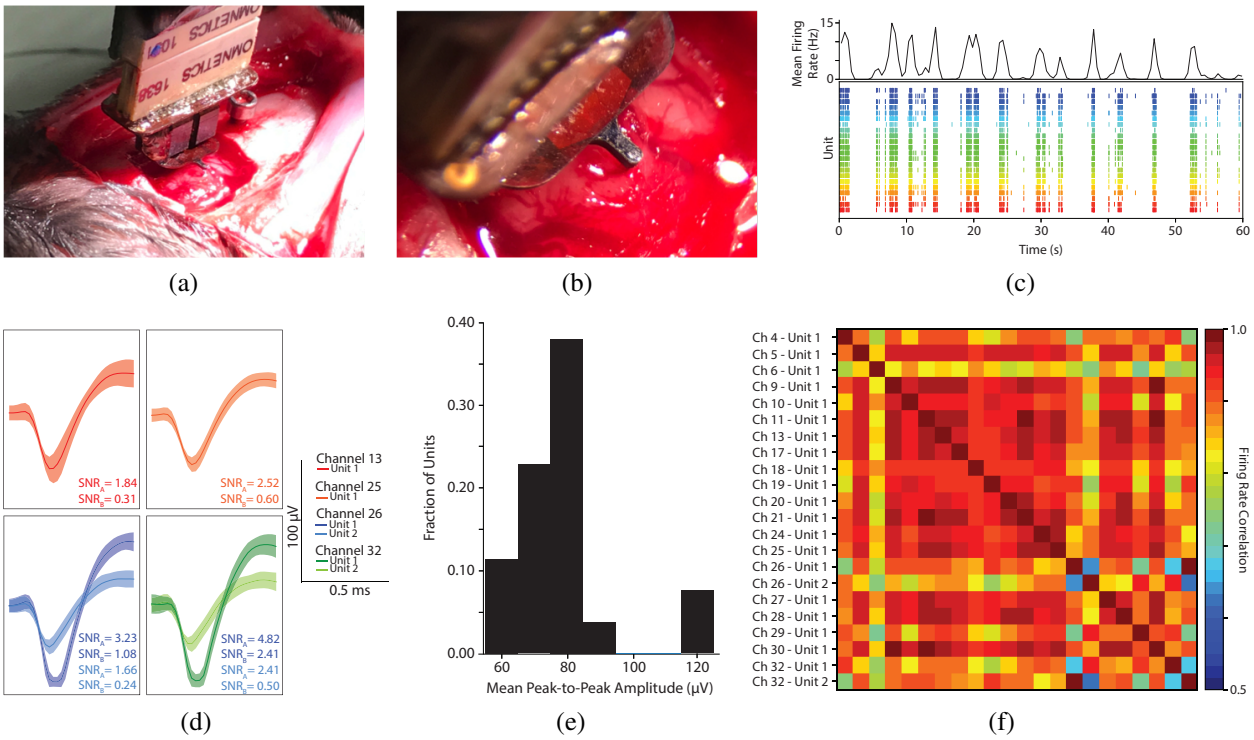

Figure 4.7: (a,b) Photographs of of a carbon fiber neural recording array implanted in M1. An enlarged craniotomy is shown for visibility, but in practice the craniotomy was approximately 1 mm in diameter. (c) Unit firing activity over time. The lower figure depicts a raster plot of the recorded units for 60 seconds, where each color represents spiking data recorded from a different unit. 22 units were recorded in total over 20 of the 32 channels. The upper figure displays the instantaneous firing rate averaged across all of the recorded units. (d) Representative unit waveforms recorded from M1. Mean unit waveforms from four channels are shown, with the shaded regions indicating the standard deviation of the corresponding unit activity. Signal-to-noise ratio (SNR) values are given for each unit according to Methods A and B described in Section 4.4. (e) Distribution of peak-to-peak unit amplitudes. The amplitudes are grouped to into 10 µV bins to determine the distribution of waveform amplitudes. (f) Correlation of spiking activity across channels. Unit activity is binned into 500 ms segments over the duration of the recording and using to compute firing rates over time per unit. Pearson correlation across all units using these firing rates is shown with the color indicating the strength of the correlation.

TX). Data were read using the Neo package for Python (NeuralEnsemble Initiative) and analyzed post-hoc using custom Python software.

The 32-channel array was used to measure the spontaneous neural activity in M1, recording field potential on all channels and identifying well-isolated units on 20 channels. Figure 4.7 shows photos of the implanted array and summarizes key data validating the carbon fiber array for single-unit recording. The raster plot indicating unit timing and firing rate suggests that the majority of

unit activity is likely produced by one neuron, with a limited number of other neurons producing the remainder of detected spike events. This is further supported by the high correlation observed among units and spatial proximity of the recording sites. Representative single-unit spikes with peak-to-peak voltage ranging from 52 µV to 115 µV are provided alongside a histogram of peak-to-peak voltages of detected units. Finally, field potential data from a single channel is shown in Figure 4.8.

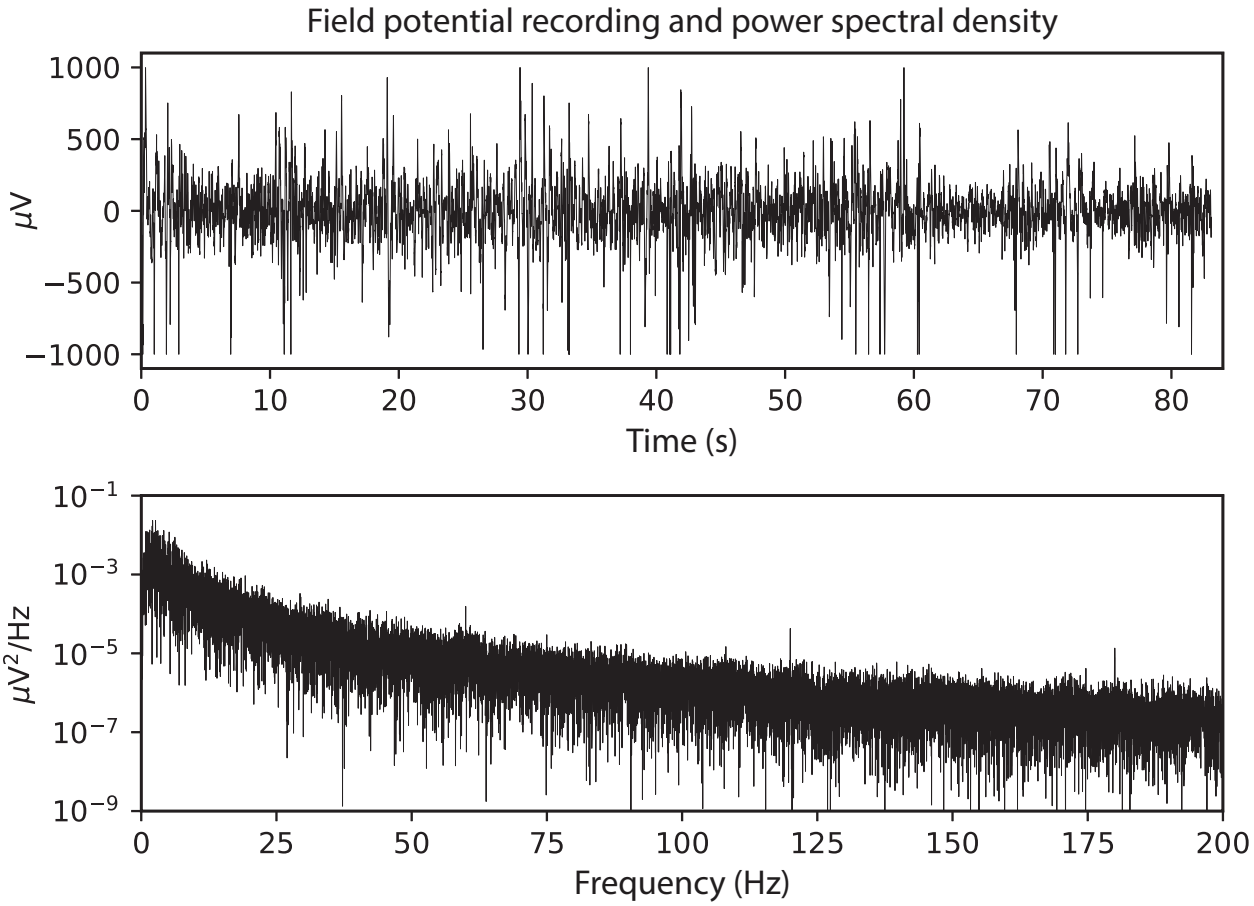

Figure 4.8: Analog field potential signal recorded on channel 32 at 1 kS/s and corresponding power spectral density. Large spikes in the time-domain signal are breathing artifacts.

SNR is calculated for each recorded unit and tabulated in Table 4.1. Two methods are used, as there is no standardized method for computing the SNR of spikes given that they are nonperiodic signals. Method A takes the ratio of the peak-to-peak waveform voltage on a given channel to the RMS noise voltage. Method A is common in the literature [142–144]. Method B takes the square of the ratio of the RMS value of the spike waveform to the RMS noise voltage. While Method B resembles the traditional method of calculating SNR for a periodic signal, for a nonperiodic signal such as a spike waveform it is dependent upon the time window over which the spike RMS value is

Table 4.1: RMS values of noise recordings, RMS and peak-to-peak voltages of recorded units, and SNR values calculated per Methods A and B of Section 4.4.

Channel/Unit	$V_{RMS,noise}$ (μV)	$V_{RMS,unit}$ (μV)	$V_{p-p,unit}$ (μV)	SNR_A	SNR_B
Ch 4 - Unit 1	17.63	57.86	34.83	0.26	1.66
Ch 5 - Unit 1	16.53	55.48	36.39	0.21	1.52
Ch 6 - Unit 1	22.17	70.96	24.16	0.84	2.94
Ch 9 - Unit 1	19.39	66.33	64.71	0.090	1.03
Ch 10 - Unit 1	18.84	64.57	76.39	0.061	0.85
Ch 11 - Unit 1	23.32	77.13	44.34	0.28	1.74
Ch 13 - Unit 1	26.13	86.24	46.76	0.31	1.84
Ch 17 - Unit 1	22.70	74.24	31.90	0.51	2.33
Ch 18 - Unit 1	22.27	70.19	36.41	0.37	1.93
Ch 19 - Unit 1	21.97	70.82	48.58	0.20	1.46
Ch 20 - Unit 1	19.36	62.98	37.07	0.27	1.70
Ch 21 - Unit 1	22.38	72.66	33.28	0.45	2.18
Ch 24 - Unit 1	22.29	71.78	34.86	0.41	2.06
Ch 25 - Unit 1	23.28	75.47	30.00	0.60	2.52
Ch 26 - Unit 1	38.31	118.95	36.88	1.08	3.23
Ch 26 - Unit 2	17.90	61.38	36.88	0.24	1.66
Ch 27 - Unit 1	20.21	68.85	69.67	0.084	0.99
Ch 28 - Unit 1	17.74	61.08	62.63	0.080	0.98
Ch 29 - Unit 1	22.94	76.75	46.49	0.24	1.65
Ch 30 - Unit 1	20.87	70.43	43.47	0.23	1.62
Ch 32 - Unit 1	37.46	116.24	24.13	2.41	4.82
Ch 32 - Unit 2	16.98	58.10	24.13	0.50	2.41

calculated. SNR values for Method A range from 0.85 to 4.8, and those for Method B range from 0.061 to 2.4.

4.5 Conclusion

This chapter has demonstrated that reliable assembly of carbon fiber neural recording arrays is feasible, with 80-90% of recording electrodes having impedances of approximately 1 MΩ at 1 kHz and negligible crosstalk between channels. The arrays are capable of recording multiple single-unit action potentials with spatial oversampling as predicted by the 38 μm electrode pitch.

The assembly process described is finely tuned, having considered percolation network theory to appropriately select an ICA meeting specific the requirements to function within the constrained volume of the through-silicon via. Further, a process was developed to graphitize residual polymer between silver particles in the ICA by applying a voltage exceeding the dielectric strength of the

polymer. Finally, the optimum combination of embedding compound, temperature, and blade type were selected to achieve the cleanest possible cut when exposing the recording sites on fibers arrayed two-dimensionally.

Taken together with the automated fiber threading system of Chapter 3, the assembly procedure presented in this chapter is scalable to a device with a large number of recording sites. This topic of scalability will be explored in depth in Chapter 5, considering what modifications to the described processes are required to scale this carbon fiber neural recording array to thousands of electrodes and demonstrating that the vision is well within reach.

Chapter 5

The roadmap toward scalability

The characterization and *in vivo* recordings presented in the previous chapter bring the discussion of the development of this high-density carbon fiber neural recording array full-circle in that they come to support the initial motivation for building such a device. From the first chapter, we saw that there is a clear need for a neural recording array that meets the varied requirements that may be present both in the scientific and clinical settings, including high channel count, minimal adverse biological response, single unit spatiotemporal resolution, full-volume sampling, and device longevity for chronic implantations. While longevity is outside the scope of this work, which was explicitly targeting acute implantation scenarios, the other four requirements *are* squarely within the scope of this dissertation. Among them, the minimal adverse biological response is addressed by use of carbon fiber microwire electrodes of sub-cellular dimension which have been shown previously not to elicit a perceptible foreign body response. The high spatiotemporal resolution is essentially a given for intracortical electrodes, and the full-volume sampling is enabled by the fine electrode pitch. While meeting these three requirements simultaneously already represents a step forward in the field, many of the efforts and design decisions in this work hold scalability toward a large number of channels as the ultimate goal. While the array presented in this work has twice the channel count of the current state of the art among carbon fiber neural recording arrays, this difference is marginal given that the field is trending toward discussion of devices that count channels in the thousands. The remainder of this chapter looks at this topic of scalability more closely, considering specifically how this carbon fiber neural recording array design is potentially scalable to thousands of electrodes, what additional work or modifications would be involved in doing so, and any additional challenges this may present. Each step in the procedure is considered, including the scalability of the substrate, the scalability of the assembly process, and CMOS integration.

5.1 Scaling the substrate

Chapter 2 described in-depth the three-mask substrate microfabrication procedure, and why based upon a look at prior work this through-silicon approach is appropriate—namely, that to array fibers in two dimensions, they must extend orthogonally to a two-dimensional substrate. For a large

number of electrodes, stacking one-dimensional rows of fibers is impractical, and thus the out-of-plane configuration becomes necessary.

Microfabrication presents the next benefit to scalability, namely that every processing step affects the entire area of the wafer surface simultaneously. In other words, the time required and complexity of the process is inherently independent of the number of recording sites on a particular device. While the masks would have to be redesigned to reflect the increased electrode count, procedural layout generation renders this straightforward.

While increasing the number of through-silicon vias on the mask is trivial, the routing is somewhat more involved and necessitates consideration of how each trace will be routed from the via and out from the head of the device, as well as the degree to which traces widen and diverge at a given point on the substrate to minimize resistance and crosstalk, respectively. Further, as the number of vias increases, the distance between each pair of vias must increase to accommodate this routing. As will be discussed in section 5.3, however, this added complexity to the routing may be unnecessary, as the burden of signal routing can be relegated to an integrated ASIC.

With regards to the microfabrication process itself, while the process may be independent of the particular number or arrangement of vias and traces on the substrate, second-order concerns are worth brief consideration. For example, as the number of vias increases, there will be both local and wafer-scale mass loading of the SiO_2 and Si DRIE etches. If the quantity of etch gases present are heavily consumed in the reaction, then the etch rate will begin to decrease. For the scale and density of features, however, this is not expected to be a concern. Personal empirical observations have found that mass loading does not play a significant role at the wafer scale until the exposed area being etched is on the order of tens of percent of the wafer surface. Local mass loading has not been observed for the middle holes on a 6x6 array at the finest pitch that one might practically want to use (38 µm), so it is unlikely to significantly affect a larger array of vias. This same mass loading argument extends to all subsequent etch steps and the ALD deposition of TiN.

The yield-limiting step in the microfabrication process related to the photoresist coating process for patterning the metal film. Because the surface tension-driven problems observed occurred in an all-or-none fashion on each die, the substrate die yield can be expected to be similar if scaled to a large number of recording sites. Again, however, this may be moot speculation given that substrate-level routing may be replaced by an ASIC's internal routing.

While integration of a separate ASIC could reduce the necessary microfabrication process to a single mask, performing both via and ouline DRIE steps in a single step, another option for CMOS integration might involve post-processing a CMOS wafer with some subset of the microfabrication process described in Chapter 2. In this case, all high-temperature ($>$400 °C steps would need to be removed and/or replaced with low-temperature equivalents. Specifically, this would affect the thermal oxidation steps and the H_2 anneal. The oxidation steps could feasibly be replaced by PECVD deposition of a dielectric material (SiO_2, Si_3N_4, etc.), but there is no low-temperature substitute for the H_2 anneal process. Provided the ALD TiN process yields truly conformal coverage, however, the H_2 anneal may be unnecessary as conductivity along the sidewall of the via to the face of the substrate would not be dependent upon shadow-free deposition of the top-level metal film. This presumption is unverified as we opted to hedge my bets by both smoothing the sidewall for continuous sputter deposition as well as depositing TiN by ALD, so the

reader is cautioned to take it as such.

5.2 Scaling the assembly process

Once the substrate has been scaled to a large number of electrode-ready vias, the next step is to scale the assembly procedure. The majority of the assembly procedure is unchanged, as steps such as filling the vias with an isotropically conductive adhesive (ICA) using a doctor blade or cryototoming to expose the recording sites remain unchanged. The steps of note in the assembly process are those that are performed serially, that is where the time required scales linearly with the number of electrodes. Some of these serial steps, such as electroplating and characterization, are already automated by nature. While the process time may increase linearly with the number of electrodes, the human time required for an automated process amounts to setup overhead and is independent of the number of electrodes. Thus, as presented in the third chapter, automating a serial step is an acceptable route toward scaling that step to a large number of electrodes.

The first N-per-device serial step in the assembly process is wire bonding the substrate to the flex PCB. While wire bonding can be automated, and typically is for high-bond-count integrated circuits, this still requires considerable space on the substrate. If the pad pitch were 100 µm, a 100 mm perimeter would be required for one thousand electrodes, which is clearly impractical. Flip-chip bonding could be a feasible alternative, but typical 100 by 100 µm pad sizes and 200 µm pitch required would still result in a large die 9 mm on a side. There are boutique fine-pitch flip-chip processes available, but pushing a process to its limit rarely yields a robust, repeatable process, particularly when working with a non-standard chip (i.e. not a foundry-manufactured CMOS IC) and non-standard substrate (flex PCB instead of fiberglass). Instead, it would be preferable to replace the bonding procedure with a solution either involving fewer pads (on-substrate CMOS electronics) or replace the bonding process with something that doesn't require significant additional substrate area beyond the array of vias. Potential paths toward each are discussed in section 5.3.

The other N-per-device step in the process, as discussed at length in the third chapter, is threading the individual carbon fiber filaments through the substrate vias. As this process can take 2-5 minutes per fiber (12-30 fibers per hour) even for an experienced individual, scaling to 1000 fibers or more is again infeasible, particularly when considering the working time of the ICA into which the fibers are threaded. While the details of a practical, low-cost automated assembly system capable of submicron positioning have been previously described and the concept demonstrated, there are yet a few outstanding steps toward making that system feasible.

Practical requirements for automating fiber threading at high channel counts

The first two outstanding issues with the current system were introduced briefly at the end of Chapter 3. First, a proper method of repeatably cutting the capillary with the correct tip diameter is necessary. Since tools exist and this is standard practice in biology laboratories, it warrants no further discussion other than to say that such tools or expertise must be acquired to improve

the reliability of the robotic threading system. Second, a servo-actuated mechanism for cutting the fibers is required. Again, since this was introduced previously and the implementation is straightforward, no extended discussion warranted other than to mention that there are a variety of cutting mechanisms to be explored, such as tissue scissors or something in the style of a microscale cigar cutter.

Another challenge to address with regards to using the automated threading system to aid assembly of a high channel count device is the preparation and nominally spooling of the fiber. For 3 mm recording electrodes, 3 m of carbon fiber monofilament is necessary per thousand electrodes. Monofilaments can feasibly be separated from the tow (bundle) in 200-300 mm lengths, but replenishing the assembly robot's fiber source every hundred electrodes is inconvenient, at best. Instead, one would ideally want a long (tens of meters) spool of carbon fiber monofilament. While there is no fundamental reason why this can't exist, we have been unable to find a supplier of $<30\,\mu m$ diameter carbon fiber monofilament, and fiber of that diameter would obviate the benefits of using carbon fiber. Practically, manufacturing 5-7 µm monofilament may be difficult because any break along the length would require human intervention. Manufacturing a tow, in contrast, provides additional filaments to which the broken monofilament can electrostatically or hygroscopically attract, allowing the process to continue. Nevertheless, this problem of sourcing a long monofilament remains a practical difficulty in threading thousands of channels. Until an adequate solution is developed, manually loading new lengths of fiber approximately every one hundred electrodes threaded is an unfortunate limitation of the automated threading system.

Finally, removing a threaded array from the automated threading system to load it into an oven is potentially quite difficult. While the entire stage on which the micropositioners are mounted can be removed, this is both labor intensive and accident prone. Instead, the blue laser built into the system may provide a suitable method for heating the substrates to the desired temperature to cure the ICA. While the laser was used in previous iterations of the array design to anneal gold at temperatures exceeding 500 °C, it has not yet been evaluated or characterized for this purpose. Further, the mounting of the substrate to the micropositioner must be consistent to achieve repeatable results at a given laser current and have low thermal conductivity to minimize the laser power required.

While a laser might not seem the most straightforward method of heating the substrate, it holds several advantages over competing methods. The three methods of heat transfer are radiation, convection, and conduction, and each presents options for substrate heating. Convection is the quickest method to dismiss, both because the carbon fibers are sensitive to airflow and because it would require considerable input power to achieve sufficient heating to heat the small substrate within the large volume of air necessary for the assembly robot. Further, we to heat only the substrate, as other components of the assembly system are not suited to the 150-250 °C temperatures at which our ICAs cure. Conduction seems promising, as small ceramic heaters are easy to use and can easily achieve the desired temperatures, but firmly thermally contacting the small silicon substrate with a relatively large ceramic heater without disrupting or damaging the substrate again is practically challenging. Many components must fit within a small volume around the substrate within the assembly system (feeder assembly, camera, etc.), and having to include a ceramic heater would be nontrivial. Radiative heat transfer, in contrast, can be as localized as conductive heating

and yet require no contact. We briefly explored infrared spot heating, but found the spot size still significantly larger than the device, and the halogen bulb less than robust. The laser, in contrast, was easily focused to a spot size less than that of the substrate, and yet the total input power is 1-3 orders of magnitude lower than any of the other heating methods investigated because nearly all of that energy is deposited into the substrate. Any reflected energy is defocused and contributes neglible heating to the assembly system enclosure. Further, the collimated beam affords more flexibility in the placement of the laser compared to any other heating method.

5.3 Integrating electronics

Integrating electronics is the single largest yet outstanding modification necessary to scale this electrode array to thousands of electrodes. As alluded previously, moving the amplification, multiplexing, digitizing, and even potentially compression operations onto the device itself can significantly reduce the interconnect required, the quantity of data that must be transferred, the impact of electromagnetic interference, and the complexity of the microfabrication process. While CMOS integration is non-trivial, there are two feasible routes to be considered: directly incorporating CMOS onto the silicon substrate, or bonding the substrate to a separate CMOS die.

Option A: Incorporating CMOS into the silicon substrate

Direct incorporation of CMOS into a neural recording array has recently been demonstrated by Jun *et al.* [93]. While it is an excellent potential solution, it made use of facilities capable of processing both high-yield CMOS as well as MEMS, which are unaccessible to many. Further, MEMS post-processing of CMOS restricts allowable process steps to those below about 400 °C as noted in section 5.1. CMOS post-processing of MEMS is almost never feasible both because of microfabrication tool cleanliness requirements as well as the topography introduced by most MEMS processes. Post-processing CMOS is further practically limited by the need for an intact wafer, whereas foundry-produced CMOS must be returned diced unless the circuit designer has purchased the entire wafer area. For most research, this practical requirement is out of reach.

A more accessible approach would be to incorporate very basic amplifiers and multiplexers using an researcher-accessible cleanroom CMOS process. While one must forego the complexity, fine linewidth, and robustness of a professional foundry process that would enable digitization and compression, amplification and multiplexing are possible even with rudimentary CMOS available in most laboratory cleanrooms. Such an approach would come with the same temperature restrictions as noted above, but the researcher would have access to a whole CMOS wafer for MEMS post-processing and would have more flexibility over process steps in producing the active substrate. The clear drawback of this approach is the complexity of such a process. Even the most basic CMOS process is significantly more involved than most MEMS processes, and few laboratory cleanrooms have the strict process control necessary for high yield.

Option B: Bond the substrate to a CMOS die

Alternatively, rather than incorporating the CMOS directly into the substrate, one could bond the substrate directly to a CMOS die. Of the bonding methods discussed previously, flip-chip bonding holds some promise, but still requires relatively large pitch and non-negligible additional processing to prepare the substrate for bonding. Further, the key limitation of die-to-die bonding is that still N connections are required for N electrodes. To address these challenges, an alternate method of bonding is preferred.

The through-silicon vias with isotropically conductive adhesive present a promising solution, inherently providing the electrically conductive bonding agent in the ICA itself and requiring no routing on the substrate provided that the bond pads on the CMOS die are aligned with the vias on the array substrate. With the substrate and CMOS dice aligned and held firmly together, the ICA can be applied as usual, potentially with vacuum assistance to ensure complete filling of the substrate vias and intimate electrical contact with the pads on the underlying CMOS die. This approach takes advantage of the existing assembly process without significant modification, and even simplifies the microfabrication process as with substrate routing no longer necessary the via and device outline etches can be collapsed to a single mask and etch step.

No approach is without cost, however. With ICA bonding the array substrate to the CMOS die in the same step as the ICA is cured to connect the fibers to the substrate, we are limited to the inherent conductivity of the ICA inside the via. Applying an 18 V breakdown potential is no longer an option, as nearly all available CMOS processes are rated for no more than low single-digit voltages before the gate dielectric itself will break down. One must either tolerate the increased impedance or find an alternate isotropically conductive adhesive. Given that the silver ink/epoxy approach has already been optimized near its physical limit as discussed at length in Chapter 4, an this approach may require alternate type of conductive material altogether.

Replacing the isotropically conductive adhesive

Two potential approaches stand for potentially replacing the silver ink and epoxy: solder and electroplated metal. Electroplating is of interest because it may be possible to electroplate vertically upon the CMOS bond pad and up into the via, with the electroplated metal wrapping around the fiber and filling the hole. Such an approach has been successfully demonstrated inside a silicon trench by [108], but preventing short circuits and fiber aggregation is known to be a challenge.

A fine solder paste, in contrast, can conceptually be applied in the same manner as the silver ink and epoxy, and would offer a pure metal film guaranteed to provide low-resistance contact between the fiber a the copper-, nickel-, or tin-plated CMOS bond pad. Sufficiently fine solder compositions, while they do exist and seem very attractive, are considered a specialty product that for financial reasons limited to large-volume orders. While fine solders can be custom-made in the laboratory, this is often impractical, potentially hazardous, and oxide formation on the solder particles must be carefully mitigated as submicron solder particle sizes as the surface to volume ratio is substantially higher compared to standard Type 3 to Type 5 solder paste products that are tens of microns in diameter. So-called fluxless solder may be advantageous in this regard, but

most are gold-based and are thus can be costly. Further, “fluxles” solder composed of gold and tin still must be reflowed in a forming gas environment to prevent oxidation of the tin component and reduce surface any surface oxide formed on the mating surfaces.

No single approach is without difficulty or drawback, but neither is any approach discussed impossible, leaving the future researcher with a number of potentially viable options to be explored in integrating CMOS with the carbon fiber array and ultimately scaling the device to thousands of electrodes. Certainly the path toward scalability presented here is clearer and more attainable than with any previous carbon fiber or microwire-style neural recording array, and in that regard this work proves a success in providing that clear roadmap toward scalability.

5.4 Closing remarks

No research is ever entirely complete, as there are always parameters to further optimize and new and interesting directions to pursue, but it is my hope that you, the reader, have come away from this dissertation with both a clarity of the need for a high-density carbon fiber neural recording array with a large number of recording electrodes as well as a clear technical route to fabricate such a device based upon this small-scale proof of concept. We have demonstrated the array viable both by recording single unit action potentials from a rat’s motor cortex, as well as through extensive characterization. Further, we have done our best to be transparent about the limitations of the device and this method of fabrication, and have provided a thorough physical physical understanding of all such relevant challenges to inform the rational design decisions in development of this array. Finally, this chapter has provided a look toward the future for the potential of this technology, as in any pursuit is this vision for the future that drives us forward. While we can’t claim with certainty that this device will transform the world, we can confidently assert that we have done our part to (and continue to) move the ball forward.

Appendix A

Lateral microwire compliance

The stiffness of microwires against lateral displacement is a concern for micromotion-induced tissue damage. To this end, I compare here the lateral spring constant of 1 mm of carbon fiber to an equal length of tungsten microwire. This length l represents the unsupported segment of the microwire between the substrate and brain, and approximately accounts for the thickness of a rat's skull.

A.1 Lateral spring constant of a 5.4 micron carbon fiber

To find the lateral spring constant of a carbon fiber implanted in the brain, treat it as a fixed-guided beam of circular cross-section, with a point load applied at the guided end. The radius is 2.7 µm and Young's modulus E is taken to be 234 GPa.

From Roark's Formulas for Stress and Strain [145], Table 8.1.1b,

$$y = \frac{-W}{12EI}(l-a)^2(l+2a) = \frac{-Wl^3}{12EI} \; for \; a = 0$$

$$I = \frac{\pi}{4}r^4$$

Therefore, the spring constant is:

$$k_{CF} = \frac{3\pi E r^4}{l^3} \left[\frac{N}{m}\right]$$

For l = 1 mm,

$$k_{CF} \approx 0.12 \left[\frac{N}{m}\right]$$

A.2 Lateral spring constant of a 25 micron tungsten microwire

Repeating the analysis above for 1 mm long fixed-guided tungsten microwire of 12.5 µm radius and Young's modulus $E = 450\,\text{GPa}$,

$$k_W = \frac{3\pi E r^4}{l^3} \approx 104 \left[\frac{N}{m}\right]$$

The tungsten microwire is therefore about three orders of magnitude stiffer than the carbon fiber microelectrode against lateral displacement.

Appendix B

Tools developed to aid microfabrication and assembly

B.1 Alignment substrate microfabrication

The alignment substrates are microfabricated from a silicon-on-insulator (SOI) wafer with 15 µm device layer and 1 µm buried oxide. Low-stress silicon nitride (LSN) is deposited on both faces via low-pressure chemical vapor deposition (LPCVD), and subsequently patterned with standard photolithography and etched in a CF_4 plasma. The etch defines a 6x6 array of 33 µm holes on the same pitch as the device wafer, as well as a device outline for eventual release. Pyramidal funnels are etched into the silicon using 24% potassium hydroxide (KOH) at 80 °C, using the LSN as a hard mask and the buried oxide and (111) silicon plane as stop layers. Following the KOH etch, the front side of the wafer is protected with a second deposition of LSN. The backside LSN is removed with a CF_4 plasma as before, and the silicon handle is completely removed in KOH. Because SiO_2 is not a perfect barrier to KOH, the etch is monitored visually to identify complete removal of backside silicon. Finally, the alignment substrates are singulated and both LSN and SiO_2 removed using concentrated hydrofluoric acid (HF). This procedure is diagrammed in Supplementary Figure B.1.

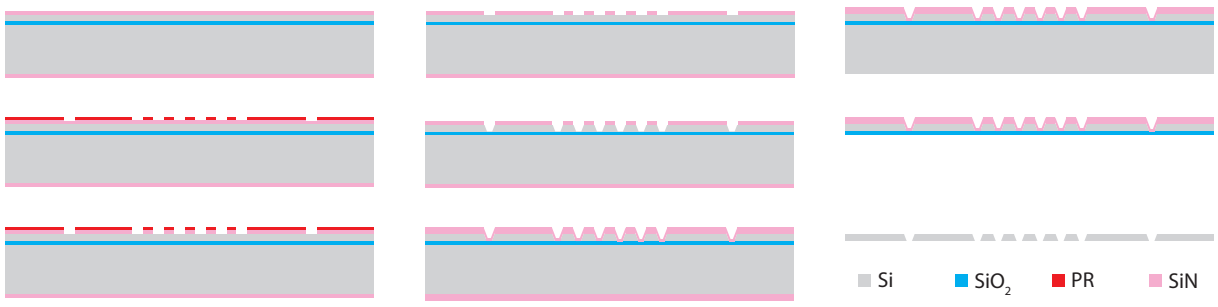

Figure B.1: Cross-sectional diagrams of the fabrication of the alignment aid funnels.

B.2 Temporary handle wafer bonding tool

Microfabrication processes often demand, for a variety of reasons, that a process wafer have a handle wafer temporarily (reversibly) bonding immediately behind it. Within the scope of this work, a few such reasons are:

1. We are performing a through-wafer etch and wish to protect the etcher's chuck from the process gases/plasma.

2. The process wafer has holes in it and either can't hold vacuum on a vacuum chuck or leaks helium on an electrostatic chuck with helium backside cooling.

3. The process wafer is thinner than the tool can accommodate, whether for optical reasons as with lithographic steppers or wafer edge finders, or for reasons of mechanical stability.

Several standard wafer bonding techniques exist and are available in the Marvell Nanolab, but none is without prohibitive drawbacks.

1. **Crystalbond 509**: Disallowed in many Nanolab tools, Crystalbond 509 (SPI Supplies, West Chester, PA) is prone to melting during long etches, allowing wafers to separate. Film thicknesses of crystal bond are often thicker than necessary because of the viscosity of the bonding agent and user inexperience, and challenging application leads to voids or trapped air bubbles that can cause wafer separation or damage during processing.

2. **Thermal grease**: Thermally conductive grease can provide a high thermal conductivity bond, which may enable wafers to be bonded at only 5 points rather than applying a continuous film across the wafer. Unfortunately, thermal grease has embedded metal particles (to increase thermal conductivity) that can become trapped in the substrate holes.

3. **Photoresist**: Photoresist can be used as a bonding agent, but thermal conductivity is very poor. This is typically addressed by using only very thin (1-2 µm) films, but such films provide poor adhesion to thin wafers because wafer bow increases dramatically as wafers become thinner. While robust bonding can be achieved with thicker (10 µm) films, poor thermal conductivity can result in photoresist burning during an etch process.

4. **Thermal release tape**: Thermal release tape can be used to bond two wafers and is relatively easy to apply, but is only suitable for short etch processes. Long or high-power etches can cause the tape to release mid-process. The thermal conductivity of thermal release tape is also quite poor due to its thickness.

5. **Dicing tape**: Dicing tape can be used in lieu of a handle wafer, but is only suitable for processes below 80 °C, at which point the tape and its adhesive can begin to melt. This can be helpful for holding vacuum, but is not allowed in most vacuum tools.

6. **Water**: A droplet of water can be applied between two wafers to temporarily bond them. Advantages include ease of bubble-free application and a thin resulting film thickness, but water is also prone to evaporation and is not suitable in most vacuum tools. This technique is best used in lithographic steppers where rapid evaporation is not a concern.

7. **Polyphenyl Ether**: Polyphenyl ether is a type of oil used in diffusion pumps, marketed as Santovac5 (SPI Supplies, West Chester, PA). It is excellent for forming a thin, thermally conductive bonding layer and is chemically inert to most processes. Bonding is typically performed on a hot plate, spreading a small volume of polyphenyl ether on the wafer and bringing two wafers into aligned contact at elevated temperature. While this is the preferred bonding method for etchers in the Nanolab, the bonding process can be messy, it can be difficult to achieve bubble-free thin films, and perfect alignment can be difficult. These inconveniences have led to a low rate of adoption among Nanolab members.

Because polyphenyl ether is the preferred bonding agent for etch processes from a technical standpoint, it seemed prudent to develop a tool to overcome the inconveniences and practical challenges. These drawbacks fundamentally come down to three points: (a) the mess associated with using polyphenyl ether as a bonding agent is in the spreading, (b) the risk of air bubbles is due to bonding the wafers at atmospheric pressure, and (c) alignment by hand is always difficult. The clear solution, then, involves bonding wafers under vacuum, letting surface tension spread a droplet of polyphenyl ether and an alignment fixture guide the wafers into the proper position. While these latter points are trivial, bringing wafers into contact while under vacuum required development of the tool shown in figure B.2.

The key operating principle of the bonding jig is that shape memory alloy (SMA) fingers hold one wafer suspended above the other, constrained within guide posts, and those fingers actuate to release the wafer at the desired temperature. Because this bonding process is typically performed at 100 °C and the vacuum oven has a tendency to overshoot its setpoint, I selected the SMA with the closest actuation temperature, 90-95 °C. When heated to this actuation temperature, the inwardly bent SMA fingers restore to their annealed shape (in this case, straight) and the wafer drops. Because only a small droplet of polyphenyl ether is placed in the center of the wafer, the bonding agent doesn't contact the top wafer and begin to spread until the third and final finger allows the top wafer to fully drop onto the wafer below. The base of the bonding jig is recessed, allowing the bottom wafer to sit on a narrow ledge of aluminum, so the bottom wafer's face doesn't contact the metal.

The detailed bonding procedure is as follows. First, place one wafer polished side down on the bonding jig. The positioning of the alignment posts will allow the wafer to fit in only one orientation. Ensure that the SMA fingers are not pinned beneath the wafer. Dispense 0.5 mL polyphenyl ether in the center of the wafer; do not spread. Bend each SMA finger inward from its base to point toward the center of the wafer, and place the second wafer atop the fingers. Place the jig into the vacuum oven and pump down to 10-30 torr at room temperature before switching on the heater to heat the oven to 80 °C (setting 5 on vacoven2). Let the oven stabilize at that temperature and reach base pressure (typically 1.2 torr) before increasing the setpoint to 120 °C

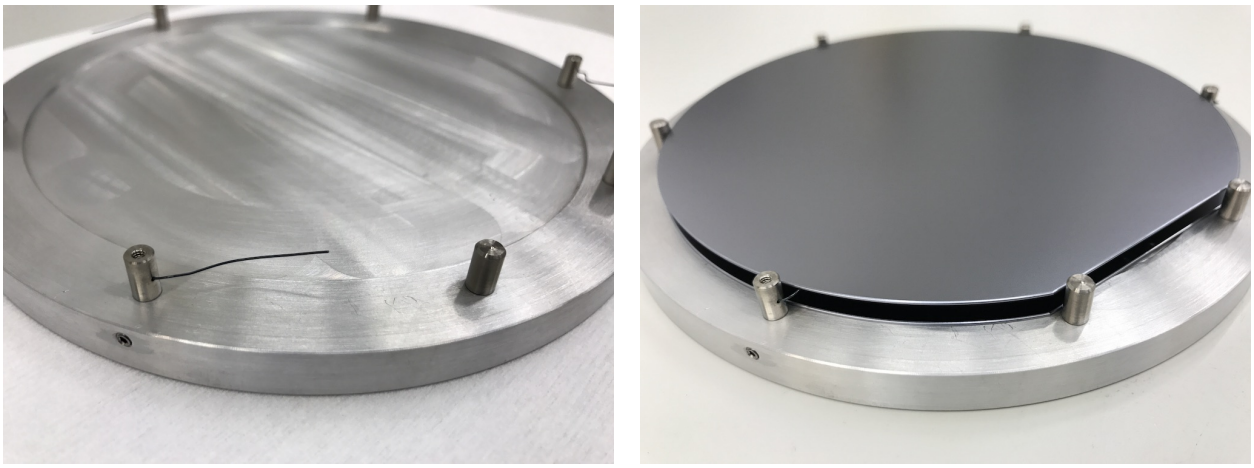

(a) (b)

Figure B.2: Photographs of the wafer bonding jig without (a) and with (b) wafers. The device wafer rests face-down over a recess milled into the aluminum base, and the handle wafer rests on three shape memory alloy wires bent inward from the three posts around the perimeter of the wafers. When the jig is heated in a vacuum oven, the shape memory alloy wires straighten to their default state and drop the handle wafer onto the device wafer, and capillary forces spread a small droplet of polyphenyl ether bonding agent into a thin film between the two wafers free of air bubbles.

(setting 7 on vacoven2). The fingers actuate, the wafer drops, and the polyphenyl ether begins to spread; allow 60 minutes for this complete process to ensure complete and even polyphenyl ether coverage across the wafer. Vent the oven and cool the jig with wafers on a large aluminum cooling chuck before attempting to remove the wafers.

Once processing is finished, the wafers can be separated using acetone to dissolve the polyphenyl ether. Because the film is thin, this process can take a prohibitively long time and potentially even leave the wafers stuck together, so it can help to insert razor blades around the edges of the wafers to provide a small spring force to help separate the wafers.

The wafer bonding jig itself remains in the Nanolab near the vacoven2 tool, owned by the Nanolab (who paid for its machining) and functionally under the care of the Pister Group. Design files and manual are on the Pister Group's Box repository, and the detailed operation and maintenance manual is on the Maharbiz Group wiki.

B.3 Wire bonder vacuum work holder with modular plates

Wire bonding is a part of nearly any MEMS project, but with the diversity of the MEMS field comes a wide variety of die and PCB shapes that must be accommodated during bonding. While mechanical clamping options exist, namely tape and copper stage clips, such mechanisms can be damaging to the substrate and may dissipate much of the bonding energy. Vacuum work holders

can provide a robust, secure substrate for holding the work piece (i.e. PCB and/or die), but the size and distribution of vacuum holes on standard vacuum work holders is often optimized for relatively large printed circuit boards rather than for microdevices on the order of millimeters. Additionally, as MEMS chips or PCBs may not be simply rectangular or may have cutouts/voids, a standard rectangular grid of vacuum holes may not be appropriate. I found when wire bonding my silicon substrate to the flex PCB that off-the-shelf work holders were inadequate, and many of my colleagues were having similar experiences, so it became prudent to develop a vacuum work holder that would meet our varying needs.

Because everyone's application is different, a key requirement for the vacuum work holder was modularity. This led to a design in which a relatively small and inexpensive top plate can be customized per individual application with appropriately sized/spaced vacuum holes and even topography, while a consistent base remains connected to the vacuum line. These top plates are machined from aluminum (Proto Labs, Maple Plain, MN) and may or may not have a raised section as needed to accommodate package geometry. Blank plates can be drilled locally with holes in positions to suit a user's device shape. Vacuum holes should be spaced such that at least three are positioned beneath the extents of the device such that the device can't easily translate or rotate during bonding. This ensures that the majority of the ultrasonic energy from the wedge bonder is imparted to the bond itself rather than to moving the device.

The base was designed as a cylinder for ease of rotation, and sized such that it naturally fits in the hand (2.5" diameter). A large hole is drilled through the center of the cylinder, and a small hole extends radially from the center to a barbed NPTF fitting that connects to a vacuum line. Both the top and bottom surfaces of the cylinder are milled inward slightly, excluding an outer lip, such that the vacuum area is nearly as large as the cylinder itself. Both top and bottom have a groove milled around the perimeter, just inside the aforementioned lip, sized for a gasket (1/8" SV2-Gasket, Pearson Workholding, Simi Valley, CA) to improve holding force both to the top plate as well as to the stage. CAD models and photographs of the base and top plate are shown in figure B.3. All CAD files are stored on the Pister Group Box repository, including top plate templates.

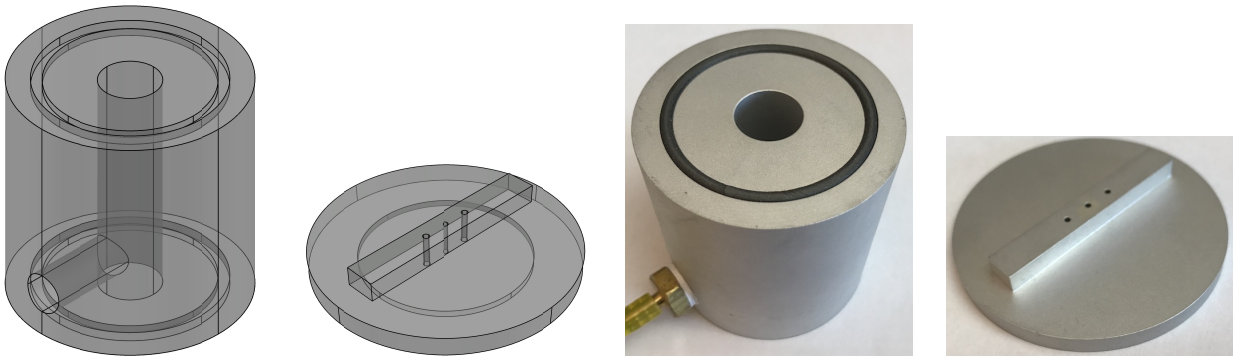

(a) (b) (c) (d)

Figure B.3: (a,c) CAD and photo of the vacuum work holder base. A black rubber gasket is pressed into the machined grooves on the top and bottom of the base unit. (b,d) CAD and photo of a representive top plate machined for DIP packages. This top plate was also used to for wire bonding the silicon array substrate to the flex PCB because of the suitable spacing of vacuum holes.

Bibliography

[1] Santiago Ramón y Cajal. *Les nouvelles idées sur la structure du système nerveux chez l'homme et chez les vertébrés*. C. Reinwald, 1894.

[2] Amiram Grinvald et al. "Optical imaging of neuronal activity." In: *Physiological reviews* 68.4 (1988), pp. 1285–1366.

[3] Werner Göbel and Fritjof Helmchen. "In vivo calcium imaging of neural network function." In: *Physiology* 22.6 (2007), pp. 358–365.

[4] Raymond Damadian. "Tumor detection by nuclear magnetic resonance." In: (1971).

[5] Seiji Ogawa et al. "Brain magnetic resonance imaging with contrast dependent on blood oxygenation." In: *Proceedings of the National Academy of Sciences* 87.24 (1990), pp. 9868–9872.

[6] Ritchie Chen, Andres Canales, and Polina Anikeeva. "Neural recording and modulation technologies." In: *Nature Reviews Materials* 2 (2017), p. 16093.

[7] ER Kandell, JH Schwartz, and Thomas M Jessell. *Principles of neuroscience*. 2000.

[8] Mikhail A Lebedev and Miguel AL Nicolelis. "Brain–machine interfaces: past, present and future." In: *TRENDS in Neurosciences* 29.9 (2006), pp. 536–546.

[9] Meel Velliste et al. "Cortical control of a prosthetic arm for self-feeding." In: *Nature* 453.7198 (2008), pp. 1098–1101.

[10] Leigh R Hochberg et al. "Neuronal ensemble control of prosthetic devices by a human with tetraplegia." In: *Nature* 442.7099 (2006), pp. 164–171.

[11] Miguel AL Nicolelis. "Brain–machine interfaces to restore motor function and probe neural circuits." In: *Nature Reviews Neuroscience* 4.5 (2003), pp. 417–422.

[12] John P Donoghue et al. "Neural discharge and local field potential oscillations in primate motor cortex during voluntary movements." In: *Journal of neurophysiology* 79.1 (1998), pp. 159–173.

[13] Yoshinao Kajikawa and Charles E Schroeder. "How local is the local field potential?" In: *Neuron* 72.5 (2011), pp. 847–858.

[14] Thomas Nevian et al. "Properties of basal dendrites of layer 5 pyramidal neurons: a direct patch-clamp recording study." In: *Nature neuroscience* 10.2 (2007), pp. 206–214.

[15] David Ogden and Peter Stanfield. “Patch clamp techniques for single channel and whole-cell recording.” In: *Microelectrode techniques* (1994), pp. 53–78.

[16] Miguel AL Nicolelis. *Methods for neural ensemble recordings*. CRC press, 2007.

[17] Matthew J Nelson et al. “Review of signal distortion through metal microelectrode recording circuits and filters.” In: *Journal of neuroscience methods* 169.1 (2008), pp. 141–157.

[18] J Ross Macdonald et al. *Impedance spectroscopy*. Vol. 11. Wiley New York etc, 1987.

[19] Subramaniam Venkatraman et al. “In vitro and in vivo evaluation of PEDOT microelectrodes for neural stimulation and recording.” In: *IEEE Transactions on Neural Systems and Rehabilitation Engineering* 19.3 (2011), pp. 307–316.

[20] Ernst Niedermeyer and FH Lopes da Silva. *Electroencephalography: basic principles, clinical applications, and related fields*. Lippincott Williams & Wilkins, 2005.

[21] Matti Hämäläinen et al. “Magnetoencephalography—theory, instrumentation, and applications to noninvasive studies of the working human brain.” In: *Review of Modern Physics* 65.2 (1993), p. 413.

[22] Kai J Miller et al. “Real-time functional brain mapping using electrocorticography.” In: *Neuroimage* 37.2 (2007), pp. 504–507.

[23] P Ledochowitsch et al. “Strategies for optical control and simultaneous electrical readout of extended cortical circuits.” In: *Journal of neuroscience methods* 256 (2015), pp. 220–231.

[24] Changhyun Kim and Kensall D Wise. “A 64-site multishank CMOS low-profile neural stimulating probe.” In: *Solid-State Circuits, IEEE Journal of* 31.9 (1996), pp. 1230–1238.

[25] Miguel AL Nicolelis et al. “Chronic, multisite, multielectrode recordings in macaque monkeys.” In: *Proceedings of the National Academy of Sciences* 100.19 (2003), pp. 11041–11046.

[26] Patrick K Campbell et al. “A silicon-based, three-dimensional neural interface: manufacturing processes for an intracortical electrode array.” In: *Biomedical Engineering, IEEE Transactions on* 38.8 (1991), pp. 758–768.

[27] Charles M Gray et al. “Tetrodes markedly improve the reliability and yield of multiple single-unit isolation from multi-unit recordings in cat striate cortex.” In: *Journal of neuroscience methods* 63.1 (1995), pp. 43–54.

[28] Peter Ledochowitsch et al. “A transparent μECoG array for simultaneous recording and optogenetic stimulation.” In: *Engineering in Medicine and Biology Society, EMBC, 2011 Annual International Conference of the IEEE*. IEEE. 2011, pp. 2937–2940.

[29] Rikky Muller et al. “A minimally invasive 64-channel wireless μECoG implant.” In: *IEEE Journal of Solid-State Circuits* 50.1 (2015), pp. 344–359.

[30] P Ledochowitsch et al. “Fabrication and testing of a large area, high density, parylene MEMS μECoG array.” In: *Micro Electro Mechanical Systems (MEMS), 2011 IEEE 24th International Conference on*. IEEE. 2011, pp. 1031–1034.

[31] Azadeh Yazdan-Shahmorad et al. “A large-scale interface for optogenetic stimulation and recording in nonhuman primates.” In: *Neuron* 89.5 (2016), pp. 927–939.

[32] P Ledochowitsch et al. “Sub-mm functional decoupling of electrocortical signals through closed-loop BMI learning.” In: *Engineering in Medicine and Biology Society (EMBC), 2013 35th Annual International Conference of the IEEE*. IEEE. 2013, pp. 5622–5625.

[33] Azadeh Yazdan-Shahmorad et al. “Demonstration of a setup for chronic optogenetic stimulation and recording across cortical areas in non-human primates.” In: *Optical Techniques in Neurosurgery, Neurophotonics, and Optogenetics II*. Vol. 9305. International Society for Optics and Photonics. 2015, 93052K.

[34] Peter Ledochowitsch, Elisa Olivero, and Michel M Maharbiz. “An Optically Transparent, Gold-ITO-Hybrid Electrode Array for Integration of Electrocorticography with Optogenetic Techniques.” In: ().

[35] Brian Pepin. “Transparent Micro-electrocorticography (ECoG) Arrays for Optogenetic Mapping of Surface Potentials.” In: (2013).

[36] CA Diaz-Botia et al. “Fabrication of all-silicon carbide neural interfaces.” In: *Neural Engineering (NER), 2017 8th International IEEE/EMBS Conference on*. IEEE. 2017, pp. 170–173.

[37] Camilo Diaz-Botia et al. “A silicon carbide electrode technology for the central and the peripheral nervous system.” In: *Journal of Neural Engineering* (2017).

[38] Wilfrid Rall. “Electrophysiology of a dendritic neuron model.” In: *Biophysical journal* 2.2 (1962), pp. 145–167.

[39] Fred Rosenthal. “Extracellular potential fields of single PT-neurons.” In: *Brain research* 36.2 (1972), pp. 251–263.

[40] Bruce L McNaughton, John O’Keefe, and Carol A Barnes. “The stereotrode: a new technique for simultaneous isolation of several single units in the central nervous system from multiple unit records.” In: *Journal of neuroscience methods* 8.4 (1983), pp. 391–397.

[41] Kenneth D Harris et al. “Accuracy of tetrode spike separation as determined by simultaneous intracellular and extracellular measurements.” In: *Journal of neurophysiology* 84.1 (2000), pp. 401–414.

[42] Jerald D Kralik et al. “Techniques for chronic, multisite neuronal ensemble recordings in behaving animals.” In: *Methods* 25.2 (2001), pp. 121–150.

[43] Miguel AL Nicolelis et al. “Reconstructing the engram: simultaneous, multisite, many single neuron recordings.” In: *Neuron* 18.4 (1997), pp. 529–537.

[44] Andrew Jackson and Eberhard E Fetz. “Compact movable microwire array for long-term chronic unit recording in cerebral cortex of primates.” In: *Journal of neurophysiology* 98.5 (2007), pp. 3109–3118.

[45] Gary Lehew and Miguel AL Nicolelis. “State-of-the-art microwire array design for chronic neural recordings in behaving animals.” In: *Methods for neural ensemble recordings* 2 (2008), pp. 361–371.

[46] Craig T Nordhausen, Edwin M Maynard, and Richard A Normann. “Single unit recording capabilities of a 100 microelectrode array.” In: *Brain research* 726.1 (1996), pp. 129–140.

[47] Susan Schmidt, Kenneth Horch, and Richard Normann. “Biocompatibility of silicon-based electrode arrays implanted in feline cortical tissue.” In: *Journal of Biomedical Materials Research Part A* 27.11 (1993), pp. 1393–1399.

[48] Khalil Najafi, KD Wise, and Tohru Mochizuki. “A high-yield IC-compatible multichannel recording array.” In: *IEEE Transactions on Electron Devices* 32.7 (1985), pp. 1206–1211.

[49] György Buzsáki. “Large-scale recording of neuronal ensembles.” In: *Nature neuroscience* 7.5 (2004), pp. 446–451.

[50] Carolina Mora Lopez et al. “An implantable 455-active-electrode 52-channel CMOS neural probe.” In: *Solid-State Circuits, IEEE Journal of* 49.1 (2014), pp. 248–261.

[51] Antal Berényi et al. “Large-scale, high-density (up to 512 channels) recording of local circuits in behaving animals.” In: *Journal of neurophysiology* 111.5 (2014), pp. 1132–1149.

[52] Maysamreza Chamanzar et al. “Ultracompact optoflex neural probes for high-resolution electrophysiology and optogenetic stimulation.” In: *Micro Electro Mechanical Systems (MEMS), 2015 28th IEEE International Conference on*. IEEE. 2015, pp. 682–685.

[53] Angela Tooker et al. “Polymer neural interface with dual-sided electrodes for neural stimulation and recording.” In: *Engineering in Medicine and Biology Society (EMBC), 2012 Annual International Conference of the IEEE*. IEEE. 2012, pp. 5999–6002.

[54] Gustavo Rios et al. “Nanofabricated neural probes for dense 3-D recordings of brain activity.” In: *Nano letters* 16.11 (2016), pp. 6857–6862.

[55] Takashi D Yoshida Kozai et al. “Ultrasmall implantable composite microelectrodes with bioactive surfaces for chronic neural interfaces.” In: *Nature materials* 11.12 (2012), pp. 1065–1073.

[56] William M Reichert. *Indwelling neural implants: strategies for contending with the in vivo environment*. CRC Press, 2007.

[57] Michael D Norenberg. “The reactive astrocyte.” In: *The role of glia in neurotoxicity* 2 (2005), pp. 73–93.

[58] Stephen JA Davies et al. “Robust regeneration of adult sensory axons in degenerating white matter of the adult rat spinal cord.” In: *Journal of Neuroscience* 19.14 (1999), pp. 5810–5822.

[59] Stephen JA Davies, Pauline M Field, and Geoffrey Raisman. “Regeneration of cut adult axons fails even in the presence of continuous aligned glial pathways.” In: *Experimental neurology* 142.2 (1996), pp. 203–216.

[60] Vadim S Polikov, Patrick A Tresco, and William M Reichert. “Response of brain tissue to chronically implanted neural electrodes.” In: *Journal of neuroscience methods* 148.1 (2005), pp. 1–18.

[61] Roy Biran, David C Martin, and Patrick A Tresco. “Neuronal cell loss accompanies the brain tissue response to chronically implanted silicon microelectrode arrays.” In: *Experimental neurology* 195.1 (2005), pp. 115–126.

[62] Young-Tae Kim et al. “Chronic response of adult rat brain tissue to implants anchored to the skull.” In: *Biomaterials* 25.12 (2004), pp. 2229–2237.

[63] DH Szarowski et al. “Brain responses to micro-machined silicon devices.” In: *Brain research* 983.1 (2003), pp. 23–35.

[64] JN Turner et al. “Cerebral astrocyte response to micromachined silicon implants.” In: *Experimental neurology* 156.1 (1999), pp. 33–49.

[65] ROBERT SB CLARK et al. “Neutrophil accumulation after traumatic brain injury in rats: comparison of weight drop and controlled cortical impact models.” In: *Journal of neurotrauma* 11.5 (1994), pp. 499–506.

[66] Zaverio M Ruggeri. “Platelets in atherothrombosis.” In: *Nature medicine* 8.11 (2002), pp. 1227–1234.

[67] Kristina F Standeven, Robert AS Ariëns, and Peter J Grant. “The molecular physiology and pathology of fibrin structure/function.” In: *Blood reviews* 19.5 (2005), pp. 275–288.

[68] John W Griffin et al. “Axonal degeneration and disorders of the axonal cytoskeleton.” In: *The Axon: Structure, Function, and Pathophysiology* (1995), p. 375.

[69] T Fujita et al. “Cellular dynamics of macrophages and microglial cells in reaction to stab wounds in rat cerebral cortex.” In: *Acta neurochirurgica* 140.3 (1998), pp. 275–279.

[70] Michael T Fitch et al. “Cellular and molecular mechanisms of glial scarring and progressive cavitation: in vivo and in vitroanalysis of inflammation-induced secondary injury after CNS trauma.” In: *Journal of Neuroscience* 19.19 (1999), pp. 8182–8198.

[71] Jerry Silver and Jared H Miller. “Regeneration beyond the glial scar.” In: *Nature Reviews Neuroscience* 5.2 (2004), pp. 146–156.

[72] RK Clark et al. “Development of tissue damage, inflammation and resolution following stroke: an immunohistochemical and quantitative planimetric study.” In: *Brain research bulletin* 31.5 (1993), pp. 565–572.

[73] MA Bisby. *Regeneration of peripheral nervous system axons*. 1995.

[74] Robert L Schultz and T Joe Willey. “The ultrastructure of the sheath around chronically implanted electrodes in brain.” In: *Journal of neurocytology* 5.6 (1976), pp. 621–642.

[75] Tamara Roitbak and Eva Syková. “Diffusion barriers evoked in the rat cortex by reactive astrogliosis.” In: *Glia* 28.1 (1999), pp. 40–48.

[76] Xindong Liu et al. “Stability of the interface between neural tissue and chronically implanted intracortical microelectrodes.” In: *IEEE transactions on rehabilitation engineering* 7.3 (1999), pp. 315–326.

[77] Stéphanie F Bernatchez, Patrick J Parks, and Donald F Gibbons. “Interaction of macrophages with fibrous materials in vitro.” In: *Biomaterials* 17.21 (1996), pp. 2077–2086.

[78] JE Sanders, CE Stiles, and CL Hayes. “Tissue response to single-polymer fibers of varying diameters: evaluation of fibrous encapsulation and macrophage density.” In: *Journal of biomedical materials research* 52.1 (2000), pp. 231–237.

[79] John P Seymour and Daryl R Kipke. “Neural probe design for reduced tissue encapsulation in CNS.” In: *Biomaterials* 28.25 (2007), pp. 3594–3607.

[80] Paras R Patel et al. “Chronic in vivo stability assessment of carbon fiber microelectrode arrays.” In: *Journal of neural engineering* 13.6 (2016), p. 066002.

[81] Hyunjung Lee et al. “Biomechanical analysis of silicon microelectrode-induced strain in the brain.” In: *Journal of neural engineering* 2.4 (2005), p. 81.

[82] Michelle C LaPlaca et al. “High rate shear strain of three-dimensional neural cell cultures: a new in vitro traumatic brain injury model.” In: *Journal of biomechanics* 38.5 (2005), pp. 1093–1105.

[83] Aaron Gilletti and Jit Muthuswamy. “Brain micromotion around implants in the rodent somatosensory cortex.” In: *Journal of neural engineering* 3.3 (2006), p. 189.

[84] Erin Patrick et al. “Corrosion of tungsten microelectrodes used in neural recording applications.” In: *Journal of neuroscience methods* 198.2 (2011), pp. 158–171.

[85] Erdrin Azemi, Carl F Lagenaur, and Xinyan T Cui. “The surface immobilization of the neural adhesion molecule L1 on neural probes and its effect on neuronal density and gliosis at the probe/tissue interface.” In: *Biomaterials* 32.3 (2011), pp. 681–692.

[86] Cristina Marin and Eduardo Fernández. “Biocompatibility of intracortical microelectrodes: current status and future prospects.” In: *Frontiers in neuroengineering* 3 (2010).

[87] Ian C Clarke, Pat Campbell, and Nir Kossovsky. “Debris-mediated osteolysis–a cascade phenomenon involving motion, wear, particulates, macrophage induction, and bone lysis.” In: *Particulate debris from medical implants: mechanisms of formation and biological consequences*. ASTM International, 1992.

[88] Jeremy J Clark et al. “Chronic microsensors for longitudinal, subsecond dopamine detection in behaving animals.” In: *Nature methods* 7.2 (2010), pp. 126–129.

[89] Kee Scholten and Ellis Meng. “Materials for microfabricated implantable devices: a review.” In: *Lab on a Chip* 15.22 (2015), pp. 4256–4272.

[90] Jitendran Muthuswamy et al. “Microactuated neural probes to compensate for brain micromotion.” In: *Engineering in Medicine and Biology Society, 2003. Proceedings of the 25th Annual International Conference of the IEEE*. Vol. 2. IEEE. 2003, pp. 1941–1943.

[91] Laura Poole-Warren et al. “Development of bioactive conducting polymers for neural interfaces.” In: *Expert review of medical devices* 7.1 (2010), pp. 35–49.

[92] Jorg Scholvin et al. “Close-packed silicon microelectrodes for scalable spatially oversampled neural recording.” In: *Biomedical Engineering, IEEE Transactions on* (2015), pp. 120–130.

[93] James J Jun et al. “Fully integrated silicon probes for high-density recording of neural activity.” In: *Nature* 551.7679 (2017), p. 232.

[94] Lohitash Karumbaiah et al. “Relationship between intracortical electrode design and chronic recording function.” In: *Biomaterials* 34.33 (2013), pp. 8061–8074.

[95] Ayub K Ommaya. “Mechanical properties of tissues of the nervous system.” In: *Journal of Biomechanics* 1.2 (1968), 127IN23137–136138.

[96] JD Andrade and V Hlady. “Protein adsorption and materials biocompatibility: a tutorial review and suggested hypotheses.” In: *Biopolymers/Non-Exclusion HPLC*. Springer, 1986, pp. 1–63.

[97] Yoshinori Onuki et al. *A review of the biocompatibility of implantable devices: current challenges to overcome foreign body response*. 2008.

[98] David F Williams. “On the mechanisms of biocompatibility.” In: *Biomaterials* 29.20 (2008), pp. 2941–2953.

[99] Pouria Fattahi et al. “A review of organic and inorganic biomaterials for neural interfaces.” In: *Advanced materials* 26.12 (2014), pp. 1846–1885.

[100] Felix Franke et al. “High-density microelectrode array recordings and real-time spike sorting for closed-loop experiments: an emerging technology to study neural plasticity.” In: *Closing the Loop Around Neural Systems* (2014), p. 31.

[101] James C Barrese et al. “Failure mode analysis of silicon-based intracortical microelectrode arrays in non-human primates.” In: *Journal of neural engineering* 10.6 (2013), p. 066014.

[102] Abhishek Prasad et al. “Abiotic-biotic characterization of Pt/Ir microelectrode arrays in chronic implants.” In: *Frontiers in neuroengineering* 7 (2014).

[103] Abhishek Prasad et al. “Comprehensive characterization and failure modes of tungsten microwire arrays in chronic neural implants.” In: *Journal of neural engineering* 9.5 (2012), p. 056015.

[104] Takashi DY Kozai et al. “Mechanical failure modes of chronically implanted planar silicon-based neural probes for laminar recording.” In: *Biomaterials* 37 (2015), pp. 25–39.

[105] Michael Armstrong-James and Julian Millar. “Carbon fibre microelectrodes.” In: *Journal of neuroscience methods* 1.3 (1979), pp. 279–287.

[106] Arto Piironen, Matti Weckström, and Mikko Vähäsöyrinki. “Ultrasmall and customizable multichannel electrodes for extracellular recordings.” In: *Journal of neurophysiology* 105.3 (2011), pp. 1416–1421.

[107] Grigori Guitchounts et al. “A carbon-fiber electrode array for long-term neural recording.” In: *Journal of neural engineering* 10.4 (2013), p. 046016.

[108] Paras R Patel et al. “Insertion of linear 8.4 μm diameter 16 channel carbon fiber electrode arrays for single unit recordings.” In: *Journal of neural engineering* 12.4 (2015), p. 046009.

[109] Winthrop F Gillis et al. “Carbon fiber on polyimide ultra-microelectrodes.” In: *Journal of neural engineering* 15.1 (2018), p. 016010.

[110] Ming-Chang M Lee and Ming C Wu. “Thermal annealing in hydrogen for 3-D profile transformation on silicon-on-insulator and sidewall roughness reduction.” In: *Journal of Microelectromechanical systems* 15.2 (2006).

[111] Micheal Burke et al. “Low sheet resistance titanium nitride films by low-temperature plasma-enhanced atomic layer deposition using design of experiments methodology.” In: *Journal of Vacuum Science & Technology A: Vacuum, Surfaces, and Films* 32.3 (2014), p. 031506.

[112] KJ Owen et al. “High aspect ratio deep silicon etching.” In: *Micro Electro Mechanical Systems (MEMS), 2012 IEEE 25th International Conference on*. IEEE. 2012, pp. 251–254.

[113] BJ Lin. “Multi-layer resist systems.” In: ACS Publications, 1983.

[114] Jun-Bo Yoon et al. “Planarization and trench filling on severe surface topography with thick photoresist for MEMS.” In: *Micromachining and Microfabrication Process Technology IV*. Vol. 3511. International Society for Optics and Photonics. 1998, pp. 297–307.

[115] Vincenzo Guidi et al. “Thin-film gas sensor implemented on a low-power-consumption micromachined silicon structure.” In: *Sensors and Actuators B: Chemical* 49.1-2 (1998), pp. 88–92.

[116] Richard P Walters and Bernard S Covino. “Evaluation of high-Temperature diffusion barriers for the Pt-Mo system.” In: *Metallurgical Transactions A* 19.9 (1988), pp. 2163–2170.

[117] M-A Nicolet. “Diffusion barriers in thin films.” In: *Thin Solid Films* 52.3 (1978), pp. 415–443.

[118] V Švorčík et al. “Annealing of sputtered gold nano-structures.” In: *Applied Physics A* 102.3 (2011), pp. 747–751.

[119] Christopher AR Chapman et al. “Engineering on-chip nanoporous gold material libraries via precision photothermal treatment.” In: *Nanoscale* 8.2 (2016), pp. 785–795.

[120] Vincent Grolier and Rainer Schmid-Fetzer. “Diffusion-Reaction in the Au-Rich Ternary Au-Pt-Sn System as a Basis for Ternary Diffusion Soldering.” In: *Journal of Electronic Materials* 37.6 (2008), pp. 815–828.

[121] David M Jacobson and Giles Humpston. “Gold coatings for fluxless soldering.” In: *Gold Bulletin* 22.1 (1989), pp. 9–18.

[122] DM Jacobson and G Humpston. “Fluxless soldering.” In: *International materials reviews* 51.5 (2006), pp. 313–328.

[123] Chin C Lee, Chen Y Wang, and Goran S Matijasevic. "A new bonding technology using gold and tin multilayer composite structures." In: *Components, Hybrids, and Manufacturing Technology, IEEE Transactions on* 14.2 (1991), pp. 407–412.

[124] Chin C Lee and Ricky W Chuang. "Fluxless non-eutectic joints fabricated using gold-tin multilayer composite." In: *IEEE Transactions on Components and Packaging Technologies* 26.2 (2003), pp. 416–422.

[125] Hermann Oppermann and Matthias Hutter. "Au/Sn Solder." In: *Handbook of Wafer Bonding* (2012), pp. 119–138.

[126] RickyW Chuang et al. "A fluxless process of producing tin-rich gold-tin joints in air." In: *Components and Packaging Technologies, IEEE Transactions on* 27.1 (2004), pp. 177–181.

[127] Jozsef Csicsvari et al. "Massively parallel recording of unit and local field potentials with silicon-based electrodes." In: *Journal of neurophysiology* 90.2 (2003), pp. 1314–1323.

[128] Angad Singh et al. "Batch transfer of microstructures using flip-chip solder bonding." In: *Microelectromechanical Systems, Journal of* 8.1 (1999), pp. 27–33.

[129] MM Maharbiz, RT Howe, and KSJ Pister. "Batch transfer assembly of micro-components onto surface and SOI MEMS." In: *Transducers*. Vol. 99. 1999, pp. 7–10.

[130] Michael B Cohn et al. "Microassembly technologies for MEMS." In: *Micromachining and Microfabrication*. International Society for Optics and Photonics. 1998, pp. 2–16.

[131] Kristofer SJ Pister. "Hinged polysilicon structures with integrated CMOS TFTs." In: *Solid-State Sensor and Actuator Workshop, 1992. 5th Technical Digest., IEEE*. IEEE. 1992, pp. 136–139.

[132] Samuel M Felton et al. "Robot self-assembly by folding: A printed inchworm robot." In: *Robotics and Automation (ICRA), 2013 IEEE International Conference on*. IEEE. 2013, pp. 277–282.

[133] Bradley J Nelson, Yu Zhou, and Barmeshwar Vikramaditya. "Sensor-based microassembly of hybrid MEMS devices." In: *Control Systems, IEEE* 18.6 (1998), pp. 35–45.

[134] Nikolai Dechev, William L Cleghorn, and James K Mills. "Microassembly of 3-D microstructures using a compliant, passive microgripper." In: *Microelectromechanical Systems, Journal of* 13.2 (2004), pp. 176–189.

[135] A Bueno Mario, Josue Alvarez-Borrego, and L Acho. "Autofocus algorithm using one-dimensional Fourier transform and Pearson correlation." In: *5th Iberoamerican Meeting on Optics and 8th Latin American Meeting on Optics, Lasers, and Their Applications*. International Society for Optics and Photonics. 2004, pp. 760–765.

[136] Sarah L Swisher et al. "Impedance sensing device enables early detection of pressure ulcers in vivo." In: *Nature communications* 6 (2015), ncomms7575.

[137] S Yang et al. “A high performance 180 nm generation logic technology.” In: *Electron Devices Meeting, 1998. IEDM’98. Technical Digest., International*. IEEE. 1998, pp. 197–200.

[138] R Deepthi et al. “Rheometric studies on agarose gel-A brain mimic material.” In: *SASTECH Journal* 9.2 (2010), p. 27.

[139] Farhana Pervin and Weinong W Chen. “Mechanically similar gel simulants for brain tissues.” In: *Dynamic Behavior of Materials, Volume 1*. Springer, 2011, pp. 9–13.

[140] Zhi-Jian Chen et al. “A realistic brain tissue phantom for intraparenchymal infusion studies.” In: *Journal of neurosurgery* 101.2 (2004), pp. 314–322.

[141] Li Li and JE Morris. “Electrical conduction models for isotropically conductive adhesives.” In: *Journal of Electronics Manufacturing* 5.04 (1995), pp. 289–296.

[142] Chang Hao Chen et al. “An integrated circuit for simultaneous extracellular electrophysiology recording and optogenetic neural manipulation.” In: *IEEE Transactions on Biomedical Engineering* 64.3 (2017), pp. 557–568.

[143] Amir M Sodagar et al. “An implantable 64-channel wireless microsystem for single-unit neural recording.” In: *IEEE Journal of Solid-State Circuits* 44.9 (2009), pp. 2591–2604.

[144] You-Yin Chen et al. “Design and fabrication of a polyimide-based microelectrode array: application in neural recording and repeatable electrolytic lesion in rat brain.” In: *Journal of neuroscience methods* 182.1 (2009), pp. 6–16.

[145] Warren Clarence Young and Richard Gordon Budynas. *Roark’s formulas for stress and strain*. Vol. 7. McGraw-Hill New York, 2002.